The Strong Field Simulator: Studying Quantum Trajectories in Classical Fields

DISSERTATION

Presented in Partial Fulfillment of the Requirements for the Degree Doctor of Philosophy in the Graduate School of The Ohio State University

By

Andrew J. Piper, M.Sc.

Graduate Program in Physics

The Ohio State University

2022

Dissertation Committee:

Louis F. DiMauro, Advisor

Daniel Gauthier

Ilya Gruzberg

Douglass Schumacher

Abstract

When the electric field of a laser pulse approaches the field strength between a nucleus and valence electron, it is capable of ionizing atoms or molecules via quantum tunneling. Additionally, the laser field can turn and accelerate the electron to collide with the same atom or molecule it had escaped. The electron's trajectory after ionization can be understood classically, meaning the probability and energy of the recollision is determined by the moment the electron first escapes the atom or molecule. This three-step process of tunneling ionization, acceleration, and recollision has been studied for several decades by measuring the kinetic energies of elastically scattered electrons, the rate of double ionization from inelastic collisions, and the amount of Extreme Ultraviolet (XUV) light produced by recombination of the electron and ion. This has birthed an entirely new field of attosecond (10-18) physics, as the XUV light produced by recollision are laser like pulses of attoseconds duration.

In this work, I report on a novel study of electron recollision where attosecond pulses of XUV light are used to ionize gas targets in the presence of a strong Near Infrared (NIR) field, this technique dubbed a Strong Field Simulator (SFS). One difficulty of studying recollision is that tunneling can happen at any time within the NIR field, with some moments being more probable than others, so only a superposition of results from many different ionization times are observable. Correspondingly, the dynamics of individual trajectories are hidden away from typical strong field experiments. In SFS experiments, the single photon ionization from the attosecond XUV pulses serve to replace the tunneling step, while the NIR field still accelerates the electron and drives recollision. Separating the ionization step from the NIR field, I can precisely control the moment of ionization and isolate particular electron trajectories by varying the arrival time of the pulsed XUV and NIR fields. Therefore, the SFS can experimentally emulate the dynamics of a tunneled electron wavepacket in a

low frequency field and deconstruct it into constituent trajectories, constituting a quantum simulator.

This investigation can inform current efforts to use recollision, and its byproducts, as a means of imaging molecular dynamics with attosecond resolution, the inherent timescale of electron dynamics in atoms and molecules. In addition, these experiments can test models of electron correlation, the quantum mechanical theory of electron interactions, in the most basic atomic systems. Our understanding of which is essential to the advancement of chemistry and solid state physics.

Dedicated to the women whose love and support made this work possible. Tessa, Rebecca, and Barbara Piper.

Acknowledgments

Between the design, construction, and commissioning of the experimental apparatus, in addition to actually conducting the experiments in this dissertation, there are numerous people who have contributed to the completion of this work. I'd like to thank the following people for their help throughout my research career thus far:

1. Dr. Louis F. DiMauro, my advisor, for the opportunity to work in a world leading physics laboratory for strong field and attosecond physics. Lou has supported me through every step of this project and his confidence in my abilities has seen me through some difficult times.

2. Dr. Pierre Agostini for many discussions on strong field physics, attosecond metrology, and optics. Pierre has been a constant source of inspiration and incite.

3. Dr. Dietrich Kiesewetter, from whom I inherited this research project. Dietrich taught me so much and this work would have been impossible without the experience gained through his own dissertation work. I aspire every day to reach his caliber as an experimentalist.

4. Qiaoyi Liu, who has worked with me on this project for the past four years and will be continuing it going forward. Qiaoyi helped with the construction, testing, and data collection for these experiments. His positivity is infectious and I'm excited to see what he will accomplish in the years to come.

5. Dr. Greg Smith, Dr. Stephen Hageman, and Dr. Timothy Gorman all provided mentorship and guidance as senior graduate students when I first joined the DiMauro research group. They taught me everything I needed about vacuum and laser technologies.

6. Dr. Timothy Scarborough, Dr. Vyacheslav (Slava) Leshchenko, Dr. Cosmin Blaga, Dr. Antoine Camper, Dr. Abraham Camacho Garibay, Dr. Yaguo Tang, Dr. Gregory McCracken, and Dr. Sha (Lisa) Li who all worked as post-doctoral researchers during my time in the DiMauro group. They all took the time to answer my numerous questions and troubleshoot problems in the laboratory.

7. Dr. Kent Talbert, Bryan Smith, Dan Tuthill, Eric Moore, Zifan Wang, and Dina Eisssa. Fellow graduate students in the DiMauro group with whom I've shared fruitful conversations, the challenges of graduate school, and frustrations with maintaining a function experiment.

8. Niko Stamos and Bennett Atwater, undergraduate students I had the pleasure of mentoring and who contributed to the work in this dissertation.

9. Dr. Zhou Wang, Dr. Yu Hang (Marco) Lai, Dr. Hyunwook Park, Dr. Junliang Xu, Aziz Alqasem, and Dr. Drake Austin. Colleagues in the DiMauro group during my thesis work.

10. Dameyon Shipley, Kyle Schechter, and Jessi Middleton who have provided administrative support. They have been essential in navigating the shipwreck that is OSU's purchasing department.

11. Dr. Jens Bækhøj and Dr. Ken Schafer. Collaborator's at Lousiana State University who have provided theoretical support for the work in this dissertation.

12. Phil Davids, Mark Reed, and Kent Ludwig. The physics department at OSU is incredibly fortunate to have the building and research support from these gentlemen. They have provided essential advice and support on this project, and I'm not sure the PRB would still be standing without them.

13. Dr. Carol Tanner and David McKenna, my research advisor and coworker during my research work as an undergraduate at the University of Notre Dame.

14. Finally the countless friends I have made in the physics department as a graduate student. I'll always look back fondly on our lunchtime debates and discussions.

Vita

2015 ..... B.Sc. Physics. University of Notre Dame, Notre Dame, IN

2017 ..... M.Sc. Physics. The Ohio State University, Columbus, OH

2015 - present ..... Graduate Research Associate. The Ohio State University, Columbus, OH

Publications

P. Agostini, **A.J. Piper**, L.F. DiMauro. Attosecond Metrology. In C. Guo and S.C. Singh, editors, *Handbook of Laser Technology and Applications*, 2nd edition, volume 1, page 313. CRC Press, 2021.

A.J. Piper, Q. Liu, Y. Tang, A. Camacho Garibay, D. Kiesewetter, J. E. Bækhøj, K. J. Schafer, P. Agostini, L.F. DiMauro. Coherent control of XUV seeded non-sequential double ionization in a NIR field. *In Preparation*, 2022

S. Donsa, D.R. Tuthill, T.T. Gorman, T.D. Scarborough, **A.J. Piper**, E. Lindroth, J. Burgdörfer, G. Laurent, P. Agostini, L.F. DiMauro, L. Argenti. Asymmetry in pump-probe photoemission. *In Preparation*, 2022.

Fields of Study

Major Field: Physics

Studies in Ultrafast Physics: Agostini-DiMauro Ultrafast Atomic Physics Research Group

Table of Contents

List of Figures

Figure **Page**

List of Tables

List of Abbreviations

APT Attosecond Pulse Train. xiii, 8, 9, 11–13, 16–22, 60, 62, 71, 77, 79, 91, 92, 97, 102, 121

ATI Above Threshold Ionization. 3, 4, 6, 8, 13, 19, 95, 101, 103, 104, 116, 146

BBO Beta Barium Borate. 50, 62, 71, 73

CXRO The Center for X-Ray Optics. 74

eTOF Electron Time of Flight. 27, 54–56, 58, 88, 93, 109

FFT Fast Fourier Transform. 58, 59

FWHM Full-Width at Half Maximum. 51, 59, 65, 77, 87, 97, 139

GDD Group Delay Dispersion. 8, 25, 71–73

HHG High Harmonic Generation. xii, xiii, 5, 7–9, 18, 21, 23–28, 44–47, 50, 60–76, 78, 102, 105, 126, 128, 129, 136, 137, 141

IAP Isolated Attosecond Pulse. 18, 60–62

Ip Ionization Potential. 3, 8, 9, 11, 14, 15, 19, 21, 22, 27, 46, 52, 58, 61, 65, 66, 73, 77, 81, 83, 86, 107, 108, 115, 121, 126, 129, 141–143, 146, 149

IR Infrared. 26–28, 63, 69, 72, 75

LES Low Energy Structure. 7, 61, 100, 101, 104, 125, 149

MCP Microchannel Plate. xii, 53–57, 125, 135

NIR Near Infrared. ii, xiii, 1, 2, 6, 7, 11–21, 24, 25, 27, 30–32, 35, 37, 43–52, 55, 58, 60–65, 67, 71, 73, 77, 80–84, 86–89, 91–97, 99, 100, 102–111, 114–116, 118, 120–124, 126, 128–130, 137, 142, 143, 146, 147, 149

NSDI Non-Sequential Double Ionization. 5, 12, 22, 27, 58, 81, 129, 143

OPA Optical Parametric Amplifier. 31, 32

PLC Programmable Logic Controller. xiii, 34, 39–41, 131–133, 135

PROOF Phase. 89

RABBITT Reconstruction of Attosecond Beating by Interference of Two-Photon Transitions. 17, 18, 77, 89, 103

ROC Radius of Curvature. 46, 48, 49

SFA Strong Field Approximation. 15, 22, 58, 61, 81, 97, 107, 118–120, 142

SFS Strong Field Simulator. ii, xii–xiv, 11–14, 19, 21–31, 33, 37, 38, 42–45, 47, 48, 50, 52, 54–56, 60–65, 67–70, 73–77, 80–82, 84, 87, 91, 93–97, 104–107, 114, 116–118, 120, 122, 123, 125–127, 129, 130, 136, 142, 143, 148, 149

TDSE Time Dependent Schrödinger Equation. 12, 15, 20, 21, 92

TMP Turbomolecular Pump. 24, 33–43, 45, 131–135

TOF Time-of-Flight. 33, 52, 53, 55–57, 72, 80, 85, 93, 120, 125

TOFMS Time-of-Flight Mass Spectrometry. 27, 54–56, 59, 109, 125

UHV Ultrahigh Vacuum. 33, 38, 41

Up Ponderomotive Energy. 4–8, 10, 16, 18, 20, 63, 64, 86, 87, 93–95, 97, 100, 105, 106, 108, 109, 111, 114, 116, 118–121, 125, 126, 146, 149

XUV Extreme Ultraviolet. ii, xii–xiv, 5, 7, 11–22, 24–30, 37, 43–52, 57, 58, 60, 62–64, 66, 68–70, 74–77, 80–84, 86–88, 91–95, 97, 99, 101–111, 114–116, 118, 120–130, 136, 138–143, 146

Chapter 1
Introduction

"How can we prepare for the future if we won't acknowledge the past?"

— N.K. Jemisin, The Stone Sky

1.1 A Sense of Scale

The best place to begin any discussion of physical phenomena is to establish a sense of scale for the relevant parameters describing the system. In Strong Field and Attosecond Physics, the domains of this work, these parameters characterize the applied pulses of laser light and the electronic structure of an atom or molecule. Table 1.1 provides order of magnitude estimates comparing a Near Infrared (NIR) laser pulse and a noble gas atom (the rightmost column of the periodic table). What stands out is that there is the factor of 10 separating the relevant scales of this laser pulse and atom. Naively one would assume that the former would be incapable of probing the physics relevant to the latter. A single photon (optical period) is an order of magnitude too small (large) to access the energy (time) scales of a bound electron. The power of Strong Field Physics is how these expectations are undermined through highly nonlinear interactions, leading to complex phenomena at the interface between classical and quantum physics.

1.2 Strong Field Physics

In 1905, Albert Einstein published his seminal paper on the photoelectric effect [30]. Eighteen years prior, Heinrich Hertz had discovered that when a plate of metal was exposed to ultraviolet light sparks would erupt from the plate, in other words electrons were ionized

NIR Laser		Atom	
Parameter	Order of Magnitude	Parameter	Order of Magnitude
NIR Wavelength	~1 μm - 10^{-6} m	Atomic Radius	~1 Å - 10^{-10} m
NIR Period	~1 fs - 10^{-15} s	Orbital Period	~100 as - 10^{-16} s
Photon Energy	~1 eV	1st Excited State	~10 eV
Laser E-Field	~1 V/Å	Atomic E-Field	~10 V/Å

Table 1.1: Relevant scales in strong field physics

[48]. What was shocking at the time was that the energy of the electrons depended not on the strength or intensity of the light, but its frequency or color. Further complicating matters, the number of electrons depended on the intensity, yet below a certain frequency no electrons were ionized even under the most intense light sources available at the time. Einstein resolved this paradox by proposing that light was made up of individual packets, what we now call photons, that carry a discrete amount of energy proportional to the frequency. The metal plate required a certain amount of energy to be released, the work function, and only when the photon energy exceeded the work function would ionization occur. More intense light was made up of more photons, each of which could individually ionize an electron. The kinetic energy, KE, of the emitted electrons could be calculated by taking the difference of the photon energy, $\hbar\omega$, and the work function Φ, Equation 1.1. Where $\hbar$ is the reduced Plank constant and ω is the angular frequency of the light.

$$KE = \hbar\omega - \Phi \tag{1.1}$$

With the advent of the laser in 1960 [77], light of significantly higher intensities could be produced and soon after interactions involving multiple photons were observed [37, 53].

This led to the development of nonlinear optics, where light of one color or frequency could be directly converted to other frequencies through interactions of several photons with a medium. Returning to the photoelectric effect, it was now possible that at sufficient intensity lower frequency light could ionize a target with the combined energy of several photons [22]. It was assumed that the electron energies could not exceed some multiple n of the photon energy minus the work function, where n was the minimum number of photons required to exceed the work function, Equation 1.2.

$$KE = n\hbar\omega - \Phi \tag{1.2}$$

1.2.1 Above Threshold Ionization

In 1979, it was observed that at a laser focus of sufficient intensity xenon atoms would emit electrons of several different kinetic energies separated by the photon energy [2]. This observation of Above Threshold Ionization (ATI) marked the advent of Strong Field Physics, and presented a break down of Einstein's theory of the photoelectric effect. Further improvements of laser and detector technologies allowed for observations of ever increasing electron energies with increasing intensities [65], following the rule that the energies were equal to an integer multiple of the photon energy minus the Ionization Potential (Ip), the work function of an atom, see Equation 1.3.

$$KE = (n + s)\hbar\omega - Ip \tag{1.3}$$

Where s is the additional number of photons beyond the minimum number for ionization, n.

Extensions of these experiments to longer wavelengths and more intense fields began to defy perturbative models as ionization processes requiring dozens of photons were observed [16]. At this point it was found that the ionization mechanism could be better described by a tunneling mechanism, whereby the electron tunnels quantum mechanically out of the atomic Coulomb potential modified by the laser's electric field, as first postulated by Keldysh in 1964 [58], and later by Faisal [31] and Reiss [90]. In this limit, the physics could be described

semi-classically with a quantum mechanical atom and a classical electric field. Furthermore, these theories predicted that after ionization the dynamics of the freed electrons would be dominated by the classical external field. This "Keldysh" approximation would be validated by further experiments ionizing Rydberg atoms by microwave radiation, where it was found that the measured electron kinetic energies could be predicted by a classical theory of electrons drifting in an AC electric field [40]. The relevant field parameter was not solely the photon energy or field intensity, but the Ponderomotive Energy (Up) which is the energy associated with the quiver motion of an electron in an AC electric field. Equation 1.4 defines Up in terms of the electron charge e, the field amplitude E_0, the electron mass m_e, and the angular frequency of the field ω.

$$Up = \frac{e^2 E_0^2}{4 m_e \omega^2} \tag{1.4}$$

This "Simpleman's theory" explained that in the low frequency limit, differing electron kinetic energies were determined by the time that the electron is ionized and enters the classical field, accurately predicting the highest energy ATI observed at the time as 2Up [104]. Having almost caught up to the experimental results, these theoretical insights would be incapable of explaining observations already made, or soon to be in the next few years, such as the orders of magnitude enhancement in double ionization from theoretical predictions [75], the generation of harmonic orders of light beyond perturbative scalings [83], and the broad plateau in yield of the ATI peaks observed past 2Up [88].

1.2.2 Three Step Model

The three-step or semi-classical model of strong field ionization and recollision was developed in 1993 and provided an elegant solution to these outstanding problems in Strong Field physics [21, 93]. This model extended the "Simpleman's theory" to account for the trajectories which returned the electron to the parent ion after ionization. In step (1), the binding potential of an atom is suppressed by the strong electric field and the electron tunnel ionizes. (2) The electron is accelerated in the continuum by the strong field before

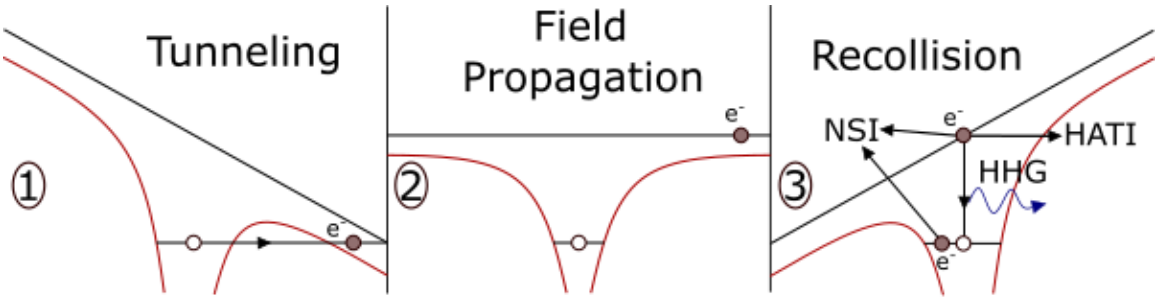

Figure 1.1: The three step model of electron recollision

The black lines represent the local electric field from the laser pulse, the red line is the total electric potential experienced by the electron. (1) the suppressed Coulomb potential allows an electron to tunnel ionize from the atom. (2) the freed electron is accelerated in the continuum, accumulating kinetic energy. (3) the electron returns to the parent ion where it can recombine to generate harmonic photons (**HHG**), collisionally excite or ionize additional electrons (**NSI**), or scatter elastically gaining additional kinetic energy in the process (**HATI**).

(3) it is driven towards the parent ion whereupon it can scatter elastically, inelastically, or recombine with the hole left in the atomic ground state. This whole process can occur in a fraction of an optical cycle, allowing for recollision energies up to 3.17Up and bursts of attosecond wavepackets. The elastic scattering generates electrons with much larger kinetic energies, the cutoff of these electrons is 10Up, and explains the plateau at high energies beyond the 2Up cutoff. The inelastic scattering explains the enhancement of the double ionization rates, in a process dubbed Non-Sequential Double Ionization (NSDI), as the recollided electron imparts sufficient energy to a second electron to doubly ionize the atom. Inelastic recollision can also drive multiple ionizations in a more generalized process called Non-Sequential Ionization. Finally, the recombination of the electron with the ion allows for the generation of light extending into the Extreme Ultraviolet (XUV) at harmonic energies of the fundamental field, called High Harmonic Generation (HHG). These three modes of studying recollision: electron spectra, photon spectra, and ion yields are worth considering individually as each reveal different aspects of this phenomena.

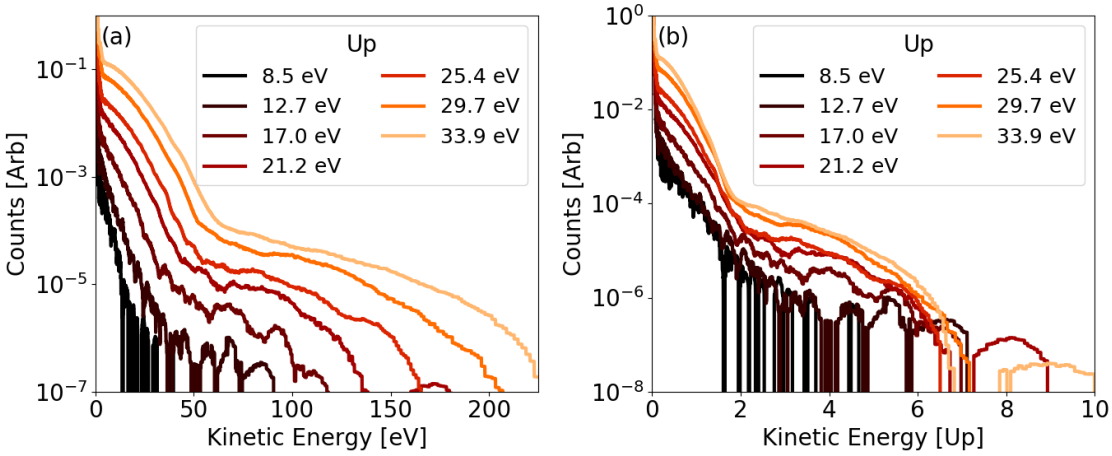

Figure 1.2: Electron Spectra

These spectra are collected with a NIR wavelength of 1.74 μm and the target species is primarily H_2O. (a) spectra for a range of Up. Two cutoffs are observed: 2Up for the direct electrons and 10Up for the recollided electrons. (b) the same spectra but with the kinetic energy scaled in units of Up demonstrating the universality of the cutoffs with Up. In these spectra the integration times were insufficient to consistently resolve the electrons up to 10Up.

1.2.3 Electron Spectra

Figure 1.2 shows the spectra for a range of Ponderomotive Energy (Up), demonstrating the common features of ATI and the plateau in yield of recollided electrons, as seen on a semi-log graph. Panel (b) makes the distinctions between these regions evident. Below 2Up the vast majority of electrons are observed and these correspond to the electrons described by the "Simpleman's Theory", which will be called the direct electrons. The yield as a function of energy falls rapidly with increasing kinetic energy, as the trajectories producing the most energetic electrons occur away from the extrema of the electric field where the tunneling ionization rate is maximized. Past 2Up, the slope of the yield versus energy shifts dramatically remaining relatively flat for a large bandwidth of electron energies. The three step model predicts the cutoff to be at 10Up which is the highest energy an electron can obtain through elastic scattering with the parent ion. In Figure 1.2 this high energy cutoff is not clearly observed due to insufficient integration times. More information about the

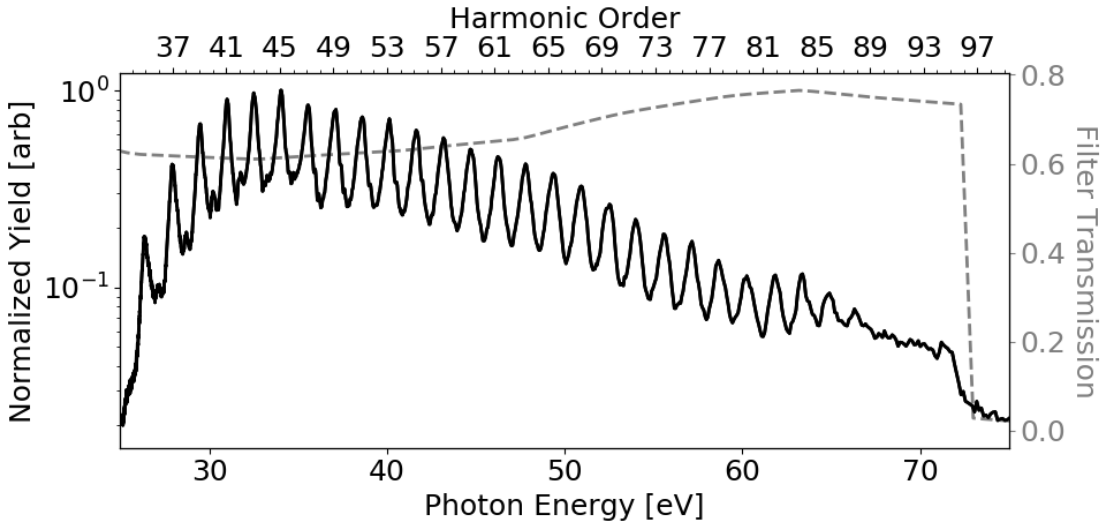

Figure 1.3: Photon Spectrum

Photon spectrum recorded for HHG in xenon with a 1.7 μm laser, collected with an XUV spectrometer and CCD camera. An aluminum filter, transmission plotted in grey, removes the fundamental beam and attenuates the signal past 73 eV. Below 25 eV, the signal is attenuated by transmission through the spectrometer. The large bandwidth of harmonics allows for the synthesis of attosecond pulses of light.

apparatus used to make this measurement can be found in Chapter 2.

In addition to these more common features, at longer NIR intensities an additional feature at low electron energies called the Low Energy Structure (LES) appears. This is a large narrow peak, typically only a few eV wide and centered at an energy of less than 5 eV. This has become associated with a series of trajectories in the three step model where the electron recollides with near 0 kinetic energy after being born at the peak of the electric field. These "soft" recollisions making up the LES stand in stark contrast to the higher energy "hard" recollisions, those observed between 2 and 10Up, in that they can constitute a significant fraction of the total electron yield, as much as 10-20%.

1.2.4 Photon Spectra

Studying the photons emitted through recollision, HHG, strips away any signal associated with the direct electrons. This allows for a more careful study of the lower energy recolli-

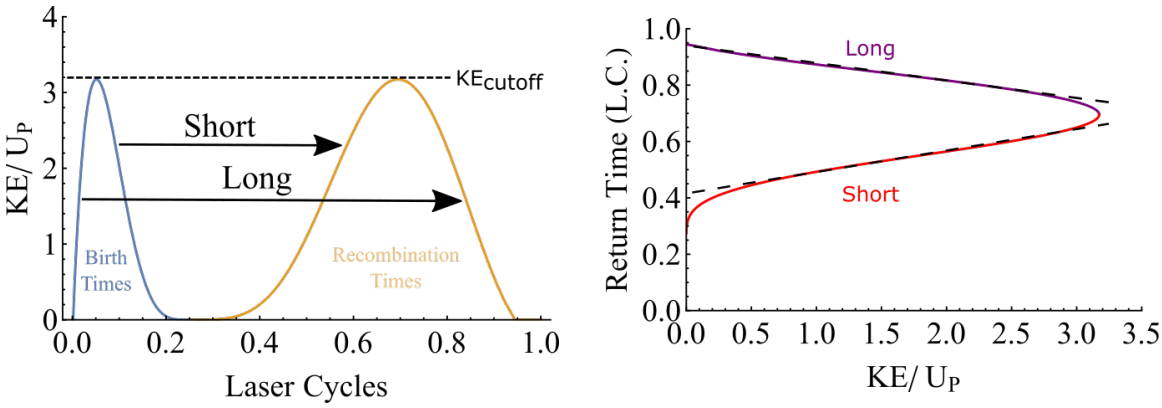

(a) Birth and return times that recombine

(b) Attochirp of short and long trajectories

Figure 1.4: Birth and return times predicted by the three step model

Only a narrow subset of ionization (birth) times result in recollision. (a) the classical trajectories of the three step model predict a unique time of recombination for a given birth time. The change in sign of the attochirp as seen in (b) allows for a clear delineation between two classes of recolliding trajectories, the short and long. Figure adapted from [43].

sions. The minimum energy associated with HHG is $n\hbar\omega$, the lowest order harmonic that exceeds the Ip of the target. The cutoff at high energy lies at the maximal recollision energy, 3.17Up, plus Ip. Typically HHG only produces harmonics at odd ordered harmonics, as opposed to ATI where the peaks are at even and odd multiples of the fundamental photon energy. The discrepancy is due to the coherent buildup of the harmonic orders across laser half cycles, as a burst of harmonics are produced at every extrema of the driving field, and the centrosymmetry of gaseous atomic targets [14]. This train of odd ordered harmonics in the frequency domain results in an Attosecond Pulse Train (APT) spaced by half a laser cycle. See Chapter 3 for more details. Figure 1.3 shows an HHG spectrum generated with a 1.7 μm laser pulse, see Appendix B for a description of the apparatus used in collecting this spectrum.

Further insights into recollision can be gained by measuring the phase of the harmonics. The following section on attosecond experiments will discuss experimental techniques that can be used to retrieve these phases. One universal feature of the APT produced via HHG is a Group Delay Dispersion (GDD) that scales with the Up of the driving field [14].

The three step model accurately predicts this so called attochirp as illustrated in Figure 1.4. The trajectories associated with the three step model will only recollide, or in this case recombine, for a narrow subset of phases of the driving field at which the electron is ionized. Each ionization time has a unique recombination time and energy resulting in a approximately linear change in phase as a function of photon energy. Two distinct classes of trajectories, the short and long, have attochirps of similar magnitude but are opposite in sign. In typical experiments involving HHG, experimental conditions are optimized to generate from the short trajectories as they are generally superior for synthesizing an APT [14]. For more information on the experimental techniques utilizing HHG to create an APT see Chapter 3.

1.2.5 Ion Yield

The final lens through which recollision can be observed is the rate of multiple ionizations as a function of laser intensity. Figure 1.5 shows the single and double ionization yields of helium exposed to a 160 fs, 780 nm laser pulse [105]. The single ionization rate has a change in slope on this log-log plot at a saturation intensity of 800 TW/cm^2 at which point the tunneling ionization probability approaches unity. Larger intensities see continued increases in the helium ionization yield at a rate of $I^{3/2}$ as a result of the increase in the focal volume size with sufficient intensity to drive tunnel ionization. The double ionization rate is orders of magnitude greater than what is predicted from a sequential process, where each electron tunnel ionizes independent of the other, as the tunneling ionization rate decreases exponentially with Ip [5]. The first Ip of netural helium is 24.56 eV, and the Ip of the ion is more than double that at 54.42 eV [63]. However, the double ionization yield appears to saturate at the same intensity as the single ion, 800 TW/cm^2, before a change in slope at 3 PW/cm^2 where the results begin to match the predictions of the sequential tunnel ionization model. This "knee" structure is ubiquitous in experiments on multiple ionizations of atoms and molecules. It is explained by the three-step model as the probability of double ionization is linearly dependent on the single ionization probability, and the probability of recollision doubly ionizing the target is orders of magnitude more likely than the sequential ionization

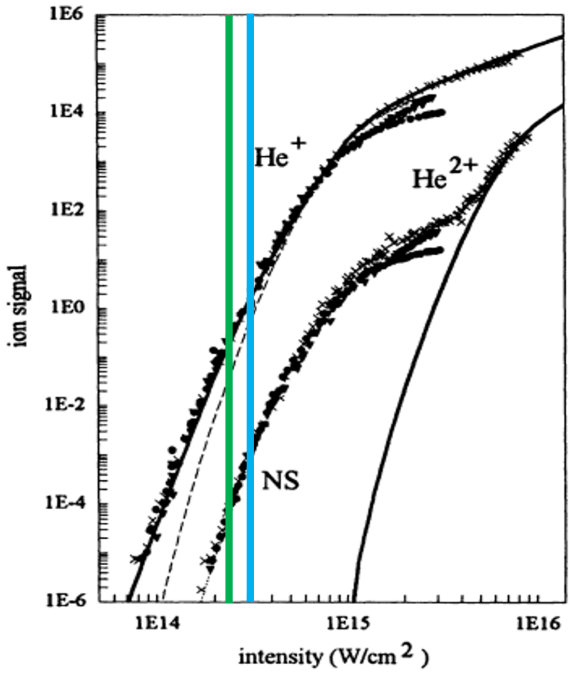

Figure 1.5: Ion yield versus intensity

Solid black lines are the predictions from the Single Active Electron approximation, where the double ionization is the result of sequential tunneling ionization events. The vertical line in blue (green) represents the intensity where the maximal recollision equals the He^+ second ionization threshold (first excited state). Adapted from [105].

mechanism until the laser is intense enough to tunnel ionize the second electron.

One of the most interesting, yet overlooked, features of double ion yield is the behavior at low intensities. The three step model predicts that the greatest energy with an electron can recollide is 3.17Up. One would expect that when this maximal recollision energy falls below the energy required to release the second electron that there would be another change in slope in the double ionization rate, see blue line in Figure 1.5. However, the second electron can be collisionally excited and then ionized by the laser pulse. So again, one would look for a change in slope where the recollision energy falls below that of the first excited state of the ionized target, green line in Figure 1.5. Presumably the collisional excitation cannot occur without sufficient energy and the bound electron will not be effectively ionized from the ground state by the laser pulse at these low intensities. Instead the rate of double ionization appears unperturbed as it falls below these thresholds, simply tracking with the

rate of single ionization. The lack of features in this region has gone unexplained for close to 30 years and represents a significant gap in the three step or semi-classical model.

1.3 Strong Field Simulator Concept

One of the greatest limitations of previous experiments in Strong Field physics is the inability to isolate the different trajectories described by the three step model. Whether the photons, electrons, or ions are measured, the data collected always represent a superposition of all the possible trajectories weighted by the ionization probability at the birth time. The original experiments by Gallagher et al. resolved different classes of trajectories at microwave frequencies [40], but observing recollision is intractable at these long wavelengths due to the diffusion of the electron wavepacket as it travels in the continuum (scales as λ^{-3}) [89]. A new generation of trajectory selective studies of Strong Field physics, within a parameter space where recollision is probable, would allow for a novel study of the three step model.

The Strong Field Simulator (SFS) is a novel concept for conducting such a campaign of experiments using a two-color field, combining a phase locked XUV-APT and NIR pulse. In an SFS experiment, the XUV-APT will replace step (1) of the three step model (the tunnel ionization step) with single photon ionization while a strong NIR field is present to drive steps (2) and (3). Changing the delay between the pulses will control which trajectories are launched, and synthesizing an XUV-APT with a pulse duration less than a tenth of a NIR laser cycle will provide a degree of specificity over the trajectories selected. Figure 1.6 illustrates the difference between traditional single color experiments and the new SFS methodology.

This experiment assumes that the electron trajectory and recollsion is insensitive to the ionization mechanism, so long as a comparable electron wavepacket is launched. The "Simpleman's Theory" suggests that the tunneling electrons are born with zero kinetic energy, and more rigorous quantum mechanical models have supported this assertion [68]. As such, it is important to generate an XUV pulse with photon energies centered on the Ip

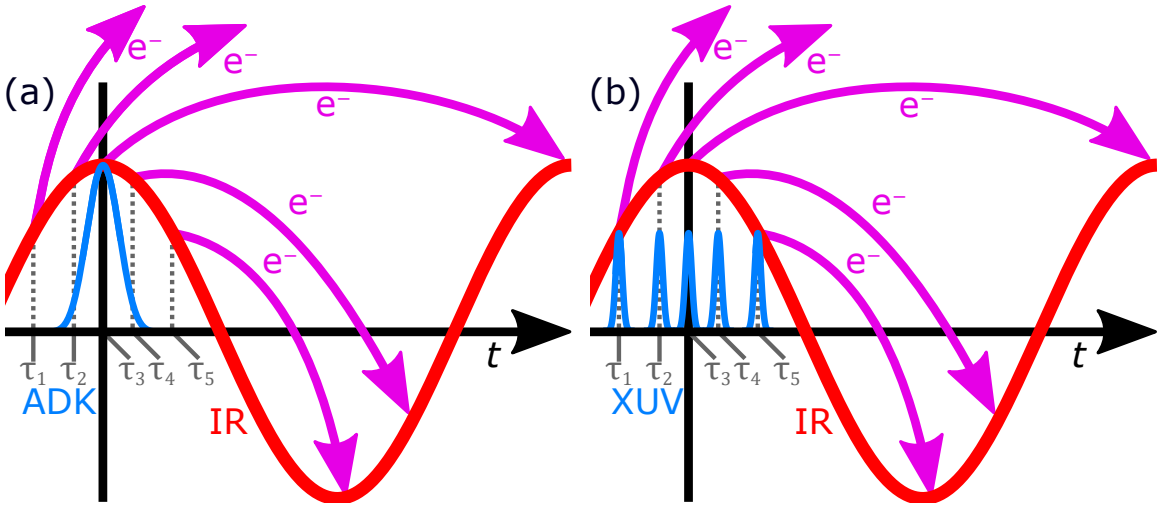

Figure 1.6: Schematic of the **SFS** principle.

(a) a traditional single color experiment. The trajectories are determined by the time of ionization, τ_i, with the probability of occurring given by the tunneling ionization rate given by the ADK theory [5]. Only certain trajectories can recollide within a laser cycle, however the experiment will measure a superposition of all possible trajectories. (b) an SFS experiment where the trajectories observed are selected by the delay of the XUV pulse. In principle all trajectories are now equally probable given the fixed rate of single photon ionization. This figure was created by Dietrich Kiesewetter.

of the target gas in order to effectively recreate, or simulate, the physics of a single color experiment. Another constraint on these experiments is ensuring that the initial ionization is driven predominantly by the XUV pulse. For NIR wavelengths, the intensities at which significant NSDI can be observed will drive some amount of tunneling ionization. Generating an XUV-APT that can ionize a larger fraction of the target gas than the NIR field is technically challenging, but is made possible by moving to longer wavelengths. Further discussion of these relative ionization rates as a function of laser wavelength can be found in Chapter 3. Figure 1.7 shows the results of computations solving the TDSE, within the parameter space of the SFS concept outlined here, to generate electron spectra for a NIR field alone and in the presence of an XUV-APT.

In Figure 1.7, the SFS wavefunctions (black dashed and red) — those launched by the XUV-APT at particular phases of the NIR field — produce electron spectra distinct from that produced by the NIR field alone (solid black). The former is fairly smooth and can

achieve larger electron kinetic energies where the latter has discernible ATI peaks. However, taking a coherent superposition of the SFS wavefunctions weighted by the tunneling ionization rate of the NIR field at the phase of the XUV pulse (cyan) returns a spectra indistinguishable from the single color NIR wavefunction. This demonstrates the potential of this SFS concept to resolve the roles of individual classes of trajectories while reproducing the results of traditional single color experiments.

The SFS will operate analogously to this computational simulation which reproduces the experimental observables by emulating the evolution of the quantum wavefunction. These experiments have all the hallmarks of prototypical quantum simulators: there is a precise initial state preparation, time evolution of the state under a comparable Hamiltonian, and measurements of quantities of interest [11]. Figure 1.7 illustrates that there is a clear mapping of the XUV-APT ionized SFS wavefunctions to their tunnel ionized counterparts. Similar to other quantum simulators, the SFS will be able to surpass traditional computational simulations in its ability to capture the dynamics of the entire quantum system. Theories of strong field recollision rely on many approximations such as there being only a single active electron, that the ion's Coulomb potential can be disregarded after ionization, and that the dipole approximation holds throughout the electron's trajectory. The SFS directly emulates the relevant physics and can reveal the limitations of these approximations in our understanding of strong field physics.

Studying electron spectra by mixing an XUV-APT with a NIR field is not a novel concept. Attosecond experiments have relied on nonlinear interactions between these disparate frequency domains to study electron interactions for two decades. The apparatus designed and built for the SFS experiments conducted in this dissertation was inspired by these previous attosecond experiments. The SFS lies at the intersection of traditional attosecond and strong field experiments. As such, it is worth exploring how these SFS experiments compare to, and extend from, previous attosecond experiments.

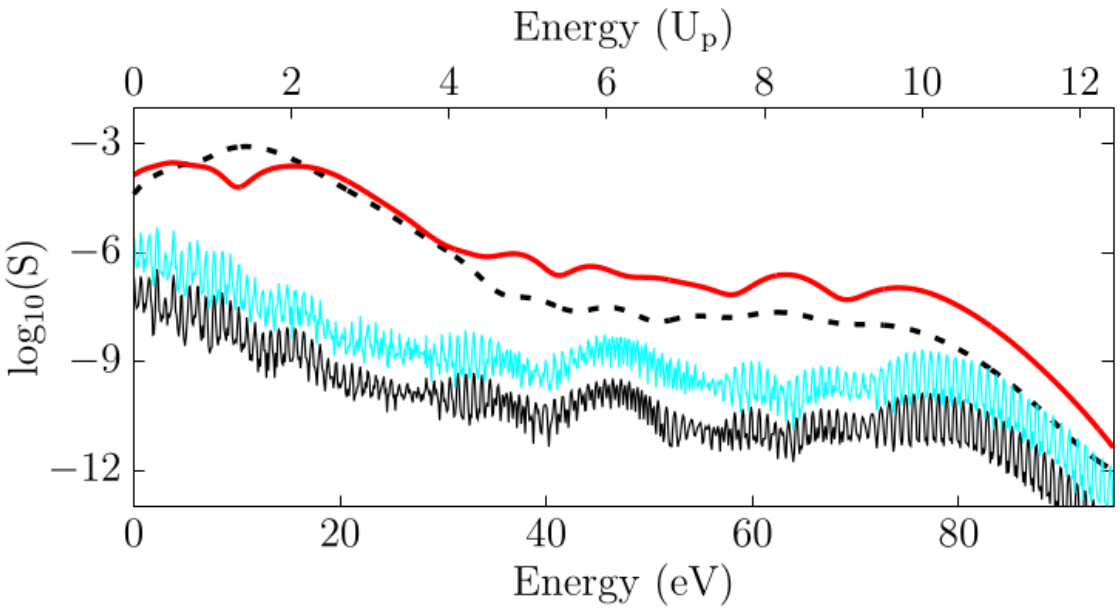

Figure 1.7: Results of TDSE simulations of SFS trajectories

These simulations are done with a 1.6 μm laser pulse, argon as the atomic target, and an XUV pulse centered at the Ip. The black lineout is the energy resolved electron yield versus kinetic energy for NIR pulse in isolation. The black dashed (red solid) curve is the result of an SFS wavefunction where the XUV pulse is present and centered at the maximum (zero) of the NIR electric field. The cyan curve is a coherent superposition of many SFS wavefunctions for various relative delays of the XUV and NIR pulses weighted by the associated tunneling ionization probability in the single color experiment. This figure was created by collaborators Jens Bækhøj and Kenneth Schafer.

1.4 Attosecond Experiments

To understand traditional attosecond experiments, the formulation of the Strong Field Approximation (SFA) by Mairesse and Quéré [78] for electron wavepackets ionized by an XUV pulse is particularly useful. The SFA can be understood as applying the Keldysh approximation to TDSE simulations in order to numerically solve for the dynamics of continuum electrons in the presence of NIR fields [4]. Using atomic units, the transition amplitude to a final electron state of velocity $\mathbf{v}$ for delay τ between the XUV and NIR fields is defined as:

$$a(\mathbf{v},\tau) = -i\int_{-\infty}^{\infty} dt e^{i\phi(t)}\mathbf{d}_{\mathbf{p}(t)}E_X(t-\tau)e^{i(W+Ip)t} \tag{1.5}$$

Where $\mathbf{d}_{\mathbf{p}(t)}$ is the dipole moment for transition from the ground state to a continuum state with canonical momentum $\mathbf{p}(t)$, E_X is the electric field of the XUV pulse, W is the kinetic energy $v^2/2$, and Ip is the Ip of the target species. The product of E_X, $\mathbf{d}_{\mathbf{p}(t)}$, and $e^{i(W+Ip)t}$ describes the electron wavepacket launched by the XUV pulse, and the role of the NIR field is contained within the phase term $\phi(t)$ defined below:

$$\phi(t) = -\int_{t}^{+\infty} dt'[\mathbf{v}\cdot\mathbf{A}(t') + \mathbf{A}^2(t')/2]] \tag{1.6}$$

Where $\mathbf{A}$ is the vector potential of the NIR field. Using the typical experimental conditions of a linearly polarized NIR laser with a pulse duration much longer than the oscillation period, this phase term can be broken into three pieces.

$$\phi_1(t) = -\int_{t}^{+\infty} dt' U_p(t') \tag{1.7}$$

$$\phi_2(t) = (\sqrt{8WUp}/\omega_L)\cos\theta\cos\omega_L t \tag{1.8}$$

$$\phi_3(t) = -(Up/2\omega_L)\sin 2\omega_L t \tag{1.9}$$

Where Up is the ponderomotive energy as defined in Equation 1.4, ω_L is the angular frequency of the NIR laser, and θ is the angle between the laser polarization and detector axis. For most attosecond experiments, relatively low intensity NIR pulses are used such that Up is small and the phase $\phi(t)$ can be approximated by $\phi_2(t)$ alone.

1.4.1 Perturbative Wavepacket Mixing

In the limit that Up is very small, $e^{i\phi_2(t)}$ can be Taylor expanded to $1+i\phi_2(t)$ in which case Equation 1.5 takes on the functional form of a Fourier Transform:

$$a(\mathbf{v},\tau) = -i\int_{-\infty}^{\infty} dt \mathbf{d}_{\mathbf{p}(t)} E_X(t-\tau)\left(1 + i\frac{\sqrt{2WUp}}{\omega_L}(e^{i\omega_L t} + e^{-i\omega_L t})\right) e^{i(W+Ip)t} \tag{1.10}$$

Where θ is taken to be 0, meaning the laser polarization is along the detector axis. The electric field of the XUV field, E_X, can be described in the frequency domain as:

$$E_X(t) = \int_{-\infty}^{\infty} d\omega U(\omega) e^{i\Phi(\omega)} e^{i\omega t} \tag{1.11}$$

Assuming $\mathbf{d}_{\mathbf{p}(t)}$ is constant, which can safely be done for many attosecond experiments where $\hbar\omega_X >> Ip$, Equation 1.10 can be simplified to a sum of three terms [17]:

$$\begin{aligned} a(\mathbf{v},\tau) \approx e^{-i\omega_v \tau}\Big[&U(\omega_v)e^{i\Phi(\omega_v)} + \\ &i\frac{\sqrt{2WUp}}{\omega_L}\left(U(\omega_v+\omega_L)e^{i\Phi(\omega_v+\omega_L)}e^{-i\omega_L\tau} + U(\omega_v-\omega_L)e^{i\Phi(\omega_v-\omega_L)}e^{i\omega_L\tau}\right)\Big] \end{aligned}$$

Where $\omega_v = W + Ip$. Equation 1.4.1 shows that in this limit of small Up, the NIR field allows for single photon electron transitions in the continuum. For a typical APT which consists of only odd ordered harmonic, the NIR will populate sideband electron energies between the XUV harmonic orders. In other words, at these sidebands $U(\omega_v) = 0$ so the measured signal, $|a(\mathbf{v},\tau)|^2$, will simplify to:

$$\begin{aligned} |a(\mathbf{v},\tau)|^2 = &\frac{2WUp}{\omega_L^2}\left[U^2(\omega_v+\omega_L) + U^2(\omega_v-\omega_L) + \right. \\ &\left. U(\omega_v+\omega_L)U(\omega_v-\omega_L)cos\left(\Phi(\omega_v+\omega_L) - \Phi(\omega_v-\omega_L) + 2\omega_L\tau + \Theta\right)\right] \end{aligned}$$

This interaction is depicted in Figure 1.8 where the single photon transitions of two

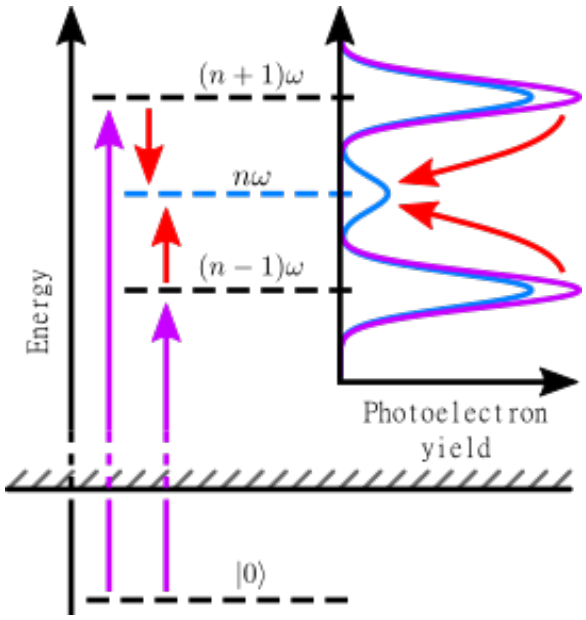

Figure 1.8: Cartoon of the RABBITT interaction

The odd ordered harmonics from a typical XUV-APT ionizes electrons to continuum states separated by 2ω. Adding a weak NIR field drives transitions between continuum states causing sidebands to appear where the even ordered harmonics would reside. The pair of interfering pathways causes the sideband yield to oscillate as a function of delay between the XUV and NIR fields at twice the frequency of the fundamental field. Adapted from [59].

adjacent harmonics, $(n \pm 1)\omega$, lead to an interference signal at a sideband electron energy, $n\omega$. As the delay between the NIR and XUV fields is scanned, the yield of electrons at a given sideband oscillates with a frequency of $2\omega_L$. The relative phases measured between sideband orders are proportional to the phases between pairs of harmonics from the original XUV-APT, $\Phi(\omega_v + \omega_L) - \Phi(\omega_v - \omega_L)$. Attosecond experiments of this variety are called Reconstruction of Attosecond Beating by Interference of Two-Photon Transitions (RABBITT), and this technique was first used to measure the relative phases between harmonics as a form of XUV-APT pulse metrology [87]. Additionally, atomic or molecular resonances in the continuum can cause significant changes in $\mathbf{d}_{\mathbf{p}(t)}$. Using a well characterized XUV-APT, RABBITT can measure the phase of these resonant features [62].

1.4.2 Attosecond Streaking

For higher intensity NIR pulses, when $W >$Up$> \omega_L$, the Taylor expansion of $e^{i\phi_2(t)}$ loses its accuracy. Correspondingly, the quantum description of wavepacket mixing yields to a more classical picture of the electron distribution being accelerated by the NIR, or streaked. Assuming the XUV pulse has a gaussian lineshape and is much shorter than the period of the fundamental NIR field, $|a(\mathbf{v},\tau)|^2$ can be approximated using the saddle point method [52]:

$$|a(\mathbf{v},\tau)|^2 \propto |\mathbf{d}_{\mathbf{p}(\tau)} E_X(\tau)|^2 \exp\left[-\left(\frac{\sqrt{8WUp}}{\omega_L}\cos\omega_L\tau + W + Ip - \Omega_X\right)^2 T^2\right] \tag{1.12}$$

Where Ω_X is the carrier frequency of the XUV pulse, and T is the XUV pulse duration. In attosecond streaking the NIR field shifts the distribution of harmonics as a function of delay such that the yield at a particularly electron kinetic energy oscillates once per laser cycle. Classically, this can be understood as the electrons being accelerated or decelerated by the NIR field depending on its phase at the moment of ionization. This type of experiment is better suited for characterizing an APT with even and odd ordered harmonics or an Isolated Attosecond Pulse (IAP) where the distribution of photon energies is continuous. Such an APT or IAP can be synthesized with HHG under particular conditions [14]. Figure 1.9 shows a streaking spectrogram for an APT of even and odd ordered harmonics generated by an 800 nm laser. The envelope of the electron distribution shifts towards larger or smaller kinetic energies depending on which half cycle of the NIR field the XUV-APT overlaps. This spectrogram was collected with the attosecond interferometer described in Chapter 2 and was the first successful attosecond measurement after the apparatus was commissioned. Similar to the RABBITT technique with APTs, streaking was originally developed to characterize an IAP [27]. Later experiments have utilized streaking to study resonant electron dynamics in the continuum, again similar to RABBITT.

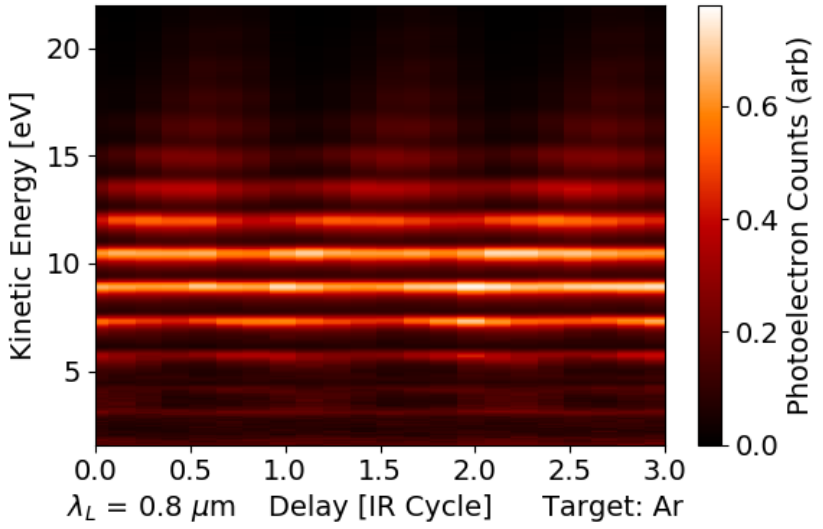

Figure 1.9: Streaking measurement at 800 nm

A spectrogram for a streaking experiment conducted with an 800 nm laser using argon as the atomic target. The distribution of electron kinetic energies is shifted by the electric field of the laser as a function of delay, leading to an oscillation once per laser cycle.

1.5 Previous Work

An initial series of experiments were conducted by Dietrich Kiesewetter, a previous graduate student in the DiMauro group, intending to test the SFS concept with helium as the target. These experiments were conducted using an interferometer designed for general attosecond experiments involving a XUV-APT and NIR pulse, more details can be found in [59, 96]. Unfortunately, the limitations of the apparatus prevented the two conditions for an SFS experiment from being fulfilled, see Section 1.3. The XUV pulse had a bandwidth of ∼20 eV, and the mean energy was ∼10 eV greater than the Ip of helium. In addition, at the NIR wavelengths used, 800 nm and 1.3 μm, the background ATI signal from tunneling ionization exceeded the XUV single photon ionization yield for all but the smallest NIR intensities. No clear signals that could be attributed to recollision events were observed, however, these experiments were instrumental in identifying essential improvements needed for the work in this dissertation to be successful.

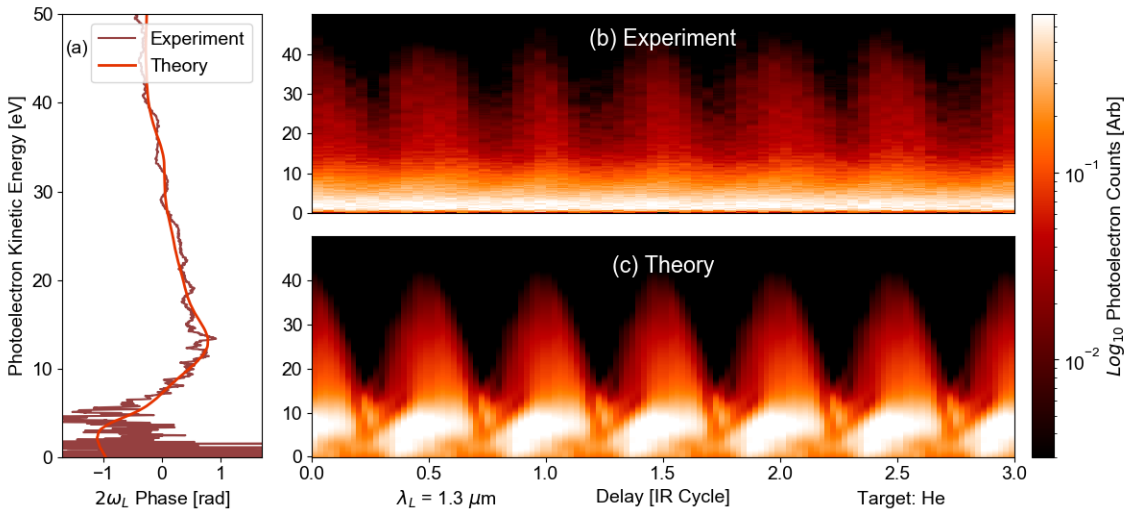

Figure 1.10: Results of previous SFS experiments and TDSE simulations

(a) is the phase extracted from analyzing the oscillation at twice the NIR laser frequency within a Fourier decomposition. The experiment and TDSE simulations, theory, show excellent agreement. (b) the electron spectrogram showing a streaking type behavior even with a comb of only odd orderd harmonics. The background tunneling ionization obscures the features at low kinetic energies. (c) simulations from TDSE simulations conducted by Jens Bækhøj and Kenneth Schafer. Adapted from [59].

Figure 1.10 presents some of the key results from this earlier work. The fundamental NIR wavelength is 1.3μm, the Up is 3.5 eV, and the XUV-APT consisted of a comb of odd ordered harmonics. Regardless, at this large of Up streaking type behavior was observed, though the dominant frequency of oscillation was twice per laser cycle. TDSE simulations carried out by collaborators Jens Bækhøj and Kenneth Schafer were able to reproduce many features in the spectrogram. A Fourier Transform of the spectrograms along the delay axis allowed for a measurement of the oscillation phase versus kinetic energy, shown in panel (a), revealing excellent agreement between the theory and experiment. At large kinetic energies, >15 eV, the slope in oscillation phase resulted from the XUV-APT's attochirp, see Section 1.2.4. Below 15 eV, the slope was attributed to effects of the atomic potential. A key finding in these experiments was that the maximum observed kinetic energy, or *cutoff*, could be accurately predicted by a trivial extension of the "Simpleman's Theory" for photoelectrons born with non-zero initial kinetic energy.

A wider search of the literature yields only a few efforts to conduct an SFS type experiment. One example conducted in 2008 examined the electron yield using a Velocity Map Imaging detector, capable of resolving the total electron momentum, with a laser wavelength of 800nm [81]. The XUV-APT consisted of odd and even harmonics and was centered at a photon energy only 1.2 eV above helium's Ip. Here the effects of rescattering were believed to have been observed by comparing the results of TDSE simulations, classical models, and the experimental results. Diffractive features and other structures at electron momenta opposite in sign to the instantaneous vector potential at ionization were attributed to coherent electron scattering off the atomic potential. However, background contamination, predominantly by water, prevented further studies at higher NIR intensities where the effects of recollision are more pronounced.

A distinctly different class of experiments and simulations approaching the SFS methodology have been conducted where the photon spectrum produced by HHG seeded by an XUV-APT is studied [8, 38, 39, 92]. These efforts have shown that the SFS concept of using an XUV-APT to replace tunneling ionization in the three step model is viable, as recombination of the electron with the parent ion is still observed. However, using HHG to study strong field ionization has its limitations due to the macroscopic effects of phase matching the harmonics in a bulk gas sample. Studies of electron and ion yields can generally be considered single atom or molecule experiments. Interestingly, these works suggest that new electron trajectories are viable in the seeded process, as electrons with momenta opposite the NIR field at ionization can be produced [92]. The presence of these 'uphill' electrons would have interesting implications for the SFS experiments conducted in this dissertation.

1.6 Motivation

As already highlighted, the experiments conducted in this dissertation are distinct from these previous efforts by virtue of meeting the SFS conditions. This means that the results of these experiments can be directly compared to the expectations of the three step model,

creating a simulator of single color, low frequency, strong field experiments. In principle, all of the results in the photon, electron, and ion measurements discussed in Section 1.2 should be reproducible with the SFS, with an added dimension corresponding to the phase at which the electron is ionized. This approach can provide insight into the effects of the Coulomb potential in recollision not captured by the traditional three step model or SFA, which assume the field of the parent ion is negligible compared to the laser field for ionized electrons. Experiments conducted in the microwave domain, at a frequency of 38.8 GHz (7.7 mm wavelength), have shown that electron recombination can occur with energies far exceeding the maximum of the "Simpleman's Theory" [94]. In this work, this discrepancy could be resolved by adding corrections associated with the Coulomb potential of the parent ion. This points to a possible explanation for the lack of features in the NSDI yield of helium at low field strengths discussed in Section 1.2.5.

NSDI is of particular interest in these SFS experiments as an experimental probe of the effects of electron correlation. Electron correlation is essential to our understanding of chemistry [101], condensed matter physics [6], and even strong field physics [34]. NSDI in helium is a elementary test bed for theories of electron correlation with only two electrons and a nucleus interacting in an external field. SFS experiments studying NSDI in helium, or non-sequential multiple ionizations in larger atoms, can provide greater insights into the effects of electron correlation in the simplest atomic systems, and inform theories of electron correlation in more complex molecular and condensed systems of more practical significance [34].

1.7 Outline

Having introduced the relevant history, models, and prominent results of Strong Field physics and the novel approach of the SFS concept, this dissertation will proceed as follows. First the new apparatus designed and built for SFS experiments will be described in Chapter 2. The methods used to generate an XUV-APT that fulfills the SFS requirements — a narrow bandwidth centered at the Ip of noble gas atoms and sufficient flux to dominate

the total number of ionization events — will be explored in Chapter 3. Chapter 4 will report on the SFS experiments conducted with helium as the atomic target, and Chapter 5 for another set of experiments with argon. A summary of the experimental results, limitations, and future possibilities will conclude this dissertation in Chapter 6. Additionally, Appendix A provides instructions on operating the vacuum system, B reviews diagnostic testing done with the new pulsed gas valve used for HHG, and C presents additional results for experiments conducted with neon as the SFS target.

Chapter 2
Experimental Methods

"All my means are sane, my motive and my object mad."

— Herman Melville, Moby Dick

2.1 Overview

In this chapter, I will the discuss the general requirements of any interferometer mixing XUV and NIR light; the particular requirements for a system to achieve SFS conditions; in depth descriptions of the laser, vacuum, optical, and detector systems built for these experiments; and a summary of the data analysis pipeline.

2.1.1 Building an Attosecond Interferometer

There are a variety of challenges in building an interferometer between XUV and NIR light. The XUV light is strongly absorbed by many materials, including the earth's atmosphere and typical glasses used to make transmissive optics. This imposes the need to generate and transport the XUV light in a vacuum environment. Even typical reflective optics have poor efficiency in this domain, and so the best approach is to reduce the number of optics the XUV interacts with to as few as possible. A large flow of gas into the vacuum system is required for optimal HHG and so large TMPs are required to maintain some semblance of vacuum during operation. These pumps can produce mechanical vibrations which then reduces the stability of the interferometer, reducing the resolution of the experiment. This trend only continues, with various requirements creating competing constraints for optimal performance of the total system.

Achieving sufficient intensities to drive HHG requires an ultra-fast laser system with millijoule pulse energies. Typical lasers are insufficient, and so amplifier systems using Chirped Pulse Amplification (CPA) are essential though they reduce the repetition rate of the laser system by orders of magnitude, compared to the oscillator which seeds the CPA. In the interferometer, maintaining the shortest pulse duration of the NIR light keeps the intensity high, and so care must be taken to minimize the GDD accumulated from each optic. Some means of controlling the delay between the two fields is required and typically added to the NIR arm of the interferometer. Finally, some means of focusing the two beams at the same position in space is required to drive the non-linear interaction between the fields that provides the attosecond resolution to the experiment. Achieving all of this is required of any attosecond experiment, but the requirements to do an SFS experiment are more stringent as outlined in the text to follow.

2.1.2 Desired Improvements

After previous work to implement an SFS experiment by Dietrich Kiesewetter, for which he used a more general purpose attosecond beamline, it was apparent that a new apparatus optimized for SFS was needed. Primary targets were set, where substantial improvements in each were deemed essential.

1. High passive interferometric stability for making attosecond measurements.
2. Low background signal from contaminant gases in the detector.
3. High XUV flux to maximize measurement count rate.

Each of these goals were addressed with a multi-pronged approach as outlined below.

Interferometric Stability

The temporal resolution of any measurement of sub-cycle strong field phenomena with a two color field, like the SFS approach, is ultimately limited by the pulse duration of the ionizing radiation. However, the limiting constraint in most attosecond experiments is actually the

repeatability of delivering the two colors of light with an identical phase delay between them [18]. This requirement motivates using a single IR laser source to coherently drive both the strong field and an upconversion to XUV frequencies called HHG, essentially an interferometer that requires a highly nonlinear process in one arm. The biggest challenge then becomes engineering an interferometer that is stable on attosecond timescales, or nanometer lengthscales [18, 49, 108].

Instabilities in the path lengths occur on two different timescales. On sub-second scales the changes are largely the result of mechanical vibrations from vacuum pumps and environmental sources. These sub-second instabilities are best addressed fundamentally in the design of the apparatus. The optimal solution for eliminating environmental vibrations is floating the optical tables, however the central laser laboratory with adjacent target area design of the DiMauro lab space precludes this due to safety concerns. The next best solution is to mount the interferometer on as massive platform as possible, relying on the mass to damp the amplitudes of any mechanical vibrations. This approach also addresses vibrations from the attached vacuum equipment. The SFS is mounted on a 48"x96"x18" (WxLxD) optical table weighing approximately 1 ton. The entire vacuum system was designed to sit low on the table to minimize the height of optical posts, with the idea being that taller posts make for larger deviations as a result of vibrations.

For longer timescales, those greater than a second, temperature fluctuations in the room and heating from the high powered laser will cause thermal expansion/contraction of the optics and their mounts resulting in drifts in the interferometer path lengths. These thermal effects, in addition to air currents causing transient instabilities, can be minimized by placing enclosures around the optics and allowing the interferometer to warm up after introducing the laser but prior to making any measurements. The performance of the laser itself can change over time, with pointing deviations appearing as slow interferometric drifts, and this effect can be reduced by placing the apparatus as close as possible to the laser system in addition to active stabilization of the laser pointing. Further improvements in stability require an active stabilization of the interferometer scheme based on feedback from some measure of the path length difference of the interferometer [108]. Active interferometer

stabilization was not implemented for the experiments described in this dissertation, but in principle the system was designed for this feature to be added in the future.

Detector Contamination

The SFS is designed to conduct studies for targets in the gas phase and the detector is capable of both Electron Time of Flight (eTOF) and Time-of-Flight Mass Spectrometry (TOFMS), even simultaneously in the coincident mode of operation. Generally TOFMS by its nature is robust against contaminants in the chamber, so long as spectra are taken with and without the target gas for background subtraction. However, there are circumstances where multiple ion species have nearly identical mass-to-charge ratios and measurements of these can greatly benefit from reducing contaminant gases in the chamber. For eTOF, it is essential to ensure that the the electrons captured are actually originating from the target of interest and not a contaminant species.

There are three major sources of contaminants in the SFS, each tackled very differently. The first is the cleanliness, or lack thereof, of the chamber itself. The detector is capable of reaching pressures on the order 10^{-10} Torr with the the vacuum hardware attached and an extended bakeout of the system. For many experiments this is sufficient to carry out both eTOF and TOFMS, however studies of Non-Sequential Double Ionization (NSDI) in helium can require a further order of magnitude reduction in hydrogen concentration. This can be resolved with use of the attached Titatnium Sublimation pump. Additionally, the ionization rate of contaminants can be dramatically reduced by moving to longer wavelengths for the IR laser. Approaching the Near Infrared (NIR), large ponderomotive energies to drive recollision can be generated with intensities so low that the ionization of lower Ip contaminants is irrelevant for targets such as helium or neon.

The second source of contaminants is gas injected into the vacuum system to generate the XUV light through HHG. Typical gas loads in the generation chamber are of order mTorr, and transmitting the XUV light requires the use of a vacuum aperture as opposed to a glass window separating the chambers. Minimizing conductance to the detector is best accomplished by shrinking this vacuum aperture as much as possible. The SFS was designed

with the vacuum aperture easily swappable and readily accessible inside the generation chamber. In this way, the vacuum aperture can be tuned to be as small as possible while still transmitting the entirety of the XUV beam.

The last source of contaminants is in the delivery of the target gas into the detector chamber. These can come from leaks in the gas delivery lines out of vacuum or may already be present in the gas source itself. The gas delivery lines can be baked to drive desorption, portions can be sufficiently cooled to freeze out contaminants, and inline filters can trap particular species. All of these techniques were employed in these experiments to remove as much of the contaminant species as possible.

XUV Flux

As we are pumping these strong field measurements with ionizing XUV light, the flux of this radiation will dictate the count rate of these experiments. So maximizing XUV flux is essential to conducting these measurements before slow interferometric drifts disturb the results. The HHG process is highly nonlinear with numerous factors influencing the total harmonic yield, but for the sake of this discussion it is reasonable to reduce these to three parameters to optimize: power of the laser driving HHG, pressure-length product of the interaction region, and transport efficiency of the XUV through the apparatus [14]. The power of the IR laser is set by the technical capabilities of the laser system, and a significant fraction of this finite power has to be sent directly to the detector to provide the strong field. Previous iterations of this experiment showed that the biggest gains in power for HHG are made by minimizing this fraction. The SFS was designed to use a spherical focusing mirror for the XUV and IR fields with a factor of two to three greater demagnification than previous experiments, increasing the intensity of light for equivalent laser power. Where previous experiments required sending as much as 80% of the IR light straight to the detector, the current SFS apparatus can be run with only 40% (tripling the power that can be sent to HHG).

The pressure-length product of the interaction region for HHG is a function of both the laser focal geometry and the generating gas source [14]. Using a longer focal length

optic, 375 mm, for the laser will increase the length over which there is sufficient intensity to generate harmonics. A pulsed gas valve was chosen to inject the generating gas into vacuum, as the low duty cycle reduces the total gas load on the vacuum system by orders of magnitude as compared to a continuous gas jet of similar dimensions. This pulsed gas valve allows for both increased interaction pressure and length, while keeping the gas load low enough to prevent damage to the vacuum pumps. Recall from the previous section that this chamber pressure has a direct impact on the contamination of the detector.

2.1.3 My Contributions

The building of the experimental apparatus for these SFS experiments was the work of several years and I am proud to having carried this experiment through the entirety of the project life cycle. This process started with an empty space after I renovated the lab in room 4121 of the Physics Research Building to accommodate a new generation of experiments. I was responsible for CAD renderings of the apparatus and budget proposals for purchasing equipment through assembly and integration of the various systems to benchmarking its performance and finally the collection and analysis of experimental data.

I was primarily responsible for maintaining the laser system for the duration of these experiments. The detector chamber was inherited from previous projects, though substantial modifications were made by myself to the optical, vacuum, and detector components contained within. I designed and built the vacuum and optical systems, with small contributions by other graduate and undergraduate students under my direction. Niko Stamos designed brackets for mounting the recombination chamber to the optical table, and assisted with collections and analysis of data for pump-down curves of each vacuum chamber. Dina Eissa assisted with the design and initial testing of the vacuum bake-out system. Qiaoyi Liu programmed the final bake-out sequence, assisted with much of the assembly of the vacuum chambers, and analyzed the data from our studies of interferometric stability. Dietrich Kiesewetter had provided CAD drawings for the custom mount of the XUV Mirror and many fruitful conversations in the early stages of the design of the vacuum and optical systems. Unless otherwise noted, I was responsible for the rest of the work in this chapter.

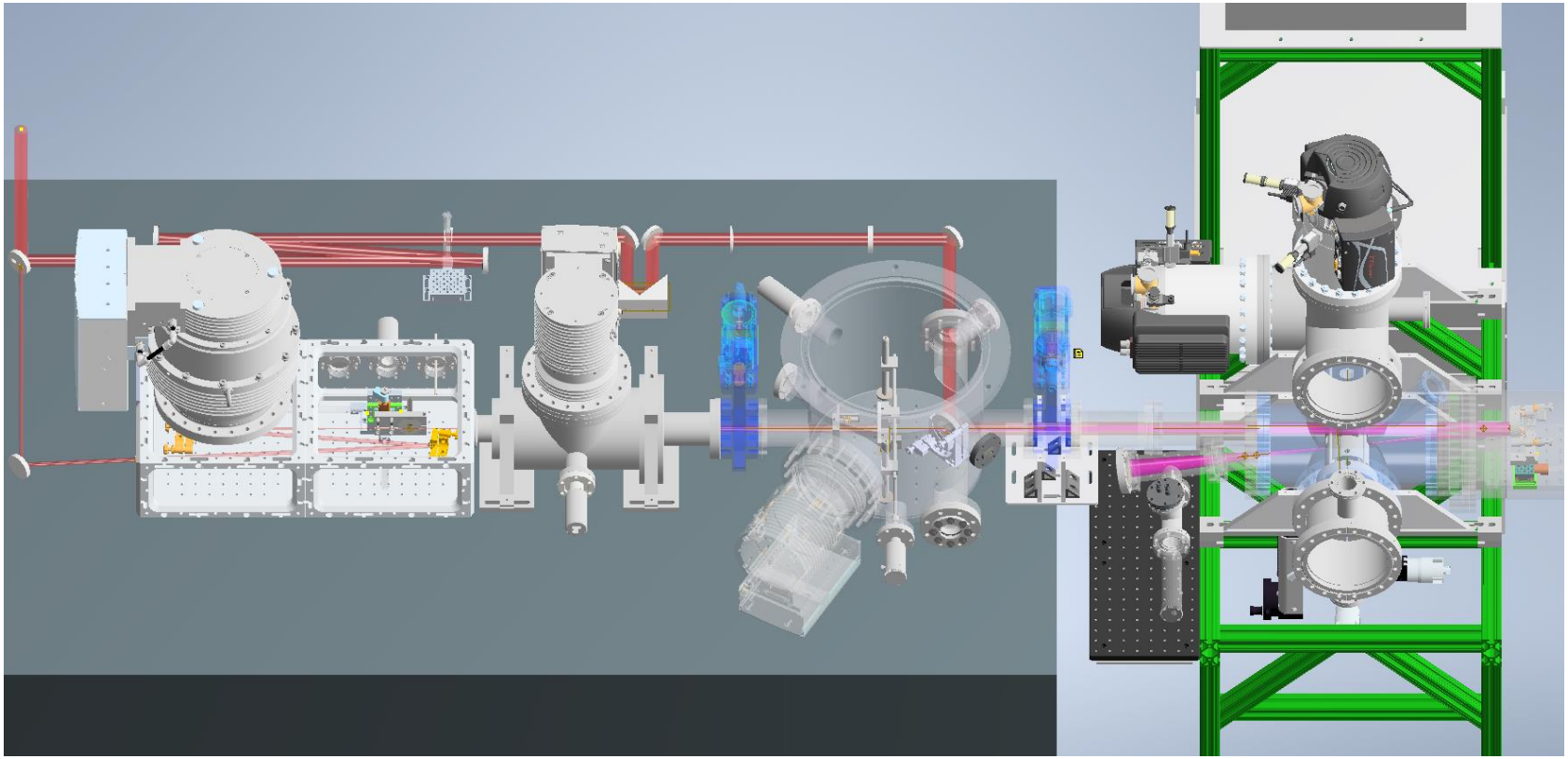

Figure 2.1: CAD design of the SFS

The apparatus for the SFS experiments described in this dissertation. The entirety of the design, build, and testing required about 2.5 years of effort. Everything mounted on the optical table was designed, fabricated, and assembled specifically for this experiment. The detector chamber shown on the green cart is inherited from previous experiments in the DiMauro group with significant updates for the SFS experiments. The NIR beam path is shown in red, and the violet profile represents the XUV light.

Parameter	Value
Center Wavelength	800 nm
Average Power	12 W
Pulse Duration	55 fs
Repetition Rate	1 kHz
Energy Stability	0.75% rms over 24 hrs
Pointing Stability	< 7 μrads rms
Beam Diameter	12 mm ($1/e^2$)
Spatial Mode	TEM_{00} $M^2 < 1.45$
Polarization	Linear, Horizontal

Table 2.1: Spitfire Ace PA specifications

2.2 Light Source

The most important technology to the successful development of an SFS experiment is the ultra-fast laser system. These experiments would not have been possible without the continued development of Ti:Sapphire amplifiers with ever greater pulse energies at high repetition rates. Although these experiments are best done further in the NIR than a Ti:Sapphire system can produce, the most efficient method for producing laser like pulses at the wavelengths, pulse energies, durations, and repetition rate required is an Optical Parametric Amplifier (OPA) pumped by a Ti:Sapphire laser. Future developments in laser technology in the NIR will allow for further improvements to SFS experiments.

2.2.1 Laser System

The workhorse for this experiment is the Sptifire Ace PA laser system from Spectra-Physics, now a subsidiary of MKS Instruments [99]. See Table 2.1 for specifications. The seed is provided by a MaiTai SP set to 22 nm of bandwidth centered at 800 nm with a repetition rate of 84 MHz [98]. This is amplified by a Ti:Sapphire regenerative amplifier pumped by an Empower 45 from Spectra Physics, a pair of Pockel's Cells pulse pick down to a 1 kHz repetition rate. Afterwards, the power is approximately 7.5 W and is further amplified in a second Ti:Sapphire crystal in a single pass stage to a final uncompressed power of 15.2 W. The uncompressed output is transported $\sim$4 m to the target room where the experiment is

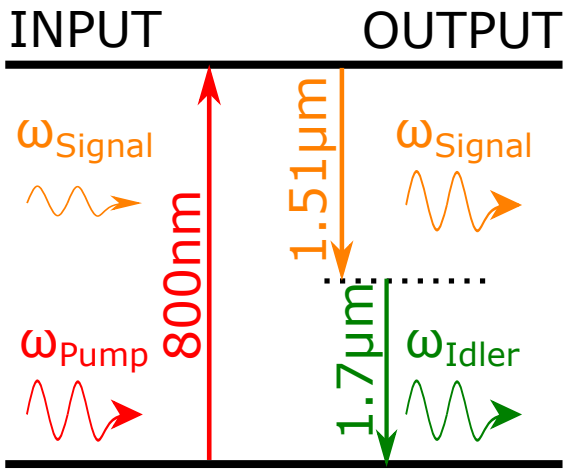

Figure 2.2: Optical Parametric Amplification

Schematic of the OPA process used to generate 1.7 μm light from an 800 nm source. Mixing the pump and signal wavelengths in a nonlinear crystal produces a seeded Difference Frequency Generation process resulting in amplification of the signal and production of idler wavelength.

conducted, and is compressed to a duration of 55 fs with 82% transmission efficiency for a final power of 12.4 W. A GuideStar II beam steering device is used to actively stabilize the pointing of the uncompressed beam into the compressor. This dramatically improves the beam pointing downstream through the OPA and consequently the pointing of the OPA output into the interferometer.

2.2.2 Optical Parametric Amplification

To create a short pulse in the NIR, the full 12.4 W of compressed 800 nm light is sent into a HE-TOPAS from Light Conversion [20]. An OPA relies on seeded Difference Frequency Generation to down-convert light of one color into a pair of laser like beams of two other colors whose summed photon energy is equal to that of original source, see Figure 2.2. In the HE-TOPAS, each amplification stage is seeded by the shorter wavelength to be produced, the signal, and generates commensurate amounts of the longer wavelength, or idler, light. This OPA provides a tunable source of NIR light from 1.1 μm to 2.0 μm. From idler wavlengths of 1.7 - 1.74 μm, at which the SFS experiments were conducted, the OPA

generated pulse durations of 60 fs and energies of 2.8 mJ at the same 1 kHz repetition rate as the 800 nm source. Subsequently, a dichroic mirror removes the signal from the idler beam which is transported to the optical table where the SFS resides ($\sim$ 2 m). The idler beam is p-polarized with respect to the optics in the interferometer, and will point along the TOF axis of the detector.

2.3 Vacuum System

The vacuum system for the SFS consists of 4 vacuum chambers, 2 dry roughing pumps, 3 magnetically levitated Turbomolecular Pump (TMP)s, 2 hybrid bearing TMPs, in addition to assorted vacuum gauges, gate valves, and feedthroughs. The system was designed to be mounted directly to the optical table with a low profile, so as to allow the mass of the optical table to dampen mechanical vibrations for the sake of interferometric stability. All of the individual chambers in the vacuum system are capable of reaching Ultrahigh Vacuum (UHV) pressures, defined here as pressures $< 10^{-8}$ Torr. The vacuum system can most easily be separated into two sub-systems populated by individual chambers based on the dry roughing pump used to back the chambers. Both roughing pumps are multi-stage roots-vane pumps from the Leybold EcoDry product line, and were selected for their high throughput, oil-free, maintenance-free, and low noise operation. Both pumps have a quoted base pressure of $\geq$ 23 mTorr, but ultimate pressures as low as 10 mTorr have been observed in this system. Both roughing pumps are housed on a trapeze shelf suspended from the ceiling of the laboratory in order to maximize floor space for equipment and through traffic.

For the sake of the rest of this chapter, *typical operation* is defined as the experimental conditions in which a measurements are made. This means the gas sources in the Generation and Detector chambers are open, and the base pressures of the chambers prior to introducing the gases are low enough to be irrelevant (no leaks virtual or otherwise). Also, pumping speeds are quoted for nitrogen unless otherwise stated.

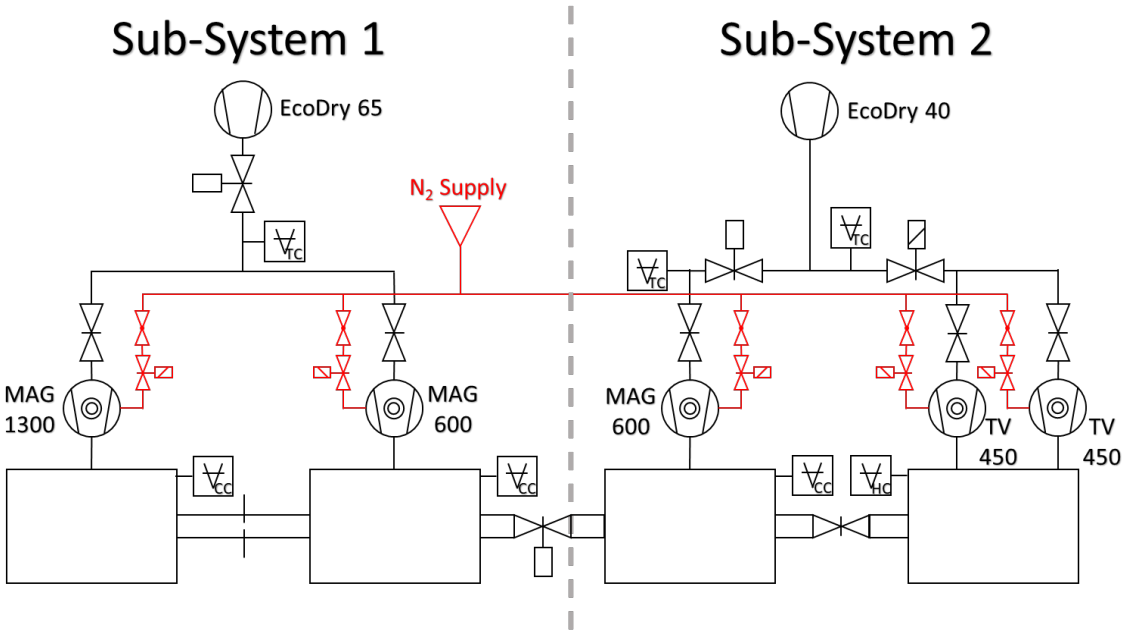

Figure 2.3: Schematic of vacuum system.

TMPs are labeled by model number, starting with MAG or TV. Valves with attached boxes are controlled by the PLC system. Vacuum gauge labels are as follows: TC - Thermocouple Gauge, CC - Cold Cathode Ionization Gauge, and HC - Hot Cathode Ionization Gauge.

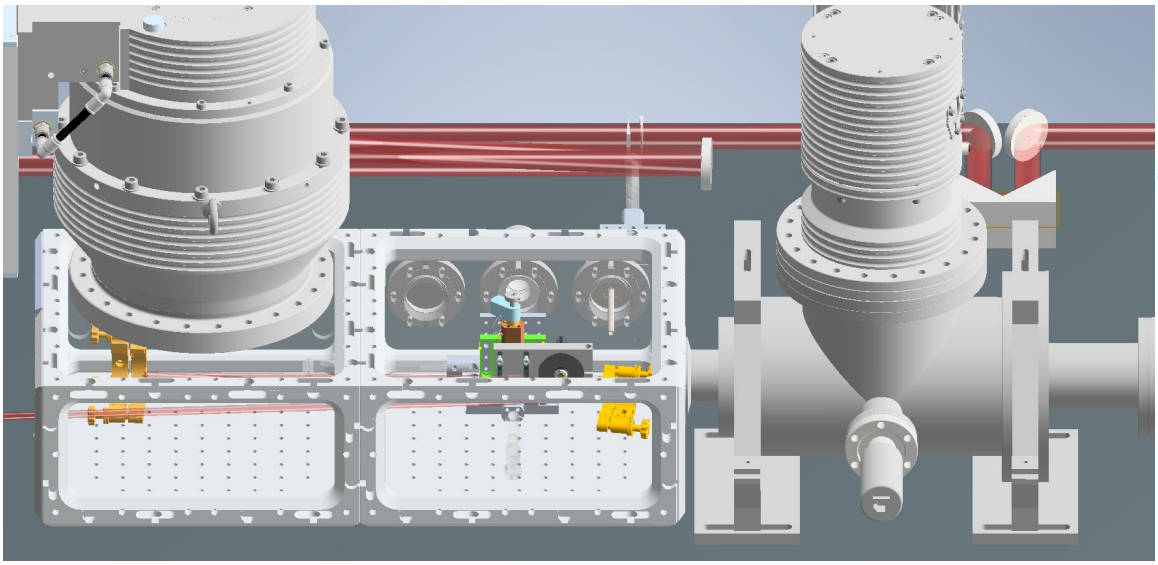

Figure 2.4: Sub-System 1

CAD drawing of the generation and differential pumping vacuum chambers, which constitute sub-system 1. A vacuum aperture separates the two chambers allowing for a 2-3 order of magnitude reduction in pressure across the aperture. A CaF window allows the NIR light to be transmitted into the vacuum system.

2.3.1 Sub-system 1

Sub-system 1 is backed by a Leybold EcoDry 65 Plus 120V with a pumping speed of 32 cfm and a KF 40 inlet flange [71], and encompasses the Generation chamber and Differential Pumping chamber. A combination of 1.5" inner diameter flexible PVC tubing and 8" rigid PVC pipe connects the inlet of the EcoDry 65 to the larger vacuum system below the trapeze shelf. A pneumatically actuated bellows sealed KF 40 gate valve connects the EcoDry 65 to the outlet flanges of two TMPs [29]. A Lesker model KJLC615TC thermocouple gauge, with a measurement range of 1-2000 mTorr, is used to monitor the pressure in the roughing gas lines [19]. Each TMP has a KF 40 manually actuated gate valve to provide redundancy in sealing the chambers from the roughing line in addition to a means of constraining the initial flow of air into the EcoDry 65 when initiating a pump down.

Generation Chamber

A Leybold Turbovac MAG W 1300 iP, with a pumping speed of 1100 L/s, is mounted on a 10" CF Flange to a pair of connected modular aluminum vacuum chambers from Ideal Vacuum [74, 103]. This chamber contains an Amsterdam Piezo Valve, a piezo actuated gas valve capable of sustaining 10 bar backing pressures with an opening diameter of 500 μm, variable pulse duration as low as 20 μs, and stable operation at repetition rates from 0 (constantly open) to 5 kHz [12, 51]. More information on the performance of this valve can be found in Appendix B. This TMP was selected to accommodate the large throughput of gas the piezo valve is capable of delivering (on the order of a $\frac{mbar*liter}{sec}$ in typical operation). Generation chamber pressure during typical operation is on the order of a few mTorr. A Penningvac PTR 90 N vacuum gauge from Leybold is attached to monitor the chamber pressure from 7.5×10^{-9} Torr to 750 Torr [72]. To mitigate absorption of the XUV light in propagating from the Generation chamber to the detector, it is desirable to reduce the pressure by several orders of magnitude from the mTorr level. Normally a glass window can be used to separate vacuum chambers while transmitting optical radiation, but the strong absorption of the XUV light requires instead the use of a vacuum aperture. A custom designed plate is fixed in the Generation chamber to mount different vacuum apertures of sizes ranging from 10 mm to 1 cm.

Differential Pumping Chamber

After the vacuum aperture, the Differential Pump chamber, a 8" CF tee from Lesker, is connected to the Generation chamber by an adapter flange to fit the KF 50 connection on the Ideal Vacuum cube chambers. It is terminated by a CF 8" to CF 4.5" adapter flange. This chamber was modified to have a CF 2.75" connection for mounting a Penningvac PTR 90 N for monitoring chamber pressure. A Leybold Turbovac MAG W 600 iP is mounted to the Differential Pumping Chamber. During typical operation, the pressure in the chamber is on the order of 10^{-6} Torr. With no gas injected in the system, vacuum pressure below the measurement range of the Penningvac gauge is common, $< 7.5 \times 10^{-9}$ Torr.

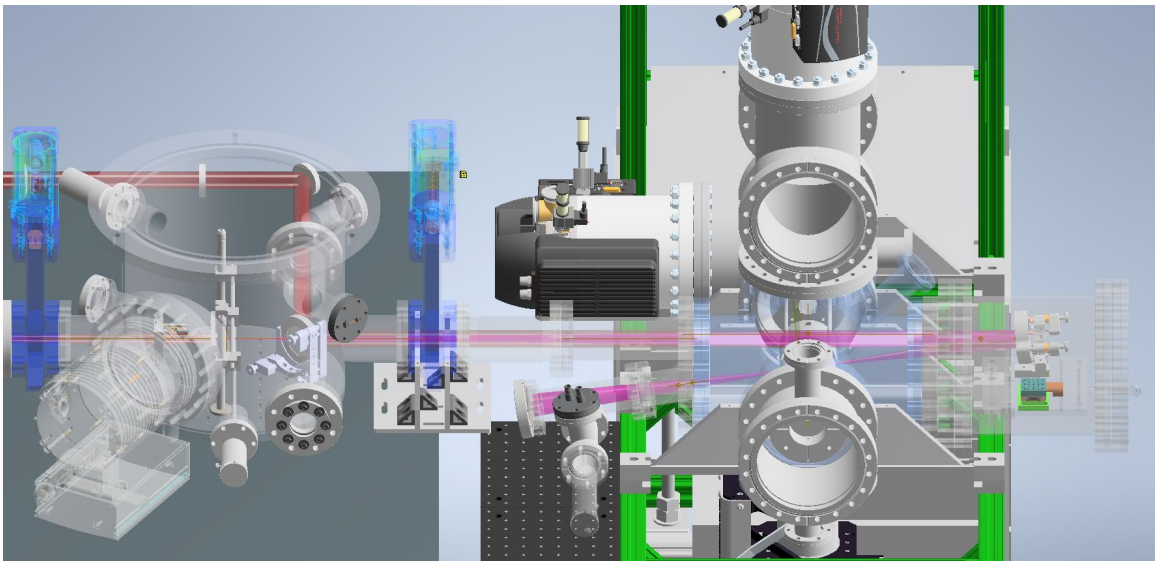

Figure 2.5: Sub-System 2

CAD drawing of the recombination and detector chambers, which constitute sub-system 2. The NIR and XUV beams are recombined on a 4 mm diameter hole mirror in the recombination chamber, and focused by the XUV Mirror in the detector chamber. A total of 860 L/s of pumping speed in the detector chamber, combined with regular baking, minimize the amount of contaminant species than can affect SFS experiments.

2.3.2 Sub-System 2

Sub-system 2 is backed by a Leybold EcoDry 40 Plus 120V with a pumping speed of 24 cfm and a KF 25 inlet flange [70], and encompasses the Recombination chamber and Detector chamber. A combination of 1.5" inner diameter flexible PVC tubing and 3" rigid PVC pipe connects the inlet of the EcoDry 40 to the larger vacuum system below the trapeze shelf where it is split by a KF 40 tee. Both chambers have hardware similar to that in Sub-system 1 to provide redundant closure of the chambers from the roughing lines and gauges to monitor rough vacuum pressure. Behind the TMP for the Recombination chamber is a KF 40 manual gate valve, a KF 25 pneumatic valve [28], and a KJLC615TC thermocouple gauge. Behind the two TMPs for the Detector chamber are KF 25 manual gate valves, a KF 25 solenoid gate valve, and a thermocouple gauge.

Recombination Chamber

The Recombination chamber is a custom cylindrical chamber with an O-ring sealed lid manufactured by Lesker. A Leybold Turbovac MAG W 600 iP, with a pumping speed of 550 L/s. is mounted to the chamber by a CF 8" flange, and chamber pressure is monitored by Penningvac PTR 90 N vacuum gauge. A CF 4.5" pneumatic gate valve (VAT 10836-UE44) connects the chamber to the adapter flange at the end of the Differential Pumping chamber [1]. A CF 4.5" manual gate valve connects the Recombination chamber to the Detector chamber downstream. During typical operation the pressure in the chamber is on the order of 10^{-6} Torr, which at this point is largely from the gas injected into the Detector as opposed to the Generation chamber. With both gate valves closed, vacuum pressure below the measurement range of the Penningvac gauge is common, $< 7.5 \times 10^{-9}$ Torr.

Detector Chamber

This chamber was largely inherited from previous experiments, and has distinct requirements from the rest of the vacuum system. As a result, much of the hardware is unique relative to the rest of the SFS. A pair of Leybold Turbovac 450i, hybrid bearing TMPs, with a pumping speed of 430 L/s, are mounted on CF 8" flanges, one directly above the interaction region, and the other near the multi-channel plate assembly for the ion time of flight spectrometer [73]. These pumps were selected for the reduced mechanical vibrations from the hybrid bearing, UHV side magnetically levitated and ceramic bearing on the outlet end, combined with the cost savings from avoiding fully magnetically levitated TMPs. Above the interaction region is a 8" CF cross where a TMP, vacuum gauge, and titanium sublimation pump are mounted. The nude hot filament ion gauge, Lesker model G1840, is used to monitor the UHV base chamber pressures down to 1.0×10^{-12} Torr. The titanium sublimation pump consists of a titanium filament which will emit an atomically thin layer of highly reactive atomic Ti when driven by a large current from an attached power supply. The atomic Ti will then bind to contaminant gases in the chamber, such as hydrogen which can permeate through the stainless steel walls of the chamber, allowing for further reduction

of the background chamber pressure. A long capillary gas nozzle with 127 μm opening is used to inject the target gas into the detector. Outside the chamber, a liquid nitrogen trap is used to freeze out contaminant gases in the delivery lines to the capillary nozzle. Typical chamber pressures in the detector chamber vary with the experiment conducted, but are of order 10^{-5} - 10^{-4} Torr.

2.3.3 Process Controls and Electronics

To provide an automated means of pulling vacuum and venting the system, a Programmable Logic Controller (PLC) has been implemented to manage both of these processes. This provides the added benefit of encoding digital safety interlocks and procedures for handling unexpected vacuum leaks and error signals from TMPs. As compared to common micro controllers such as an Arduino or Raspberry Pi, a PLC is more ruggedly constructed, conforms to process engineering standards for reliability, and can directly open/close circuits at 12 to 24 VDC which are commonly used for vacuum hardware. A PLC is programmed using ladder logic to execute actions on the outputs based on the state of the inputs. At a rate of thousands of times per second, it scans the rungs of the logic ladder executing each rung sequentially. A Click PLC from Automation Direct, model C0-10DRE-D, was chosen for its fully featured hardware and software at low cost, several expansion modules were also incorporated to increase the number of inputs and outputs [26]. This PLC was paired with a C-more Micro touch panel also from Automation Direct to provide a simple user interface to initiate system processes and check the status of various components [24]. A 24 V power supply powers this system, in addition to the various electronically controlled valves, and a battery control module with a pair of 12 V lead-alkali batteries in series provides a redundant source of power in the event of temporary power failure in the building.

Figure 2.6 provides a schematic of the various circuits connected to the PLC. All inputs and outputs are treated as binary values (open or closed). Inputs provide the PLC with information on the current state of the apparatus including error signals from the 5 TMPs (Tx-E) and pressure set points from the vacuum gauge controllers for each individual chamber (like GEN-H or CM-L). Outputs include the on/off signal for the TMPs (Tx),

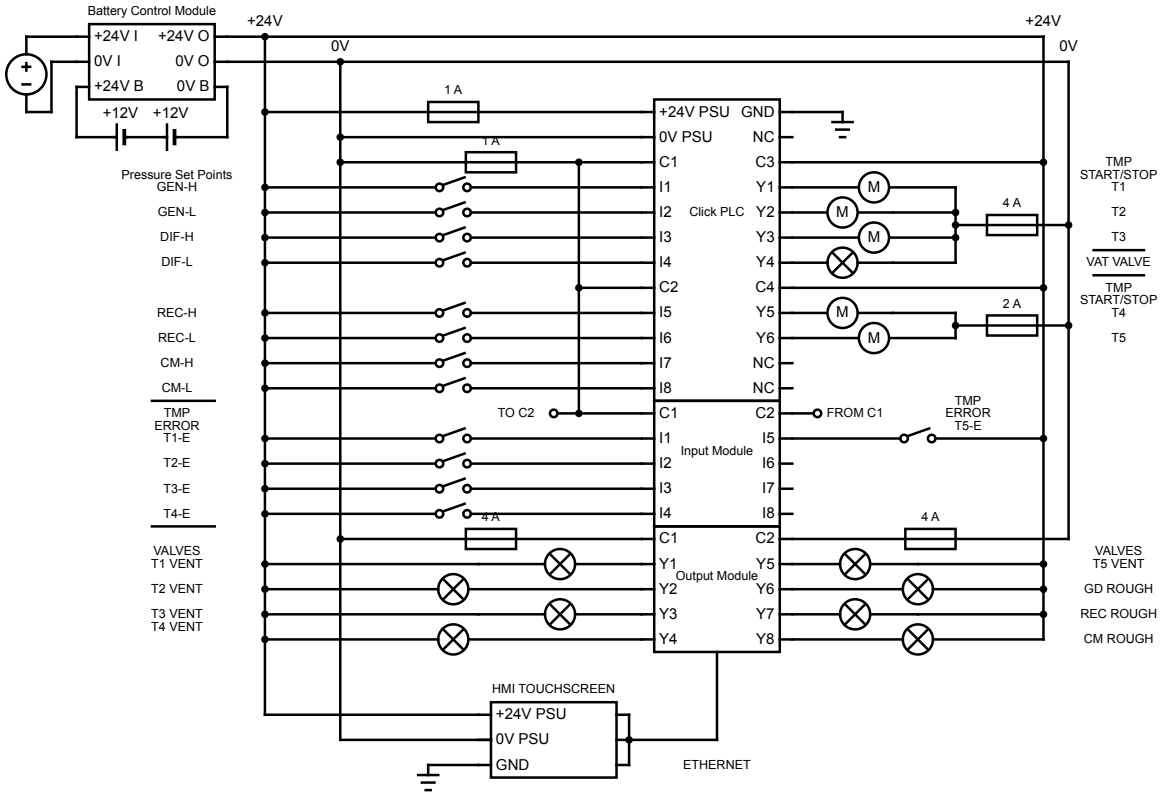

Figure 2.6: Schematic of controls wiring.

Connections to the PLC are prefixed with C - Common, I - Input, and Y- Output. Chambers are labeled by G or GEN - Generation, DIF or D - Differential Pumping, REC - Recombination, and CM - Detector. TMPs are labeled as T1 - Generation TMP (MAG 1300), T2 - Differential Pumping TMP (MAG 600), T3 - Recombination TMP (MAG 600), T4 & T5 - Detector TMPs (Turbovac 450). Crossed circles represent valves, and circles with M represent TMPs.

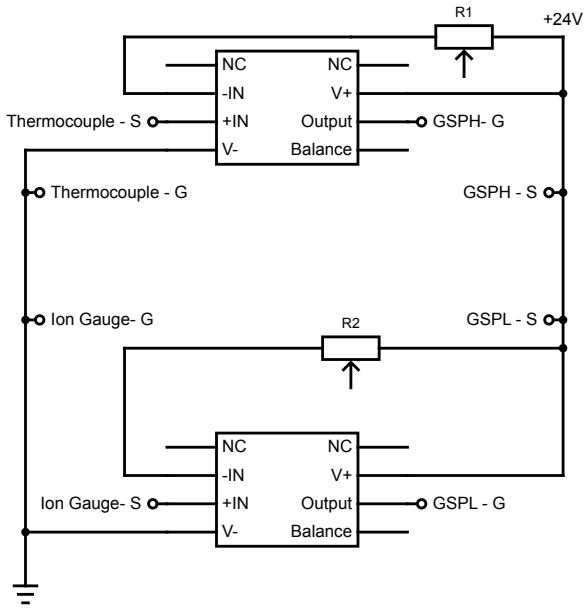

Figure 2.7: Schematic of set point circuits for detector chamber pressure.

the venting valves for each TMP (Tx Vent), the gate valve between the Differential and Recombination chambers (VAT Valve), and the gate valves for the roughing lines (REC Rough). Fuses are also marked with their appropriate Amperage rating. As the Granville-Phillips Series 307 controller for the vacuum gauges on the detector chamber (labeled CM for coincidence machine in Figure 2.6) does not provide binary output pressure set points, an additional circuit was assembled to convert the analog signal to a digital value using op-amps and varistors to create tunable comparator circuits, as can be seen from Figure 2.7 [45]. The Penningvac PTR 90 N gauges on the Generation, Differential Pumping, and Recombination chambers supply their pressure set points through their controller, a Leybold DISPLAY THREE model number 230025 [69]. For details on how to operate the PLC system to initiate vacuum processes see Appendix A.

2.3.4 Vacuum Bake-Out System

In order to achieve chamber pressures in the UHV regime, it is critical to reduce gases, water vapor, and other contaminants inside the chamber, and a vacuum bake-out is a process to remove such contaminants. Applying surface heat, up to a maximum of 80°C

for the detector chamber, for several days can significantly increase the desorption rate of molecules, especially water vapor, that adhere to the surface of the stainless steel chamber, as well as the diffusion process of other impurities.

As the SFS experiments are so sensitive to contaminant species, a vacuum bake-out system was implemented to automate the bake-out process for the detector chamber. Three lengths of heat tape, which are resistive wires sheaved in insulating fiber glass, are coiled around the exterior of the detector chamber and covered with several layers of aluminum foil on the outside. The aluminum foil helps to distribute the heat from the tape to the entirety of the detector chamber. Each length of heat tape is connected to an AutomationDirect SOLO temperature controller (SL4848 series) module with a built-in thermocouple to monitor and control the applied current through the heat tape [25].

In the span of a few days, a ramp/soak cycle is carried out using the temperature controller. This process involves discrete stepping of the chamber temperature, with each step followed by a soaking period where the temperature is held constant to allow for even distribution of the heat throughout the system. For these experiments, each step increased the chamber temperature by 20°C over 20 minutes followed by 20 minutes of soaking until the desired temperature of 80°C was reached. This final temperature would be held for 22 hours, before the ramp/soak cycle would return the chamber to room temperature via the same step and pause approach. For extended bake-outs this entire process was looped, repeating every 24 hours. The reasoning behind this slow ramp process is dictated by concern for the vacuum windows attached to the chamber. The differing coefficients of thermal expansion between glass and stainless steel are such that windows can easily shatter if the temperature of the chambers changes rapidly. Recommended upper bounds for rates of temperature change are about 2°C per minute. A successful bake-out should leave the detector chamber well below the 10^{-9} Torr level.

2.3.5 Peripheral Systems

Proper operation of the TMPs and vacuum valves relies on two other systems worth mentioning here. First is the distribution of chilled water for cooling the TMPs. The building

supplies chilled water at a pressure of about 40 psig in the DiMauro lab, and a single line of 1" braided PVC tubing connects the SFS to this supply. This line is attached to a manifold of hand valves, one for each TMP, each of which need to be open whenever operating their corresponding TMP. A pressure gauge attached to the manifold provides an indication of proper flow. The return lines from each TMP attach to another manifold, which is connected to the house supply return line. When the TMPs are not in operation, it is good practice to close these valves to prevent any water vapor in the vacuum system from condensing in the TMPs.

In addition to chilled water, the building has a supply of dry nitrogen from the boil off of the liquid nitrogen system. This source is of high purity, and is readily available at pressures of about 100 psig. Above the SFS, a pair of regulators are used to reduce the house pressure, one is set to a few psig, and the other to 75 psig. The low pressure regulator is connected to the vent valves for each TMP, so that a dry and clean gas can be used to bring the chambers up to atmospheric pressures. With a pressure slightly above atmosphere the chambers can be operated as nitrogen purge boxes when the vacuum pumps cannot be run, as the generation and recombination chambers are equipped with pressure relief valves which will leak at internal pressures above 2 psig. The high pressure regulator supports the pneumatic gate valve attached to the roughing lines and the VAT valve separating the Differential Pumping and Recombination chambers. Each device, from either the high or low pressure regulator, is in series with a compression fitted ball valve allowing for each component to be isolated from the rest when needed.

2.4 Optical System

The SFS presents several technical challenges that required careful consideration when designing the optical system. The primary concerns are:

1. Producing sufficient XUV fluence with the correct spectral shaping.
2. Generating ponderomotive energies on of ~20 eV.
3. Interfering the XUV and NIR light with attosecond resolution.

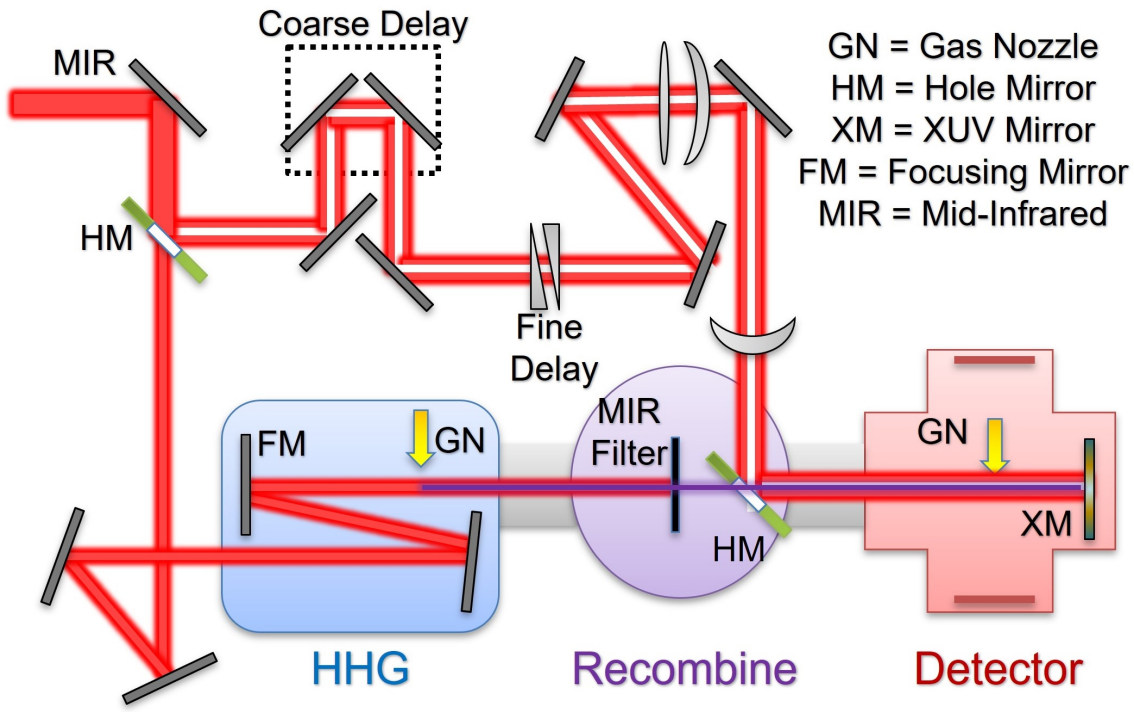

Figure 2.8: The SFS Interferometer

A schematic of the SFS Interferometer. A pair of hole mirror are used to split and recombine the HHG and Dresssing arms. The relative delay between the two arms is controlled by a retroreflector and silica wedge pair. A three-lens system provides precise control over the NIR beam size and divergence for optimal focusing in the detector chamber. An achromatic design for focusing in HHG allows for two-color HHG. A thin metallic foil separates the XUV from residual NIR light. Both arms are focused by the dual region XUV mirror, where the waists are focused to a point below the optical plane, or into the page.

Unfortunately, goals (1) and (2) often work in opposition to each other and the only means of improving both simultaneously is simply increasing the pulse energy of the infrared laser. These competing goals have been one of the leading technical difficulties of making SFS measurements in the past. The light source described in Section 2.2 is sufficient for conducting these experiments. Other strategies included minimizing transmission losses, using a shorter focusing geometry for the NIR, using longer wavelength NIR lasers, and precise beam shaping of the NIR light to maximize its intensity at focus.

Goal (3) drives the decision to use a single laser source to both generate the XUV and drive the strong field interactions of interest. The SFS requires control over the relative

phase between the XUV and NIR with sub-cycle resolution with respect to the NIR field. As HHG is a coherent process, the use of a single laser source in an interferometer ensures there is a well defined phase relationship between the two fields. However, this coherence is necessary but insufficient to conduct an SFS experiment. Instabilities in the interferometer path lengths on the order of the NIR wavelegnth, ~1.7 μm, will destroy an sub-cycle resolution for these experiments. Sources of these instabilities include mechanical vibrations from a TMP or the external environment, changing densities of air the light travels through, and drifts in the pointing of the laser into the interferometer because of the number of transmissive elements. To address these concerns the optical elements were kept low to the optical table, <6 in, and optics were mounted on 1" diameter stainless steel posts. Ideally, the large mass, ~909 kg, of the optical tables will minimize the amplitude of vibrations that could result in moving optics during experiments. The entire interferometer was enclosed, either in vacuum or by removable panels, to eliminate air currents. In addition, to minimize laser pointing drift, the laser system requires a minimum of two hours warm up each day prior to taking any measurements requiring attosecond stability. The Guidestar beam point system can correct any drifts after this initial warm up period.

2.4.1 Shared Optics

A unique challenge to building an interferometer operating at such dramatically different regions of the electromagnetic spectrum is the lack of effective dichroic optics. A Mach-Zehnder geometry featuring a pair of hole mirrors to split and combine the arms of the interferometer was selected to maintain the highest possible transmission efficiency of the XUV light. A 6 mm hole mirror, on a 2" substrate, splits the light, and a 4 mm hole mirror is used to recombine the two arms. The size of the splitting mirror determines the distribution of laser pulse energy into each arm. For the size of the NIR beam, the 6 mm hole sent 60%, 1.2 mJ, of the pulse energy into the dressing arm and the remaining 40%, 0.8 mJ, into the HHG arm. The size of the recombining hole mirror faces two competing constraints, maximizing transmission of the XUV through the hole (increasing diameter) and maximizing reflection of the NIR light around the hole (decreasing diameter). With

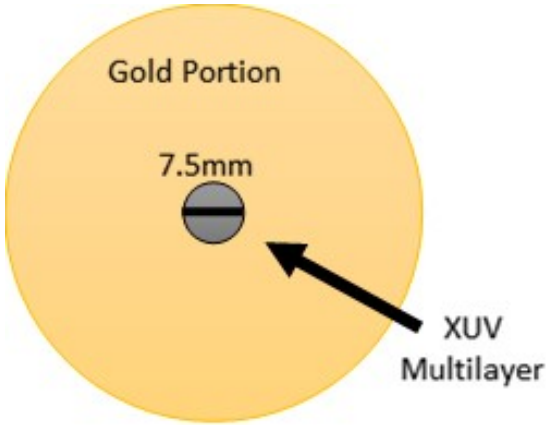

Figure 2.9: The XUV Mirror

Two concentric regions on a 2" substrate are coated for efficient reflection of the XUV and NIR light. The inner 15 mm diameter region is a multilayer SiC/Mg coating optimized for photon energies at the Ip energy of helium. The outer annular region is gold coated to efficiently reflect light across the NIR spectrum.

the relative ease of reshaping the beam size of the NIR, compared to the XUV, the first constraint was favored. The 4mm hole mirror was the smallest readily available for these experiments that did not impact the transmission of the XUV light.

The final optic shared by both arms of the interferometer is a concave spherical mirror with a Radius of Curvature (ROC) of 500 mm. To maximize the reflective efficiency for both XUV and NIR light, the mirror was designed to have two distinct regions on its 2" substrate, see Figure 2.9. The beam is initially transported above the interaction region and then reflected downward at 10°.

2.4.2 HHG Arm

Following transmission through the 6 mm hole mirror the NIR beam is reflected by a pair of mirrors and sent into the vacuum system through a 2" CaF window with an anti-reflective coating for 1.7 μm light. This provides >99% transmission efficiency for the NIR light in this experiment. In vacuum a concave spherical mirror with a ROC of 750 mm is used to focus the light into the gas jet where HHG occurs. The gas source is on a three-axis translation stage in order to optimize the relative positions of the NIR focus and the gas

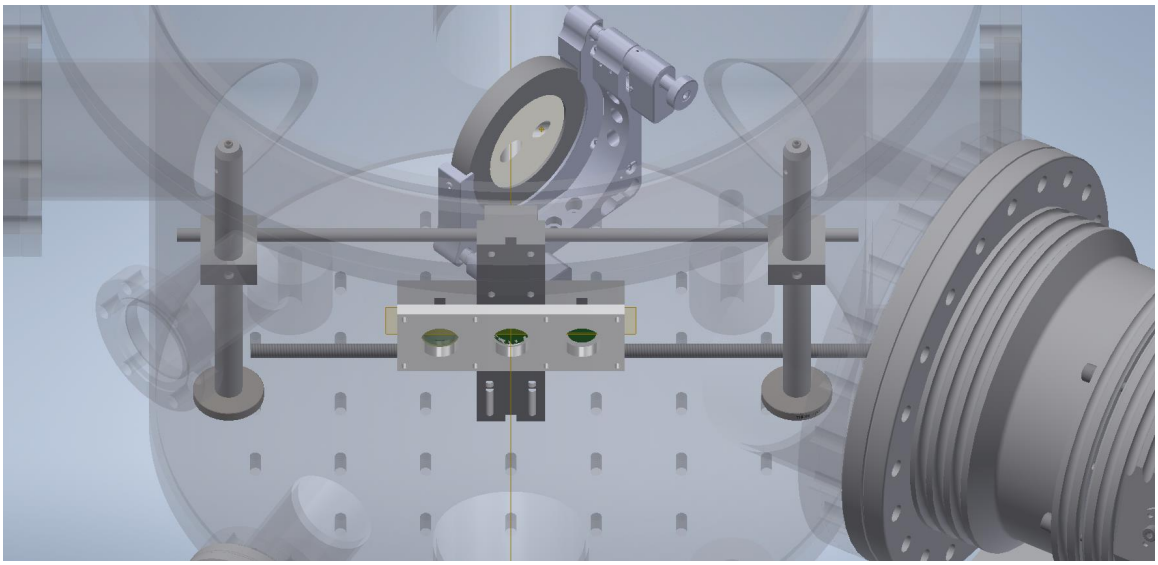

Figure 2.10: Filter Mount and Hole Mirror

CAD drawing of the recombination chamber where the thin metallic foil, for removing residual NIR light after HHG, is mounted on a rail. A lead screw driven by a knob outside of vacuum allows for exact positioning of the filter assembly. The hole mirror is mounted on a motorized optical mount for tip and tilt adjustments in vacuum, this was used for day to day adjustments of NIR pointing independent of the XUV beam.

jet. For many of the experiments discussed in this thesis, additional elements were added outside of vacuum to produce a two-color field for HHG. For more information on these additions and the HHG process itself see Chapter 3.

Following the HHG region the beam passes through a 5 mm vacuum aperture and the differential pumping chamber into the recombination chamber. It next impinges on a thin metallic foil to separate the XUV from residual NIR light. All the experiments in this dissertation utilized an aluminum foil of 100 nm thickness deposited on a supporting nickel mesh. Finally, XUV beam transmits through the second hole mirror from which it propagates collinearly with NIR light to the XUV Mirror in the detector chamber. Both the Al foil and XUV mirror transmit/reflect a finite bandpass in the XUV region which is key to the SFS design, see Chapter 3 for more details.

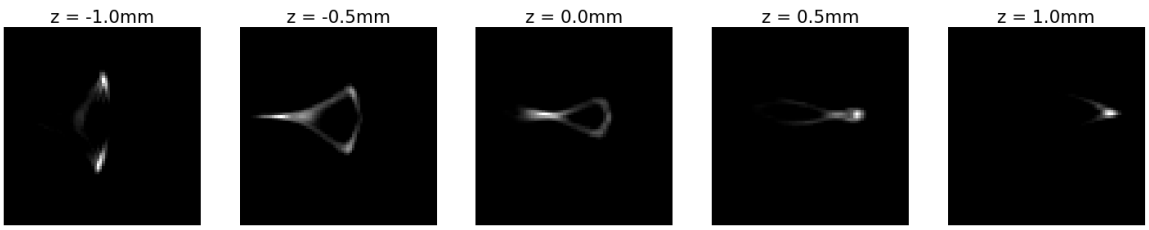

Figure 2.11: Astigmatism of Dressing Arm

Beam profile versus propagation distance as measured on a test stand using a concave spherical mirror with ROC of 400 mm. Each image is labeled with its displacement from the imaging distance approximately centered between the vertical and horizontal waists. Each image is 160x160 pixels.

2.4.3 Dressing Arm

The dressing arm begins with a reflection off the 6 mm diameter hole mirror used to split the NIR light, creating a donut shaped mode in the dressing beam. Following the hole mirror, a retroflector on a 1" translation stage provides coarse means for matching the path lengths of the interferometer. Typically this can be adjusted by hand to a resolution of order 10 μm by focusing both arms of the interferometer downstream into a BBO crystal and looking for second harmonic generation between the two beams. Fused silica wedges, with a wedge angle of 4°, paired with a Thorlabs model Z825b stepper motor provides fine control over the delay. Considering this motor's step resolution of 29 nm, and the index of refraction of silica (n = 1.44 for 1.7 μm light [79]), this provides a minimal step size of 3.11 as which far exceeds the requirements of these SFS experiments. On a daily basis the wedge insertion distance needed to be adjusted to find the optimal temporal overlap of the XUV and NIR light. Further information for identifying optimal overlap is provided in Section 2.4.4.

Key to achieving the maximum possible intensity of the NIR in the interaction region was the selection of focusing elements in the dressing arm. Various 2- and 3-element combinations were initially tested with the intent to minimize the F-number on the gold portion of the XUV Mirror, ideally maximizing the focused intensity. It was quickly discovered that the astigmatism from the off-axis reflection, 5° with respect to the surface normal at

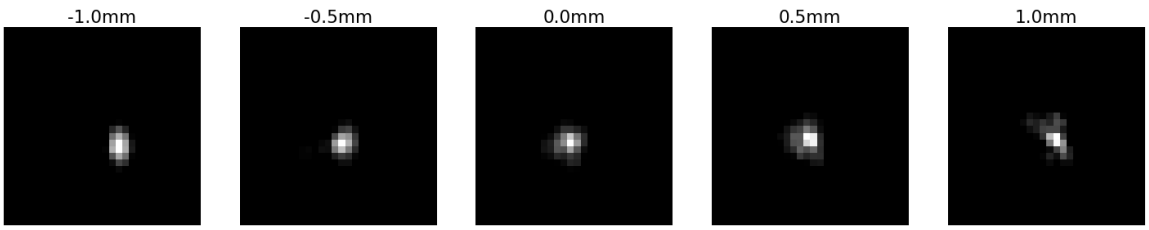

Figure 2.12: Corrected Astigmatism of Dressing Arm

Beam profile versus propagation distance as measured on a test stand using a concave spherical mirror with ROC of 400 mm. Each image is labeled with its displacement from the imaging distance approximately centered between the vertical and horizontal waists. Each image is 50x50 pixels.

center, of the spherical mirror prevented the donut shaped NIR beam from cleanly focusing. To better understand the severity of the astigmatism and identify solutions, a test stand was assembled out of vacuum to simulate the focusing geometry of the XUV Mirror in the detector chamber. At the time, a 3-element lens system in the dressing arm was tested consisting of a telescope with 2x demagnification and a -500 mm focal length lens placed ∼1.3 m before the XUV Mirror. Available at the time for the test stand was a concave spherical mirror with ROC of 400 m. The images in Figure 2.11 illustrate the astigmatic spatial profile of the focused beam. One trivial means of fixing this astigmatism was compensating for it with a rotation of the converging lens in the telescope. The optimal beam profile after correcting the astigmatism in this way is shown in Figure 2.12, demonstrating a gaussian like focus of this donut shaped beam.

Unfortunately, this method of compensating for the astigmatism led to its own problems on reflection off the second hole mirror. The amount of astigmatism introduced by rotation of the lens created a cigar shaped beam profile and caused a significant amount of light to be transmitted through the hole as opposed to being reflected around it. It was decided that the best means of reducing astigmatism was to increase the F-number on the XUV Mirror as much as possible, contrary to the original intent. Similar improvements in mode quality as in Figure 2.12 were achieved by simply increasing the F-number on the concave mirror. One concern was the NIR reflecting partially off both regions of the XUV Mirror as the donut shaped mode was reduced in size. The relative flatness between the two regions

and was unknown and it was possible that the NIR light reflected off one region would have a dramatically different phase than the other upon reaching the beam waist. Therefore, the beam was confined to the inner multilayer coated portion of the XUV Mirror. This portion of the mirror was measured to have an 80% reflection efficiency for light at 1.7 μm. The reflection off the second hole mirror again limited the effectiveness of this approach, imposing a minimum size for the donut mode while ∼1m away from the XUV Mirror. The final combination of focusing elements were a lens pair in a telescope geometry with focal lengths +125 mm and -75 mm for a 1.67x demagnification. Approximately 0.5 m after the telescope, 0.1 m prior to the second hole mirror and 1.1 m to the XUV Mirror, a -1000 mm focal length lens matches the divergence of the NIR beam to the XUV. All three elements are made of CaF and have anti-reflective coatings for 1.7 μm light. Another CaF window similar to that in the HHG arm, is used to transmit the NIR light into the vacuum portion of the dressing arm.

2.4.4 Finding Spatial-Temporal Overlap

The SFS experiment proved to be incredibly sensitive to both the spatial and temporal overlap of the XUV and NIR beams. Achieving sub-cycle resolution in this experiment requires that the XUV beam samples a small distribution of NIR phase. In the time domain, this suggests the XUV pulse duration should be as short as possible and the path lengths of the interferometer are stable. In the spatial dimensions, the waists of the two beams need to be overlapped, both in the transverse plane and along the propagation direction, and their pointing needs to be stable. The stability of the pointing and path lengths have already been addressed, but identifying the point of optimal spatial-temporal overlap is challenging. Coarse spatial-temporal overlap can be found by sending the NIR beam through both arms of the interferometer, removing the metallic foil after HHG, and looking for interference fringes in a nonlinear interaction between the fields. At 1.7 μm, a distinct yellow color was observed when the light from both arms were focused into a Beta Barium Borate (BBO) crystal, this light is likely third-harmonic generation. However, the sensitivity of SFS experiments far exceeds the resolution achieved by this coarse procedure.

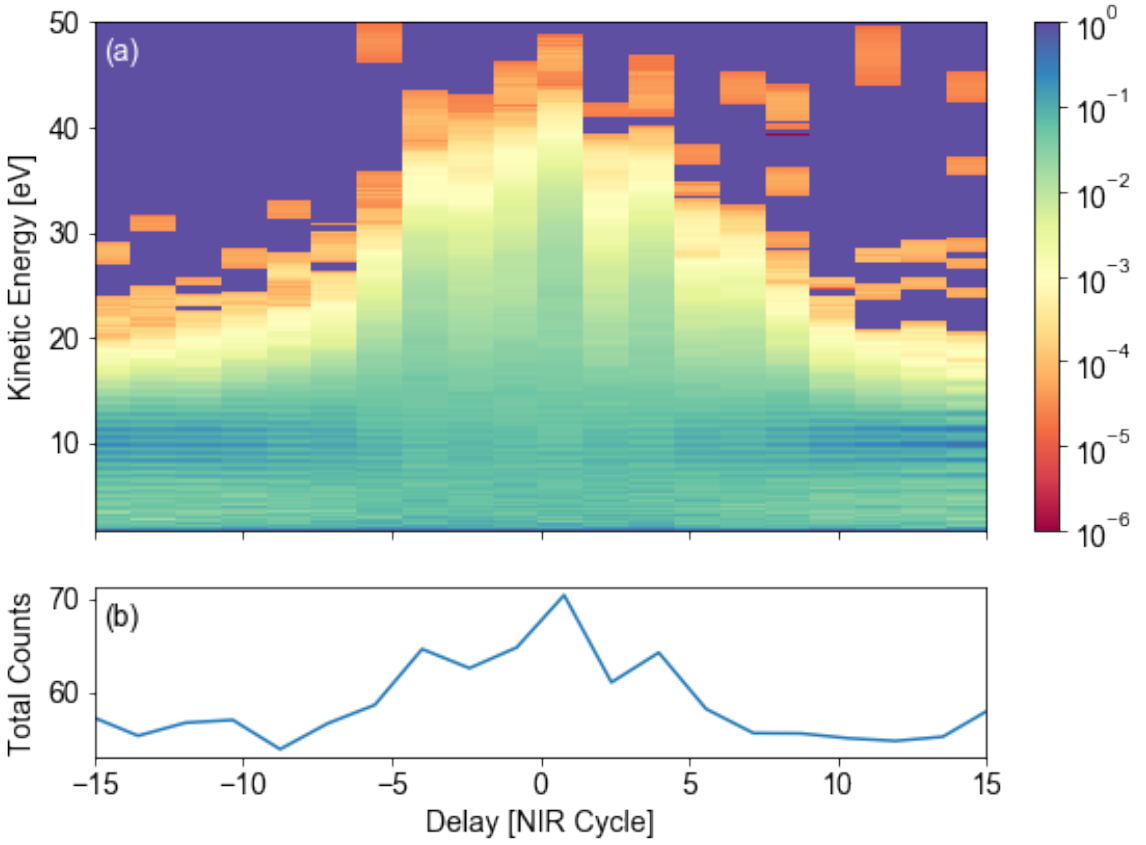

Figure 2.13: Spectrogram of a Coarse Delay Scan

(a) Photoelectron spectrum versus XUV and NIR relative delay, step size ∼1.6 NIR Cycles. Target species is argon, NIR wavelength is 1.7 μm, NIR intesnsity is ∼15 TW/cm^2, and XUV is an odd-order only comb. The NIR field has a FWHM of approximately 10 cycles. (b) The total count rate versus relative delay. The 0 delay for (a) and (b) is set by the centroid of the gaussian like distribution. The sawtooth structure near in (b) near delay 0 is aliasing and reflects the sub-cycle sensitivity of the experiment, as each delay step in this scan is a non-integer multiple of the NIR field.

More accurate spatial-temporal overlap was found by observing the photoelectron distribution when the XUV and NIR are mixed in a lower Ip target such as argon. In a sense, just attempting a crude SFS measurement. Key features in the photoelectron distribution are sensitive to the peak NIR intensity, see Chapter 4 for more details. The +125 mm lens in the NIR telescope, recombination hole mirror tip & tilt, and delay wedge insertion could all be precisely adjusted to independently control the NIR waist in the three spatial plus temporal dimensions. All of these parameters were optimized by maximizing the total photoelectron yield and highest observed kinetic energy, note these both scaled linearly in NIR intensity. The total optimization procedure begins with (1) a cross-correlation style scan as shown in Figure 2.13, from which the optimal delay of the NIR beam could be determined to within a few laser cycles. (2) finer delay steps are taken to find the sub-cycle delay yielding the greatest photoelectron counts and kinetic energies. (3) a single spatial dimension, say the pointing of the NIR beam through the tip of the recombination hole mirror, is adjusted to a new position. This will change the path length of the interferometer significantly on the order of an NIR wavelength, so (4) the new optimal delay is found by taking sub-cycle delay steps (if the adjustment was large enough repeating step (1) may be necessary). (5) the photoelectron yield yield at this new position and delay is compared to the result from (2), and the spectra with larger yield and kinetic energies is selected to be the superior position. (6) repeat steps (3) through (5) until the given spatial parameter is optimized. (7) begin this process again at step (2) for each additional spatial parameter. Unless substantial adjustments to the interferometer are made, the relative positions of the beam waists are stable day to day and the above procedure is only needed to optimize the pointing of the NIR beam. This typically takes 20 - 30 minutes to complete.

2.5 Detectors

The detectors of the SFS apparatus are a pair of Time-of-Flight (TOF) systems for measuring photoelectron kinetic energies and mass-to-charge ratios of ionic species. These detectors are collinear and the total system is capable of making coincidence measurements, though

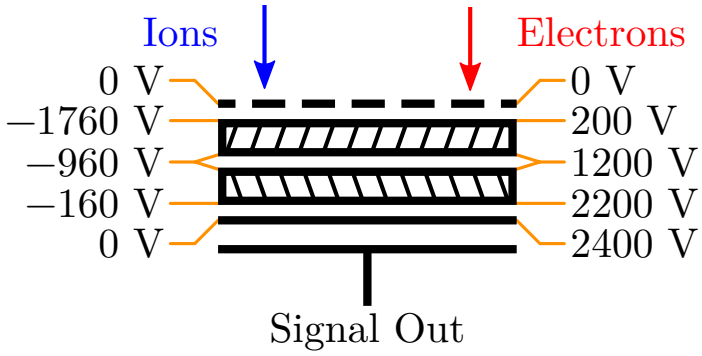

Figure 2.14: Schematic of the MCP Detectors

Each detector assembly consists of an initial field plate terminating the TOF region, a pair of MCPs in the chevron configuration, a collection plate, and a capacitively coupled anode from which the signal is read out. Adapted from [59].

none were made for these experiments due to limited counting rates for many of the signals of interest. The target gas is introduced by a capillary with an inner diameter of 127 μm, and is mounted on a three axis-translation stage to control its position relative to the laser beam waists. This portion of the apparatus was inherited from previous experiments in the DiMauro lab, though for these experiments the Microchannel Plate (MCP)s were replaced.

2.5.1 Microchannel Plate Detectors

A MCP functions similarly to an array of photomultiplier tubes tightly bundled together. Each MCP is a thin glass plate composed of micron sized channels set a small bias angle with respect to the surface normal, typically about 10°. A large bias voltage of order 1 kV across the faces of the MCP will accelerate electrons through the channels. With these conditions, a charged particle flying with sufficient kinetic energy can impact the wall of an MCP channel and drive multiple ionization events. Each of these newly released electrons are accelerated by the bias voltage such that when they impact the walls of the channel they each create their own shower of electrons. These cascading multi-ionization events, or electron avalanche, allow for exponential gain, taking a single charged particle as input and returning a measurable pulse of current. These MCPs can be chained together in series in order to achieve higher gains. Both detectors described below utilize a pair of MCPs in

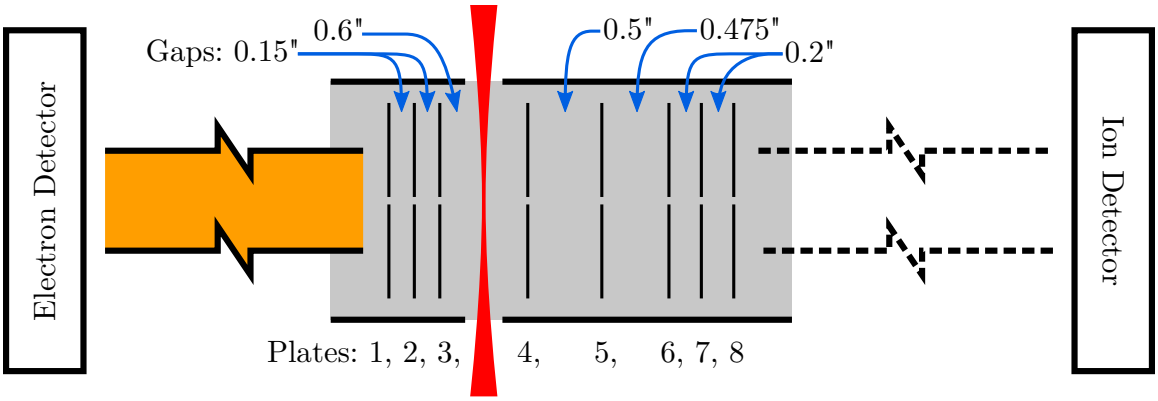

Figure 2.15: Schematic of the Coincidence Machine (Detector Chamber)

The interaction region is defined by the laser focus illustrated in red. Field plates are spaced as defined by the gaps between them. The eTOF region is protected from external fields by a gold-coated cylinder of Mu-metal. The TOFMS has a Faraday cage of metal mesh to screen external electric fields. The gas source protrudes out of the page, and a bias voltage can be applied to it independently of the field plates. Adapted from [59].

the chevron configuration, where the plates are stacked with their bias angles opposite each other such that the channels form a V-shape. See Figure 2.14.

2.5.2 Electron Time-of-Flight Spectrometer

The basic principle of an Electron Time of Flight (eTOF) spectrometer is to measure the flight time of electrons over a known distance to calculate their velocity along the detector axis, and by extension kinetic energy assuming small velocity components perpendicular to the detector axis are small. Longer flight regions provide greater energy resolution, where the 25cm of this eTOF spectrometer provides an energy resolution of $\Delta E/E$ 1% - 2% for kinetic energies of 25 - 75 eV. In the eTOF mode, field plates 1 - 8, see Figure 2.15, and the gas source are all set to 0 bias voltage, so the electrons propagate completely field free until the MCP assembly. With these conditions electron flight times were of order 100 ns and an observation window of 2 μs was used. The relatively light electron mass and low kinetic energies measured in the SFS experiments makes the eTOF sensitive to small external electric and magnetic fields, such as the Earth's magnetic field. To counteract these external perturbations, a cylinder of Mu-metal, a high magnetic permeability metallic alloy,

shields the TOF from magnetic fields and this cylinder is gold coated to act as a Faraday cage to screen external electric fields. For eTOF measurements, the output of the gas capillary was kept as close to the interaction region as possible to maximize the effective gas density, however too close and the NIR light would ionize the capillary and create a significant background signal.

2.5.3 Time-of-Flight Mass Spectrometer

The simplest Time-of-Flight Mass Spectrometry (TOFMS) consists of an acceleration region, a TOF region, and the detector. With a known velocity and TOF distance, the mass-to-charge ratio of different of the detected species can be calculated. This provides a distinct signal for most species to provide a definite assignment of atomic or molecular composition. For these SFS experiments, the acceleration region was defined by +500 V and +100 V biases applied to plates 3 and 4 respectively which surround the interaction region, with plates 1, 2, and 5 - 8 grounded. A bias voltage was set to the gas capillary to match voltage gradient between plates 3 and 4 at the position of the capillary. In these conditions ion flight times ranged from 2 to 14 μs and an observation window of 17 μs was used. On a daily basis, the capillary's bias was adjusted to optimize the ion yield for the atomic species of interest at a fixed NIR intensity. A Faraday cage consisted of a rolled metallic mesh protects the TOF region from external electric fields, with a 3 - 4 order of magnitude increase in mass as compared to electrons the ion TOF is relatively insensitive to external magnetic fields.

2.5.4 Data Acquisition

All electron spectra and ion mass spectra were collected by feeding the MCP signal output into a a 10-bit, 3 GHz, 8 GS/s, 1 V dynamic range digitizer, the Agilent/Keysight Acqiris U1065A DC252. The digitizer is triggered by a photodiode signal from each laser shot, so the output from each individual shot is separately stored in memory until read out via computer interface. The MCP for the electron detector contained a conical anode to impedance match the capacitively coupled source to the input impedance of the digitizer

at 60 Ohms. With a typical pulse height of ∼50 mV, the output of the electron detector required no amplification. The ion detector lacked the impedance matching of the conical anode, and significant ringing was observed when the output was directly connected to the digitizer. Therefore, the bias voltage across the MCP stack was reduced from the typical 2 kV to approximately 1.7 kV, see Figure 2.14, and the signal fed into an Ortec VT120 Fast Preamplifier, version C with 20x amplification. The net result was that the typical pulse height of ∼100 mV was maintained, but the fast preamplifier acted as an impedance matching device to reduce the ringing of the signal.

The control software, written by previous members of the DiMauro group, allowed the signal to be post-processed into an analog trace or digitized event binned by arrival time. In the analog mode, the signal collected for each trigger would be averaged to generate a voltage trace representative of the typical photoelectron distribution. In the digital mode, a Constant Fraction Discriminator set at 50% is used to assign an arrival time to each pulse, registering an event occurring within the corresponding time bin. The sum of many event creates a histogram of counts versus arrival time in the digital mode. Each mode has advantages and disadvantages, and the SFS experiments utilized both depending on the measurements made. The digital mode is useful for studying process with low count rates ($<$ 1 event/shot) such as the double ionization signals observed in helium and argon. Here this counting mode eliminates noise from the stochastic pulse amplitude distribution in determining the number of events occurring, see Figure 2.16. For electron signals where count rates frequently exceed 1 event/shot, the analog mode better captures the real photoelectron distribution as it can better distinguish when multiple events at the same arrival time occurred given sufficient averaging.

2.6 Analysis

Depending on whether the data collected is from the eTOF or TOFMS the pipeline for calibrating and analyzing the data are very different. In either case the basic principle is to take raw TOF, essentially an array of signal amplitude versus time, and convert the

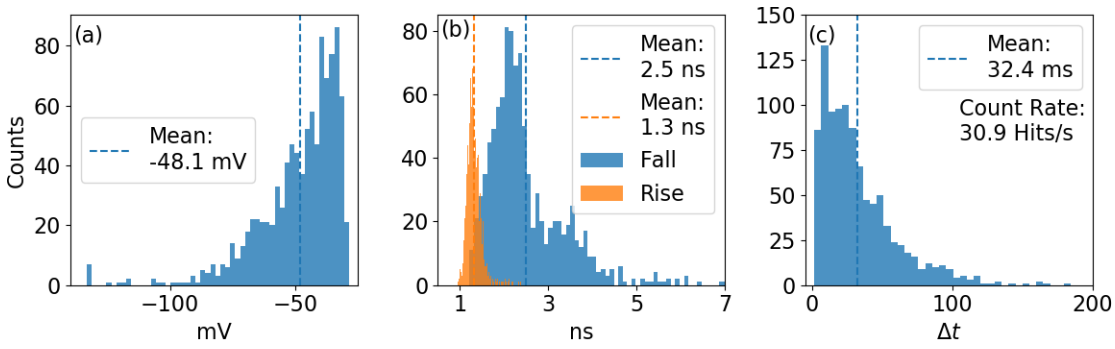

Figure 2.16: Characterization of the Electron MCP Detector

Histograms displaying the pulse characteristics of the electron MCP detector for 1000 events. These data were taken at a chamber pressure of 4.8×10^{-9} Torr at a trigger level of -20mV. These plots display (a) amplitude distribution in mV, (b) rise and fall times in ns, and (c) the time between events in ms. Inverting the mean in panel (c) provides an average count rate that when paired with the mean from (a) provide useful benchmarks for the health of the detector system. Adapted from [59].

flight time to the quantity of interest, either photoelectron kinetic energy or ion mass-to-charge ratio. There are several unknowns that effect the measured time delay between the event trigger and the arrival time of a charged particle such as the exact delay imparted by the signal transmission lines, the transmission time of the light between the triggering photodiode and the interaction region, and uncertainties in the exact voltages or geometry of the field plates in the TOF. As a result, any attempt at predicting the correct conversion formula from time delay to the measure of interest will lack the accuracy needed to effectively transform the data. Therefore, a calibration based on known features in the signal is the first step in analyzing TOF data.

2.6.1 Photoelectron Spectra

For all of the data reported in this thesis, the photoelectron spectra were calibrated using the emission from the XUV light in isolation. The harmonics are precisely spaced at a known interval, a multiple of the fundamental photon energy, providing numerous features to calibrate against. In addition, the narrow reflective bandwidth of the XUV Mirror centered at 26.2 eV provides an absolute reference for the photoelectron energies. The calibration

and conversion is done using a software package developed by Dietrich Kieswetter where the geometry and voltages of the eTOF field plates are assigned with sliding adjusters. Typically the variables fine tuned on a daily basis are the initial time and position of the laser-matter interaction within the eTOF. Unless adjustments are made to the optical elements in the beamline, the calibration of the eTOF was found to be stable indefinitely. Day to day, only small adjustments were required. Likely these adjustments were the result of small variations in optical alignment of the light source into the interferometer each time the system was started.

Once calibrated, each frame of a delay scan is converted to a 1-D line-out of signal amplitude versus photoelectron kinetic energy. Compiling these together generates a spectrogram showing the photoelectron dynamics as a function of relative delay between the NIR and XUV fields. Further analysis of these spectrograms was done using a Fast Fourier Transform (FFT) along the delay-axis to define the frequency of oscillations present in the spectrogram. For many scans, multiple peaks were observed in the FFT, a fundamental frequency and several harmonics. This was anticipated from some basic modeling using the SFA, see Chapter 4 for more details, where it was established that the lowest frequency, and always the strongest, corresponded to the frequency of the NIR field, for even and odd-ordered harmonic combs, or twice that for odd-ordered combs. Deeper insights into the photoelectron dynamics were extracted by analyzing the phase content of the fundamental mode of oscillation in delay scans.

2.6.2 Ion mass-to-charge Spectra

For all of the data reported in this thesis, the photoelectron spectra were calibrated using the emission from the NIR light in isolation. As the tunnel ionization rate scales exponentially and inversely with Ip, the field strengths required to drive NSDI were sufficient to saturate the ionization of all contaminant species in the detector. The largest source of contamination was the atmospheric gases leaking in through the gas delivery service, so the peaks for H_2O^+, N_2^+, O_2^+, Ar^+, and H^+ were consistent references for calibration. Similar to the eTOF calibration, the initial time and position of the light-matter interaction were the

variables adjusted. Calibrations of the TOFMS were very sensitive to the voltages applied to the needle gas source, which in turn needed to be adjusted daily for maximum collection efficiency of the ions. Unfortunately, the read out system for the applied voltage only displayed three digits, and the collection efficiency was sensitive to changes on much smaller scales. Day to day adjustments of this applied voltage, and therefore the calibration, were likely the result of thermal or mechanical drifts in the varistors used to control the applied voltage.

Once calibrated, it is useful to convert the data from counts versus mass-to-charge ratio to data binned by ion species. Each atomic species produces a Gaussian peak in the converted data, as the recoil energy and initial position are randomly distributed at the interaction region causing a broadening of the measured mass-to-charge ratio. The binning procedure was a 5 step process: 1) a 1-D Gaussian filter is used to smooth the data, 2) a peak is identified identified within small window of the data centered on the known mass-to-charge ratio of a single species, 3) a Gaussian distribution is fitted to the peak identified, 4) this fitted Gaussian is subtracted from the data, and 5) the subtracted data is used to identify identify and fit the next species following steps (2)-(5). Steps (4) and (5) in this procedure is particularly important for measurements of He^{2+}, m/q = 2.001, where its distribution in mass-to-charge ratio can overlap with that of H_2^+, m/q = 2.016. A histogram is then generated by integrating the original data set within the FWHM of the fitted Gaussian distribution.

The final step of the data pipeline is a Fourier analysis similar to that used for the photoelectron spectra. For a given species, the integrated counts versus delay is passed through an FFT to identify the primary frequencies of oscillation. Typically the TOFMS data only oscillated at the 1-ω frequency of the fundamental and so oscillations were easily identified when observable without any background subtraction or additional analysis steps.

Chapter 3
High Harmonic Generation

"A process cannot be understood by stopping it. Understanding must move with the flow of the process, must join it and flow with it."

- Frank Herbert, Dune

3.1 Overview

In this chapter, I will discuss the theoretical considerations and practical limitations for generating the APT used in these SFS experiments. HHG is the key to accessing the attosecond timescales desired for SFS experiments and is itself a product of strong field ionization and recombination, as discussed in Chapter 1. The defining feature of HHG, as opposed to other methods of nonlinear frequency conversion, is the presence of a broad plateau in the energy spectrum [83], see Figure 3.1. This plateau region produces the spectral bandwidth required to generate attosecond bursts of XUV light, and the current world record for the shortest pulse of light utilized HHG to achieve a pulse duration of 43as [41].

3.1.1 Ideal Attosecond Pulses

The ideal driver for ionization in an SFS experiment would be a single Isolated Attosecond Pulse (IAP) with a pulse duration orders of magnitude smaller than the optical period of the NIR field. A short IAP would sample a narrow group of ionization phases at a particular cycle in the NIR field. This would allow for the greatest resolution in selecting trajectories and would allow for the simplest interpretation of experimental results. Having

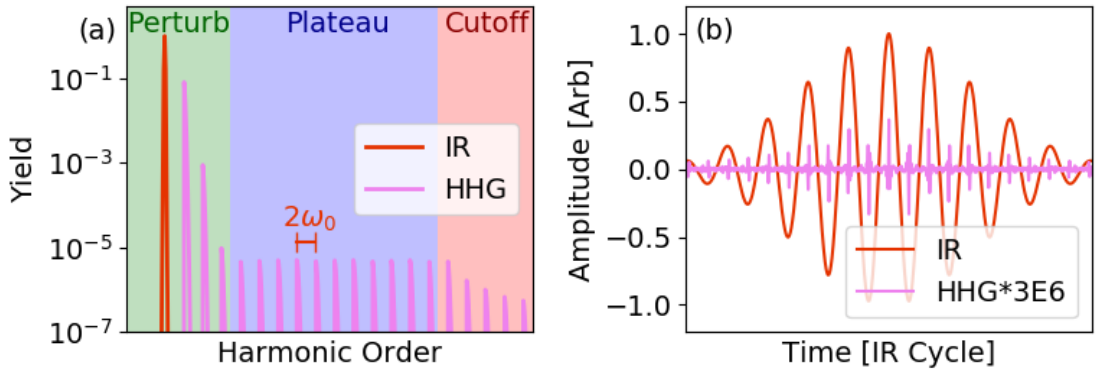

Figure 3.1: Cartoon of HHG

(a) a typical HHG spectrum consisting of three distinct regions: the perturbative low order harmonics resulting from more traditional nonlinear multiphoton processes, the plateau region where 10s to 100s of eV of bandwidth can be generated with comparable amplitudes, and the cutoff where the highest energy harmonics from recollision are produced. The harmonic are spaced by twice the frequency of the fundamental, ω_0. (b) in the time domain this spectrum produces a train of attosecond pulses, with bursts occurring twice per NIR cycle.

an IAP would also allow for more careful explorations of multi-cycle recollision effects such as frustrated tunneling ionization [86] or the Low Energy Structure (LES) in the photoelectron spectrum [9][110].

In the frequency domain, this idealized IAP would have a narrow spectrum with photon energies centered on the Ip of the atomic or molecular target to be studied. This would reproduce the assumption of the SFA model that tunneling electrons exit the atomic potential with zero initial kinetic energy. Of course, producing a narrow spectrum directly competes with the desire for the shortest pulse in the time domain but a reasonable compromise is possible. For a NIR wavelength of 1.7 μm and period 5.67 fs, a transform limited Gaussian pulse of 500 as duration only requires 3.64 eV of bandwidth. Further developments of ultrafast pulse generation at longer NIR wavelengths will further relax these constraints on SFS experiments.

3.1.2 Experimental Constraints

Having described the ideal attosecond pulse for SFS experiments, its worthwhile to explore the practical limitations on generating such a pulse. First and foremost, a NIR pulse shorter than 2-cycles is needed to generate the continuum of harmonics required to make an IAP. Other techniques for generating IAP, such as double optical gating [13], have yet to be implemented wavelengths longer than 1 μm. A 2-cycle pulse can be made in the NIR by spectrally broadening the pulse in a hollow core fiber [41], however the conversion efficiency of such process is $\sim 50\%$. For an experiment so strained for pulse energy as the SFS, these conversion losses in generating an IAP are difficult to overcome. Conversely, there is a substantial benefit to using an APT for SFS experiments. For an APT generated by a 2-color NIR field the pulses are spaced by precisely a NIR period, see 3.3, and each pulse will interact with the same phase of NIR field. Therefore, the measured signal will be the result of a coherent superposition of each of the individual pulse and there is an N^2 enhancement of the signal where N is the number of attosecond pulses [81]. This type of enhancement can be essential to observing low probability events such as electron recollision and an APT was used for the SFS experiments in this dissertation.

3.1.3 My Contributions

I was responsible for the design, assembly, and testing of the components used in HHG for this dissertation. I also realigned the XUV spectrometer used to characterize the piezo valve performance, see Appendix B, with assistance in carry out these measurements from Bryan Smith. Qiaoyi Liu aided me in optimizing the optical layout of the half-wave plates and Beta Barium Borate (BBO) crystal needed for the 2-color HHG setup. I analyzed all of the data shown in this chapter and generated the plots.

3.2 Generation Conditions

One of the primary limitations of the previous generation of SFS experiments, was the relative ionization rate between the single-photon mechanism of the XUV light and the

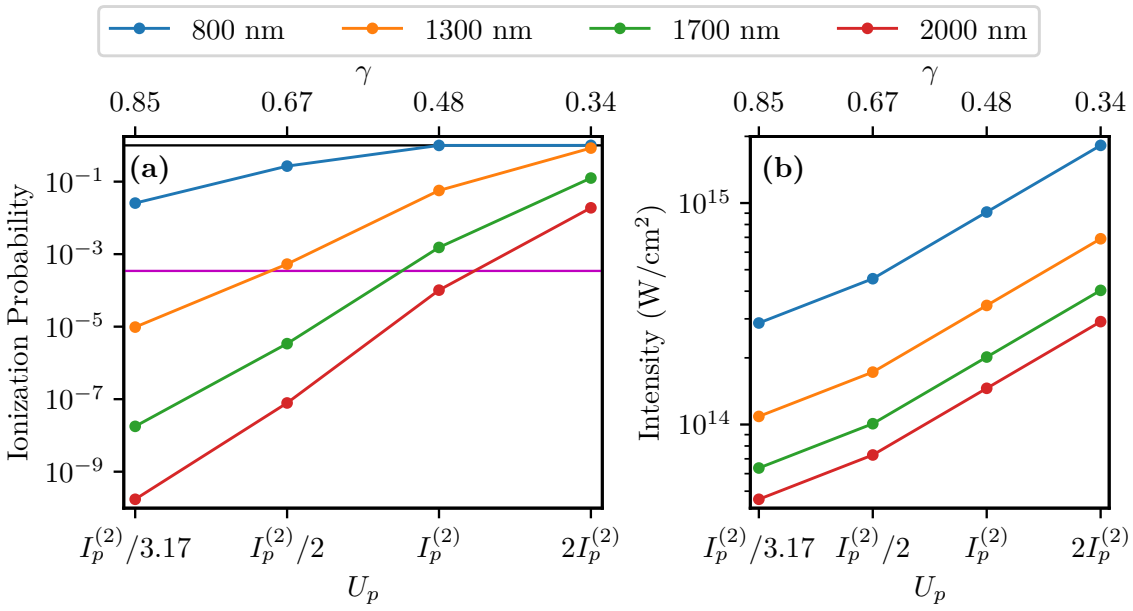

Figure 3.2: Ionization probability of helium.

(a) the probability of tunnel ionizing helium with a pulse of FWHM 60fs for various IR wavelengths using the ADK ionization rate [5]. The horizontal purple line represents an expected ionization rate from the XUV comb. Up is reported as a fraction of the second ionization energy of helium, and also as the Keldysh parameter gamma on the top axis. (b) the commensurate intensity is plotted against Up. Adapted from [59]

tunneling ionization of the NIR light. Therefore, maximizing the XUV flux is essential to this latest generation of SFS experiments. The tunneling ionization rate was reduced by switching to a longer wavelength source where larger ponderomotive energies can be achieved with less intensity. Figure 3.2 illustrates the scaling of the tunneling ionization rate as a function of NIR intensity for various wavelengths. The Keldysh Paramater defined as $\gamma = \sqrt{\frac{Ip}{2U_p}}$, is also provided.

Maximizing the yield of HHG is a matter of optimizing three quantities:

1. The number of driven dipoles (i.e. atoms or molecules in the gas phase).

2. The efficiency of each dipole.

3. The phase matching of the bulk sample (i.e. coherently adding each dipole).

In any nonlinear process there are numerous tunable parameters which affect these three

goals. Given the incredibly broad spectral range produced in HHG, there are that many more parameters and a sizable fraction are coupled together. Although numerical models can accurately reproduce the general features of HHG, when it comes to optimizing this process on a tabletop it is equal parts science and art.

3.2.1 NIR Light

As HHG is a result of strong field ionization, its foremost requirement is achieving sufficient intensity with the pump beam to drive tunneling ionization. For NIR wavelengths, this requires an intensity of order 10^{14} W/cm^2. Achieving this intensity typically requires an ultrafast laser system with a pulse duration of 10 - 100 fs and pulse energies $\sim$1 mJ. In these SFS experiments, 600 μJ pulses of 1.74 μm light with a pulse duration of 60 fs are used to generate harmonics. Both the field intensity and wavelength are key parameters in the HHG process. The cutoff, or highest observable harmonics, scales as $3.17 \times U_p$, where the Up $\propto I\lambda^2$. As discussed in the following section, there are practical limits to the intensity that can be applied, dependent on the generating medium, and so the most efficient means of creating broader combs is the use of longer wavelength drivers [89]. Unfortunately, with fixed intensity the transition to longer wavelengths yields dimmer harmonics as the conversion efficiency scales as $\sim \lambda^{-5.5}$. This results from the λ^2 increase in the width of plateau region, and a λ^{-3} scaling for the recollision probability in the semiclassical model [89].

Given the scalings of HHG with driving wavelengths, it may be counter-intuitive that SFS experiments are best conducted at longer NIR wavelengths. As mentioned previously, the key is to maximize the ionization probability of the target gas via single-photon ionization by the XUV light relative to the tunneling ionization via the NIR field. For a fixed bandwidth of harmonics, switching from 800 nm to 1.7μm should yield a 63x decrease in XUV flux. However, to achieve a given ponderomotive energy in the NIR/XUV interaction region, this change in wavelength decreases the intensity needed by a factor of 4.5x. The exponential scaling of the tunneling ionization rate means that for a 60 fs pulse, this relatively small change in intensity will reduce the tunneling ionization probability by 3 - 6 orders of

magnitude within the intensity range of interest, see Figure 3.2. This scaling persists for even longer wavelengths in the NIR, and the upper bound on driving wavelength is the ever decreasing number of events per laser shot approaching the statistical limits on making an observation in finite integration times.

3.2.2 Generation Gas

Selection of which species to generate the harmonics in is primarily dependent on a single factor, the magnitude of it's Ip. The Ip impacts in two important ways. First, recall the dependence of the tunneling ionization rate on Ip [5]:

$$w_{ADK} \propto exp\left(-\frac{2(2I_p)^{3/2}}{3F})\right) \tag{3.1}$$

Where w_{ADK} is the ionization rate in the tunneling regime given by the ADK equation and F is the field strength of the pump. This exponential scaling can provide dramatic increases in the ionization rate for even small reductions of the Ip. Given a particular Ip and pump pulse we can define a saturation intensity at which 98% of the gas sample is tunnel ionized at the peak of the pulse. For a sech^2 pulse with FWHM 65 fs, the saturation intensities of argon (Ip = 15.76 eV) and xenon (Ip = 12.13 eV) are 3.3×10^{14} W/cm^2 and 1.3×10^{14} W/cm^2 respectively [96]. Therefore, lower Ip targets allow for looser focusing to achieve similar ionization fractions within a larger focal volume, and correspondingly an increased number of atoms/molecules undergoing HHG assuming a constant gas density. If the focus of a fixed pump pulse is tuned so that the peak intensity matches the saturation intensity of the generating gas, the focal volume for xenon will be 16.35x larger than that for argon.

The Ip of the generating gas also impacts the distribution of harmonics. The spectral cutoff of HHG is located at $I_p + 3.17 \times U_p$, so increased Ip directly increase the extent of the harmonic comb. Indirectly, the higher saturation intensity for larger Ip targets allows for increased U_p further extending the cutoff energy. For 1.7μm light at the saturation intensity for argon (xenon) above, the U_p=89.1 eV (35.1 eV). As these SFS experiments requires harmonics close to the ionization threshold of the target, <25 eV for all gases, xenon is an excellent choice for the HHG medium. Xenon does add significantly to the cost

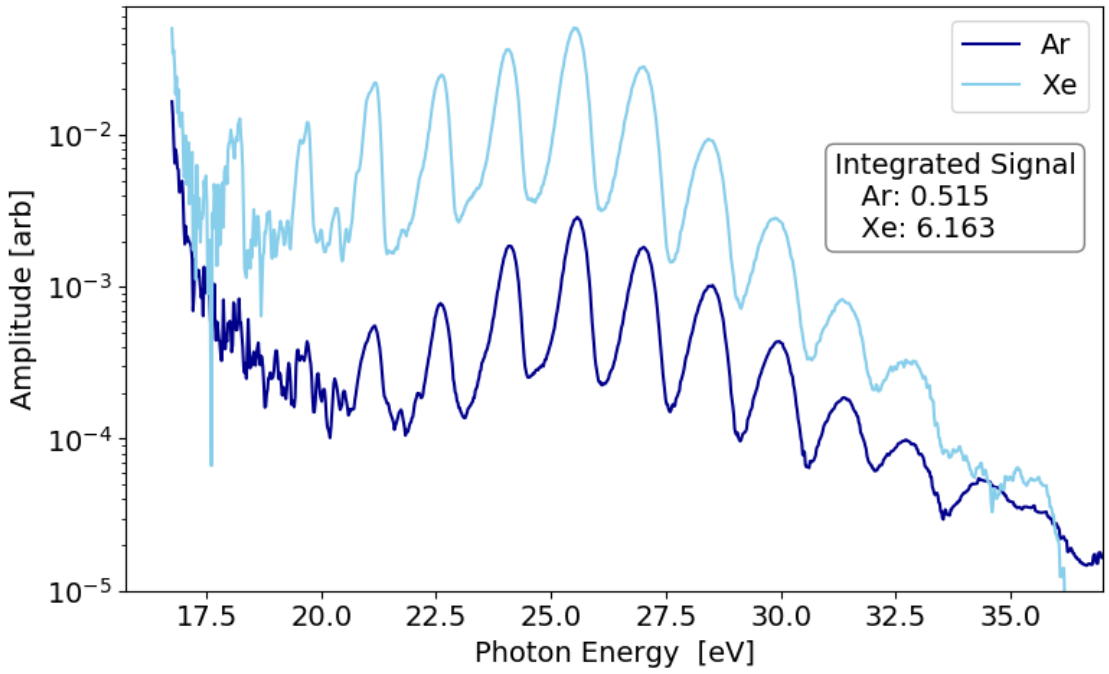

Figure 3.3: Comparison of HHG in xenon and argon

Comparison of single color HHG yield from xenon and argon with a laser pulse of wavelength 1.7μm, pulse energy 600 μJ, and duration 60 fs. These harmonic yields were measured by collecting photoelectrons from argon and dividing the signal by the absorption cross-section. The same focal spot size was used for each, though the placement of the gas source and input aperture size were changed to optimize the phase matching. Integrating the total signal, xenon produces 12x the amount of XUV light as argon.

of this experiment, but the pulsed gas valve (duty cycle 7%) helps to reduce the gas usage significantly compared to a continuous gas flow.

Lower Ip targets than xenon are readily available in molecular targets such as ethane (C_2H_6), nitrous oxide (N_2O), nitrogen dioxide (NO_2), and carbonyl sulfide (OCS) [61]. However, the scalings of HHG with Ip outlined above are built on models of atomic strong field ionization [109]. Studies of molecular ionization shows that molecular targets can have increased saturation intensities relative to the ADK prediction from the Ip alone [46]. However, HHG in molecules likely involves multiple molecular orbitals in both ionization and recombination [3, 109], and so the total HHG yield from any particular molecular target is difficult to predict without sophisticated simulations. Oxygen (Ip = 12.08 eV) was tested

as an HHG target for these experiments, but the harmonic yield was an order of magnitude less than xenon. The experience of the DiMauro Research group is that xenon is the optimal species for maximizing harmonic yield at low photon energies and was used in these SFS experiments.

3.2.3 Phase Matching

Efficiently generating harmonics in the gas phase requires all of the independent atoms to be oscillating in phase with one another, so that the radiation from each adds constructively. Borrowing the nomenclature from traditional nonlinear frequency conversions, we refer to this requirement as phase matching. In Equation 3.2 the phase mismatch for harmonic q is defined as the difference between q times the fundamental wavenumber and the wavenumber of the q^{th} harmonic. Phase mismatch for each harmonic stems from four primary mechanisms: the chromatic dispersion of the generating gas (*neutral*), similarly the dispersion of the ionized gas (*plasma*), the geometric phase evolution of the pump beam (*Guoy*), and the phase delay between the pump beam and oscillating electron in the semiclassical model (*dipole*).

$$\Delta k_q \equiv k_0 - k_q = \Delta k_{neutral} + \Delta k_{plasma} + \Delta k_{Guoy} + \Delta k_{dipole} \tag{3.2}$$

k, the wavevector, takes its typical definition as $2\pi/\lambda$, where λ is the wavelength. Optimal phase matching occurs when the absolute magnitude of Δk_q is minimized [14].

The first two terms $\Delta k_{neutral}$ and Δk_{plasma} stem from the frequency dependent index of refraction, which is a linear function of the pressure (ρ), or number density, of the gas or plasma. The fraction of atoms ionized by the pump beam (η) adjusts the effective value of ρ accordingly. The phase mismatch of the charge neutral gas is:

$$\Delta k_{neutral} = \frac{2\pi q}{\lambda_0}(1-\eta)\frac{\rho}{\rho_0}\Delta n \tag{3.3}$$

Where λ_0 is the wavelength of the pump beam and Δn defined as the difference in the index of refraction for the fundamental and q^{th} harmonic. For NIR pumps beams and noble gas generating media, Δn is always positive. Experimental values for Δn are readily available

at standard temperature and pressure (ρ_0). For xenon gas Δn is equal to 7×10^{-4} for the XUV bandwidth of interest in these SFS experiments [14].

The plasma dispersion can be derived from the classical calculation for the index of refraction for a plasma. After rearranging terms Equation 3.4 gives the phase mismatch of the plasma:

$$\Delta k_{plasma} = -q\eta\rho r_e \lambda_0 \tag{3.4}$$

Where r_e is the classical electron radius defined as:

$$r_e \equiv \frac{1}{4\pi\epsilon_0}\frac{e^2}{m_e c^2} \tag{3.5}$$

e is the electron charge, m_e the electron mass, ϵ_0 is the vacuum dielectric constant, and c is the speed of light. What is notable here is that the plasma phase mismatch is always negative, as opposed to the positive dispersion of the neutral gas, and scales linearly in pressure, same as the neutral gas. Therefore, a critical ionization fraction can be defined for which the phase mismatch of these two terms is zero.

$$\eta_c = \left(1 + \frac{\rho_0 r_e \lambda_0^2}{2\pi\Delta n}\right)^{-1} \tag{3.6}$$

For xenon with a pump wavelength 1.7μm the critical ionization fraction is $\sim$2%. As such optimal HHG often occurs at intensities below the saturation intensity of the generating gas as discussed in the previous section.

The next two terms in the phase mismatch are governed by the geometrical features of a focused beam, the first is the phase evolution on axis. For a gaussian beam profile this is referred to as the Guoy phase and takes the following form:

$$\Delta k_{Guoy} = q\frac{2b_0}{b_0^2 + 4z^2} - \frac{2b_q}{b_q^2 + 4z^2} \tag{3.7}$$

Where b_x is the confocal parameter, twice the Rayleigh range, and z is the distance from the beam waist along the propagation axis. This term is typically negative [96].

The last term relates to the total phase excursion of the electron trajectory that results in generating harmonic q, which is a function of intensity. Since the intensity of the driving

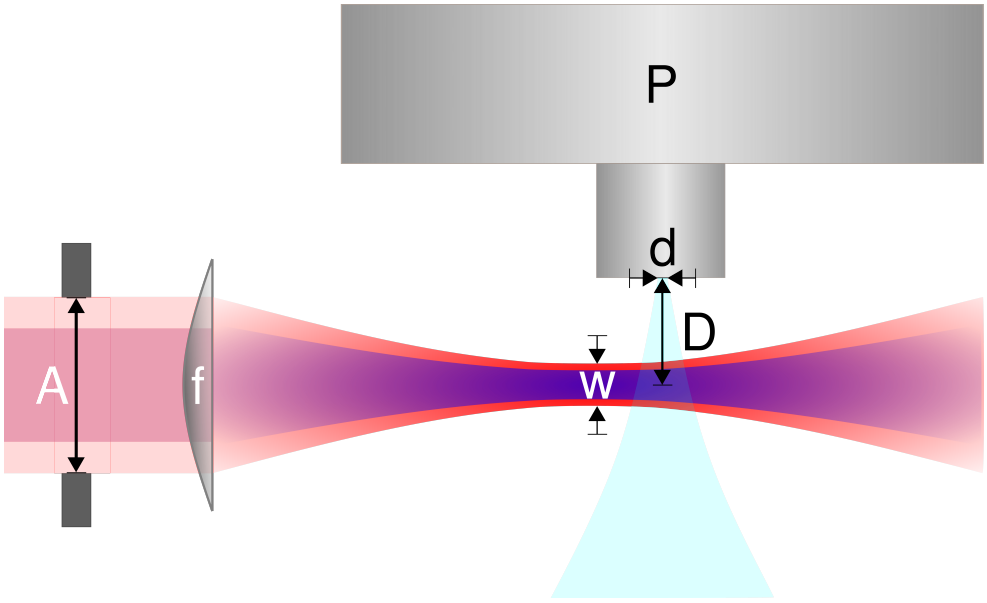

Figure 3.4: Schematic of HHG conditions

For these SFS experiments a 2-color IR field is focused into a pulsed gas jet of xenon gas. The phase matching of the HHG, and therefore the XUV yield, depends on the following parameters: A the input aperture size, f the focal length, d the gas nozzle diameter, D the distance between the IR waist and nozzle, and P the backing pressure of the gas source.

field will increase as it approaches the focus, and decrease after, the sign of the dipole phase depends on the relative location of the gas medium and the laser focus. This dipole phase mismatch is defined as:

$$\Delta k_{dipole} = -\alpha_q \frac{\delta I}{\delta z} \tag{3.8}$$

Where α_q takes on different values depending on the class of trajectories. Typical values are $\alpha_q = 2 \times 10^{-14}\ cm^2/W$ for short trajectories, and $\alpha_q = 22 \times 10^{-14}\ cm^2/W$ for long [7, 56].

In any given experiment, the readily available controls for optimizing the phase matching are depicted in Figure 3.4. Some general rules of thumb follow. Placing the gas medium around one Rayleigh range after the beam focus is optimal, as near here the *dipole* and *Gouy* phase mismatches will cancel for the short trajectories [91]. The loosest focus, largest value for f, for which a visible plasma appears will maximize the total yield. The distance D, should be set so that the laser focus is centered on the Mach disk of the supersonic gas

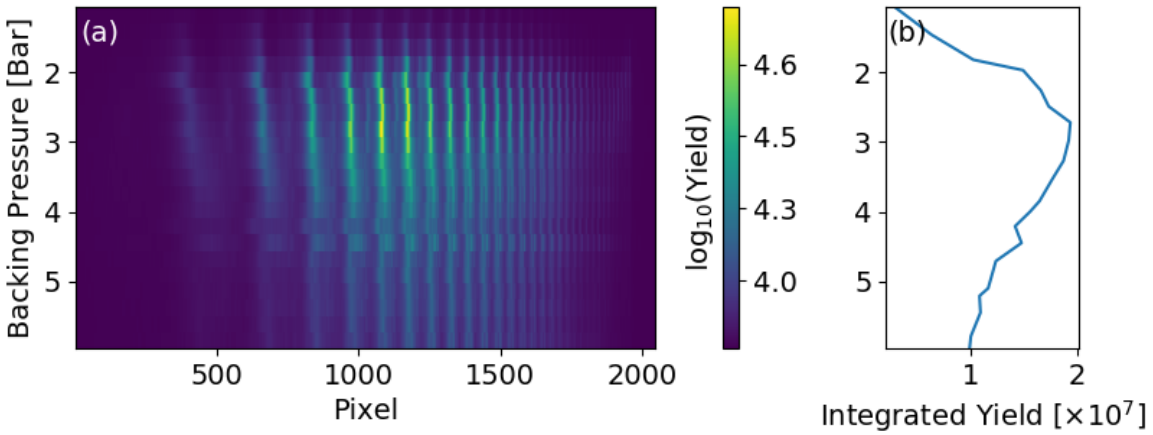

Figure 3.5: XUV spectrum versus backing pressure

(a) XUV spectrum scanning the backing pressure of the pulsed piezo valve. This data was recorded with 2 mJ of 1.7μm light, xenon gas generating, a 25 cm focal length lens, and an XUV spectrometer with a CCD camera. Absolute pressures are reported. (b) the total yield increases quadratically as a function of pressure up to the optimal interaction pressure [14], with a maximum at a pressure of ~2.8 Bar.

jet formed by the rapidly expanding gas source [44]. For a continuous flowing gas jet in vacuum the Mach disk lies at $10 \times d$, where d is the diameter of the gas source aperture [85]. The aperture diameter simultaneously adjusts several parameters such as the on axis intensity and phase evolution, and adjustment of the aperture size often leads to significant increases in harmonic yield after all other parameters are optimized [57]. The backing pressure and gas source aperture size affect the density of the gas in the focal volume. A finite pressure which maximizes HHG yield always exists, where as the generating gas can begin to significantly reabsorb the XUV light at sufficient pressure [14]. Figure 3.5 shows the XUV spectrum generated with the piezo valve as measured by a spectrometer. Maximum HHG yield is observed at a backing pressure of 2.8 Bar absolute pressure. For further information about the testing of the piezo valve see Appendix B.

3.3 2-Color HHG

One limitation of traditional HHG with a single color laser pulse, is the production of two XUV pulses per laser cycle. For the purposes of SFS experiments, there are significant

advantages from the coherent addition of all the pulses in the APT interacting with the same phase of the NIR light [81]. To produce a harmonic comb with only a single burst per cycle, and correspondingly both even and odd harmonic orders, a two color field mixing the NIR light with its second harmonic can be used [15, 80].

3.3.1 Field Symmetry Breaking

The fundamental concept extends from perturbative nonlinear optics where a centrosymmetric system is incapable of generating even ordered harmonics [10]. For single atom gases, there is no means of breaking of this symmetry within the generating medium. Instead, even order harmonics can be produced by breaking the symmetry of the field [80]. As shown in Figure 3.6(b), the addition of a small amount of the second harmonic can create a synthesized field similar to the fundamental but with asymmetric amplitudes on the positive and negative half cycles. In these experiments, a 5 to 1 intensity ratio between the fundamental and second harmonic fields was found to produce the APT with the largest flux.

3.3.2 Second Harmonic Generation

Generating the second harmonic of an ultrafast laser pulse, as used in these experiments, can be as simple as adding a crystal such as BBO along the beam path. What complicates matters in this experiment is the need for the fundamental and second harmonic to both be p-polarized and coincident at the point where HHG occurs. For Type I phase matched second harmonic generation, the second harmonic is polarized perpendicular to the fundamental [10]. Matching polarizations requires some means of independently rotating the polarization of one color independent of the other. This can be done by rotating the polarization of the fundamental with a $\lambda/2$ waveplate, or a $\lambda/1$ waveplate for the second harmonic so that the polarization of this color is unchanged. The GDD of any transmissive optics subsequent to the second harmonic generation will separate the two pulses in time. Returning the pulses to coincidence requires some transmissive material, usually with birefringence or anomalous dispersion, to delay one pulse with respect to the other. Rotation of

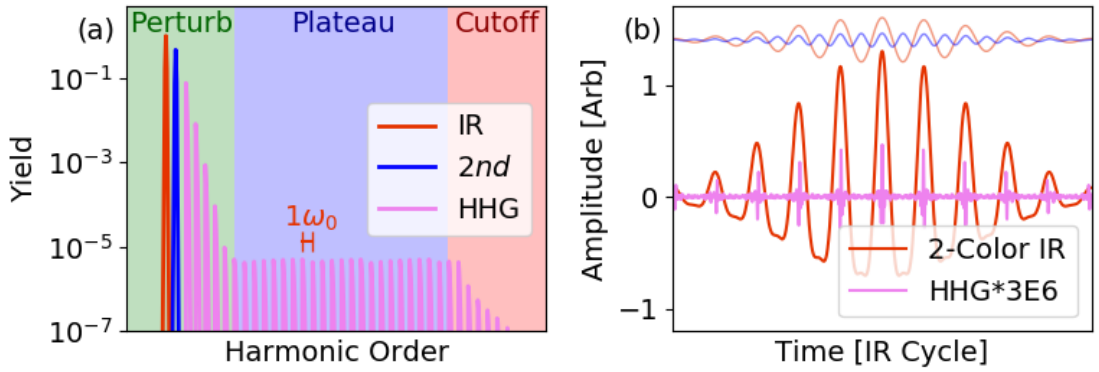

Figure 3.6: Cartoon of 2-color HHG

(a) resulting HHG spectrum when the fundamental is mixed with its second harmonic, and this two color field is used to generate harmonics. The harmonics are now spaced by the fundamental frequency. (b) correspondingly in the time domain a burst of attosecond light is produced once per IR cycle, as opposed to twice in Figure 3.1. The mixing of the fundamental with a small amount of its second harmonic, at a specific phase offset between the fields, breaks the up-down symmetry of the IR field allowing for the generation of even-ordered harmonics.

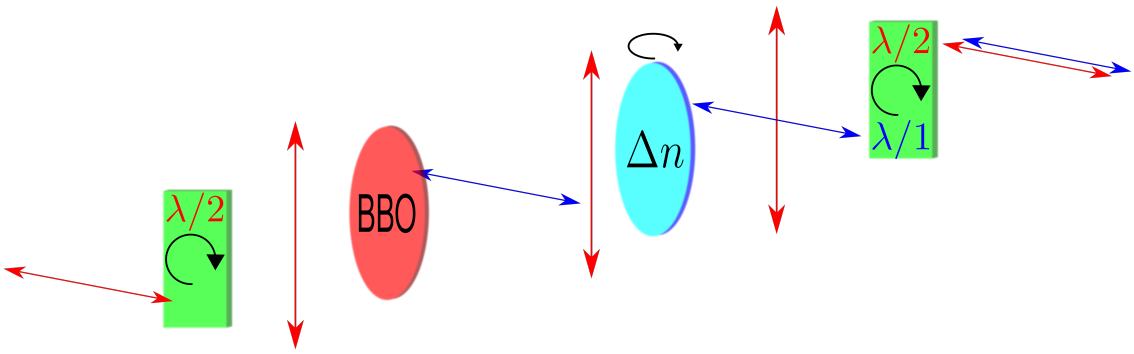

Figure 3.7: Second harmonic generation scheme

The fundamental beam begins p-polarized so as to be aligned with the TOF axis. A $\lambda/2$ waveplate rotates the polarization 90°. Type I second harmonic generation produces light along the extraordinary crystal axis, so as to be p-polarized. Typically, GDD accumulated from glass downstream will cause a delay between the fundamental and second harmonic, so this is compensated for in advance (Δn). Another $\lambda/2$ waveplate rotates the s-polarized fundamental to p-polarized, matching the second harmonic which experiences a π rotation for no change in polarization.

this delay compensator allows for sub-cycle control over the relative phase of the two fields. Figure 3.7 illustrates this procedure.

In these experiments, the NIR light was sent through a BBO crystal of 300 μm thickness cut at an angle of 29° with respect to the optical axis. The pulse energy of 600 μJ was split 5 to 1 between fundamental and second harmonic for optimal harmonic yield. The fundamental begins p-polarized, and must return to p-polarization, and the $\lambda/2$ waveplate will only rotate the fundamental's polarization. This means the polarization must be rotated prior to the second harmonic generation with an additional $\lambda/2$ waveplate. Around 1.7 μm the group velocity dispersion of common glasses such as Fused Silica and CaF_2 in the NIR can be rather small, order 10 fs^2/mm. The number of transmissive optics between the BBO and the point of HHG was only two, a 3 mm thick CaF_2 window and a $\lambda/2$ waveplate of fused silica with thickness less than <2 mm. The net result is that the two pulses were separated in time by 10's of fs, but it would take a very thin piece of calcite to compensate for this GDD, order 10 μm, which was not readily available. A simple solution was to tune the wavelength of the fundamental to find a point where the anomalous dispersion of the BBO canceled out the dispersion of the subsequent optics. This was found to occur at 1740 nm. The relative phases of the two fields were controlled by small rotations of the BBO to find the optimal conditions for HHG.

3.4 Spectral Shaping

As discussed in 3.1.1, an SFS experiment requires an attosecond pulse with a narrow spectrum centered on the Ip of the atom or molecule to be studied. However, HHG produces a broad plateau extending 10s of eV. Selecting a generating gas with low Ip can reduce the spectral extent of the plateau, and the reduced saturation intensity will compel the experimenter to decrease the pump intensity and therefore the cutoff photon energy. Optimized phase matching will also allow for an increased yield in a particular band of harmonics. The use of xenon and experimental design choices can make some progress along these lines, but these means of attenuating the bandwidth were insufficient for the SFS. A combination

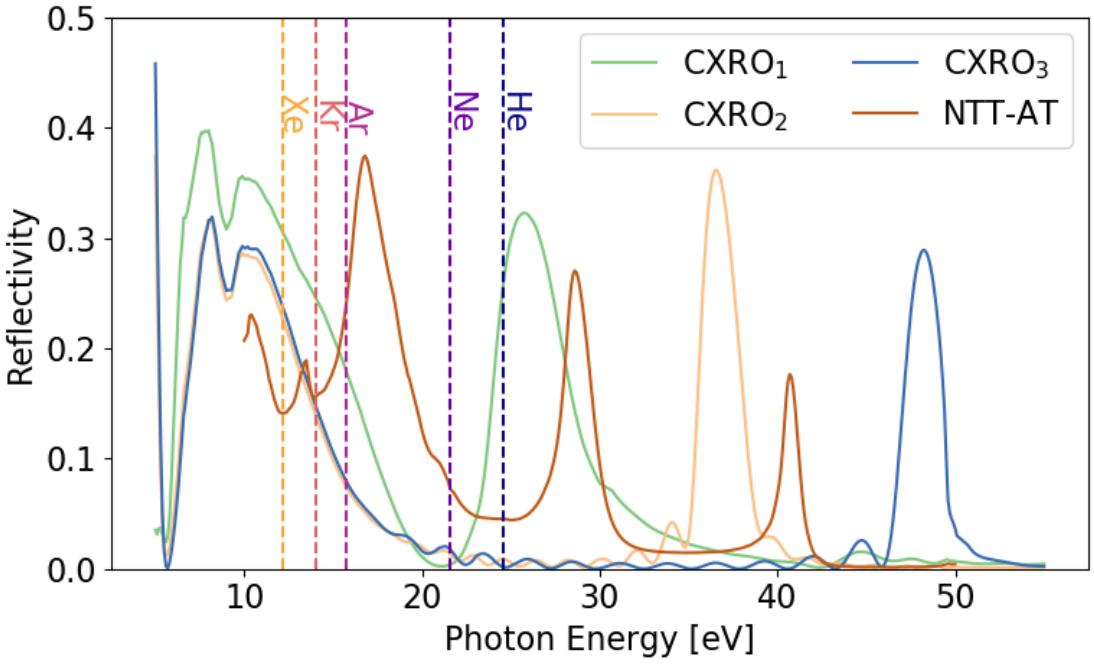

Figure 3.8: Multi-layer mirror reflectivity in the XUV

Reflectively of several multi-layer mirrors procured for these SFS experiments. Each of these are calculated curves based on ideal deposition at a fixed angle, CXRO at 6.5° and NTT-AT at 5.0°. Ionization potentials of noble gas atoms are plotted as vertical dashed lines. Data provided by CXRO and NTT-AT.

of transmissive filters and multi-layer mirrors were the primary means of controlling the bandwidth of XUV light from HHG.

3.4.1 XUV Multi-Layer Mirror

At near-normal incidence angles, multi-layer dielectric coatings can offer tailored reflectivity bandwidths in the XUV region. For the photo energy range of interest in these experiments, typical multi-layer coatings are made from magnesium and silicon carbide. In collaboration with The Center for X-Ray Optics (CXRO) three mirrors were custom manufactured for these SFS experiments. Their predicted spectral reflectivity are plotted in Figure 3.8. The mirror labeled $CXRO_1$ was used for the SFS experiments reported in this dissertation. The $CXRO_2$ and $CXRO_3$ are interesting candidates for future studies where the photoelectrons

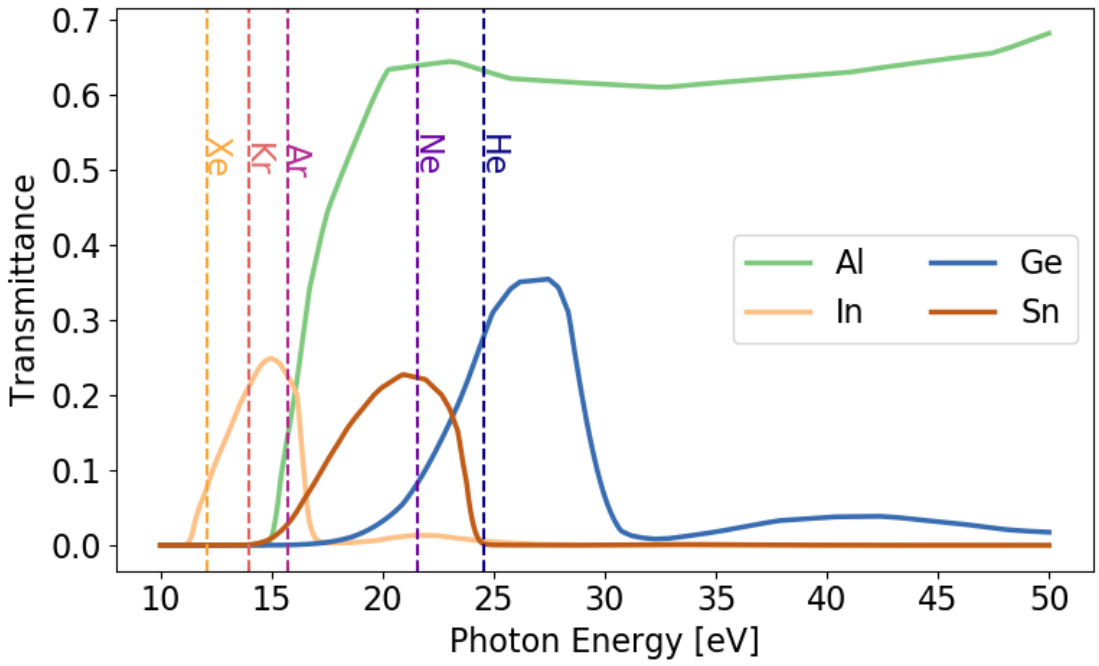

Figure 3.9: Metallic foil transmittance in the XUV

Transmittance of common thin metallic foils in the XUV energy range of interest in SFS experiments. Each filter is assumed to have a thickness of 200 nm. Ionization potentials of noble gas atoms are plotted as vertical dashed lines. Data retrieved from [47].

are launched into the continuum with significant kinetic energies, a new domain of strong field physics so far unexplored. In addition, a fourth mirror has been procured from NTT Advanced Technology Corporation (NTT-AT) with a bandpass effective for future SFS experiments in argon.

3.4.2 Metal Foil Filter

Thin nanometer scale metallic foils are common ingredients in attosecond interferometers to separate residual amounts of IR light from the XUV after HHG. Figure 3.9 shows the transmission function of several mono-atomic foils of 200 nm thickness in the range of 10-50 eV [47]. Aluminum provides a broad band transmission for experiments desiring the largest possible bandwidth. Germanium, tin, and indium, are excellent choices for providing narrow bandwidths close to the ionization threshold of helium; neon; and xenon, krypton,

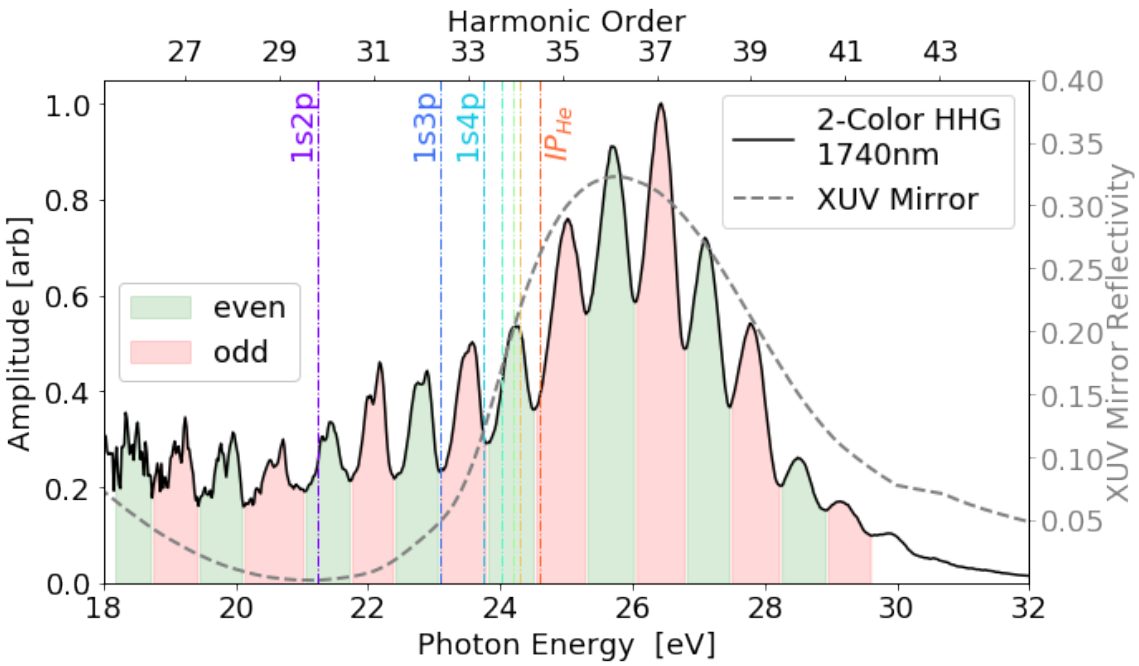

Figure 3.10: HHG spectrum used in these experiments

The XUV mirror attenuates the bandwidth of harmonics to a narrow comb close to the ionization energy of helium. The XUV Mirror reflectivity displayed is the result of a numerical prediction, and the behavior for greater photon energies is more accurate than the lower. With a fundamental wavelength of 1740 nm, several harmonic 34 overlaps several Rydberg resonances in helium. However, the lower resonances with significantly greater oscillator strengths are largely avoided. Helium energy levels are retrieved from [63].

or argon respectively. Unfortunately, thin foils of germanium often require capping layers of aluminum to reduce oxidation meaning the transmission efficiencies of such filters can be very small. In the SFS experiments in this dissertation a 100 nm thick aluminum filter was used, and the XUV Mirror provided the required bandwidth attenuation.

3.5 Final Comb

Figure 3.10 shows the final comb of harmonics used in these experiments. This distribution was measured through photoionization of argon, and the absorption cross-section has been removed to render the ordinate axis to spectral amplitude. Notably the XUV Mirror does not attenuate the lower energy range of 18 - 23 eV as anticipated, though this is attributed

to limits of the numerical simulations. With a center of mass photon energy of 24.65 eV and standard deviation of 3.02 eV, this comb meets all the requirements on the XUV distribution to conduct SFS experiments in helium (Ip = 24.59 eV)

One unforeseen complication, was the significant yield of harmonics still present below the ionization threshold of helium. As can be seen in Figure 3.10, the first excited state of helium, 1s2p, is located at what was predicted to be a local minima in the XUV Mirror reflectivity. Similarly, lower flux was anticipated at the second excited state, 1s3p. Chapter 4 will discuss the experimental signatures associated with these excited states and their possible role in these experiments.

3.5.1 Pulse Characterization

Up to this point the amplitude distribution has been discussed, but it is worth considering the phases as well. Significant chirp would result in different photon energies interacting with significantly different phases of the NIR field complicating the interpretation of results. For odd order combs RABBITT can be used to extract the spectral phases of an APT. In principle, analogous techniques are available for the even and odd ordered combs used in these experiments. However, previous implementations of these more complex techniques in the DiMauro group have proven them to be unreliable. For this reason, a RABBITT measurement at a laser wavelength of 1.7μm was used to provide a benchmark pulse duration, see Figure 3.11. With an intensity FWHM of 366 as, the duration of individual pulses in this APT are $< 1/15$ an optical period of the fundamental. A transform limited pulse would have a FWHM duration of 355 as. The spectrogram of the RABBITT experiment used in this pulse reconstruction is shown in Figure 3.12.

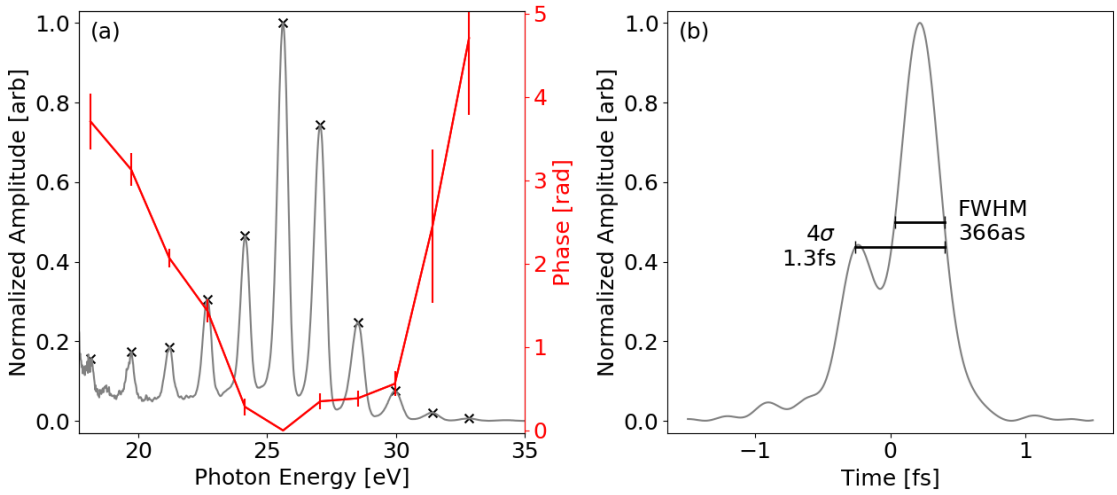

Figure 3.11: Pulse characterization

(a) harmonic comb from single color HHG with 1.7μm light. The x markers indicate the harmonics with sufficient amplitude that they were used in the pulse reconstruction. The red curve indicates the phases measured for each harmonic from the RABBITT measurement in Figure 3.12. (b) the intensity of the attosecond pulse reconstructed from the amplitudes and phases in panel (a).

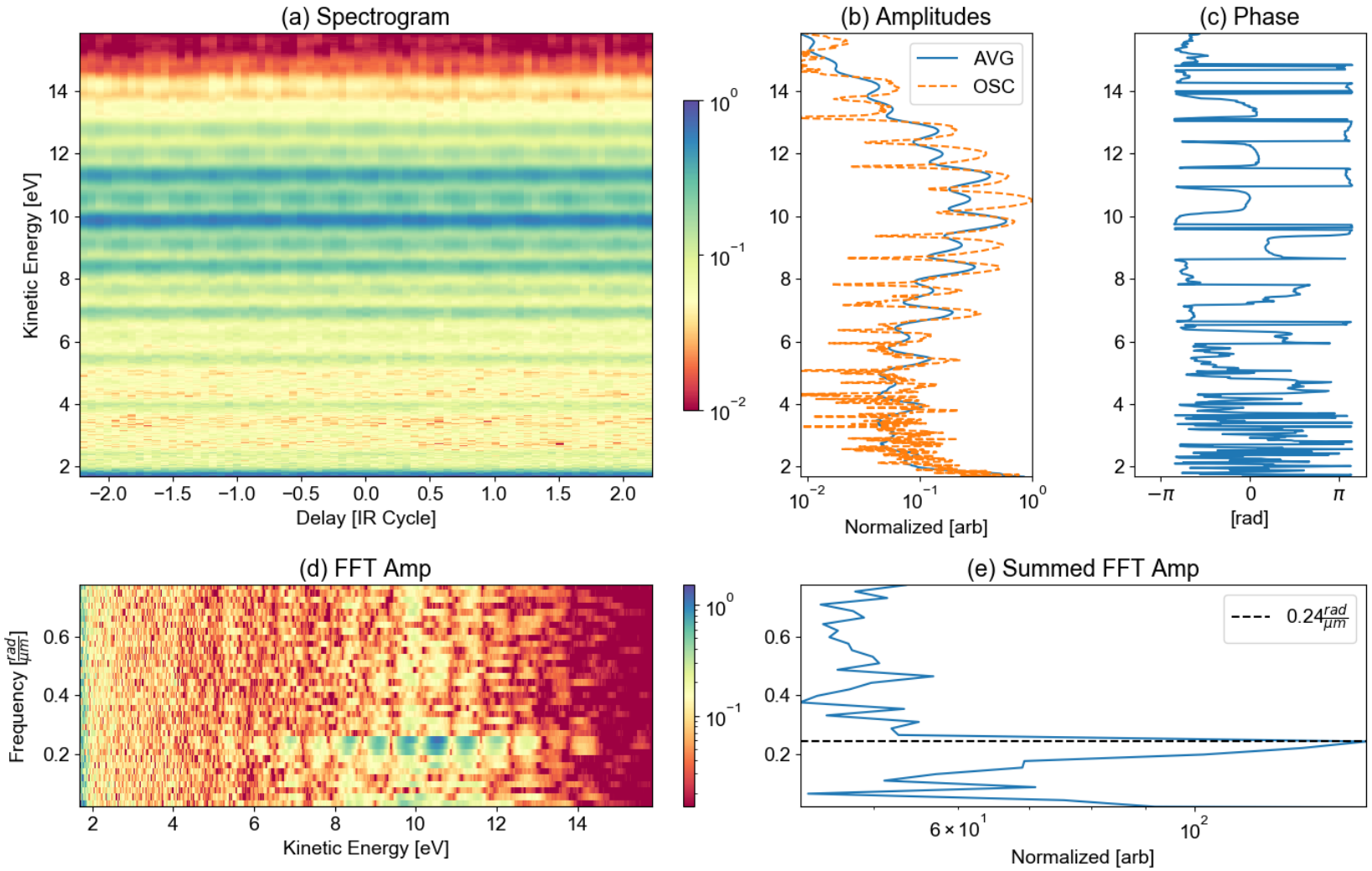

Figure 3.12: RABBITT for APT generated at 1.7 μm

(a) RABBITT spectrogram for harmonics using argon as the detection gas. (b) lineout of the amplitudes averaged over delay from the spectrogram, as well as the oscillation amplitude after the Fourier filter is applied. (c) the wrapped phases extracted from the 2ω oscillation. (d) heatmap of the Fourier decomposition versus kinetic energy. (e) the amplitudes of the Fourier decomposition summed over all photoelectron kinetic energies. The primary oscillation occurs at 0.24 $rad/\mu m$ which is anticipated for a 2ω oscillation of a 1.7μm field for the delay wedges described in subsection 2.4.3.

Chapter 4
Helium Experiments

"You can prove anything you want by a coldly logical reason – if you pick the proper postulates."

– Isaac Asimov, I, Robot

4.1 Overview

In this chapter, I will present the results of my SFS experiments in helium. I'll begin with the ion yield data where I observed a two-color enhancement that suggests XUV-seeded recollision was occurring. Then in the photoelectron data, I will show that I failed to observe any clear signatures of recollision and discuss the experimental limitations that likely prevented this observation. Finally, I'll discuss some experimental signatures of the XUV driving electrons into excited bound states, and the possibility that these can affect the results of the SFS experiments.

Note that these experiments were all conducted under identical experimental conditions, only attenuating the intensity of the NIR field with a pair of wire grid polarizers. The polarization of the NIR field was fixed parallel to that of the XUV and TOF axis.

4.1.1 My Contributions

Helium has been the primary target I set out to study, and all of the experimental decision making was done with the particular demands of helium in mind. I'm proud to have made the first observation of an XUV+NIR mechanism for double ionization of helium, suggesting the SFS concept of XUV seeded recollision works. I was responsible for collecting and

analyzing all of the data presented in this chapter. I developed the software to run the SFA simulations of the photoelectron data. Qiaoyi Liu assisted me in collecting the data, and running simulations.

4.2 Ion Data

Although counter-intuitive, for these experiments on ultrafast electron dynamics it is worth beginning the discussion with studies of the ion yield. Recalling Section 3.2, a successful SFS experiment requires the ionization rate due to single photon absorption of the XUV light to exceed the tunneling ionization rate due to the NIR field. Verifying that this requirement had been met was one of the first experiments conducted in this SFS campaign, and was frequently repeated throughout the course of the endeavor. In addition, Non-Sequential Ionization is a hallmark of electron recollision after strong field ionization and NSDI in helium is the most fundamental test bed for this effect, as helium has only two electrons interacting in the second ionization process. As discussed in Section 1.6, there is significant physics left to be understood about NSDI in helium likely involving electron correlation.

4.2.1 Single Ion Results

When studying photoelectrons without a coincident measurement of ion species, it is important to verify that the vast majority of electrons are coming from the target of interest. For SFS experiments it also important to discern the ionization mechanism producing these electrons. In Figure 4.1, the relative abundance of various ion species are plotted when only the NIR pulse is present, at the two largest NIR intensities used in these experiments, and when the XUV is isolated as well. Due to the exponential dependence of the tunneling ionization rate on Ip, the NIR data does not reflect the relative abundance of each atom or molecule in the detector. For O_2 and H_2O, Ip of 12.08 eV and 12.65 eV respectively [61], the probability they are ionized by the NIR field is order unity, as 120 TW/cm^2 is close to the saturation intensity for both species. For helium with an Ip of 24.59 eV, the tunneling ionization probability is 5 orders of magnitude less.

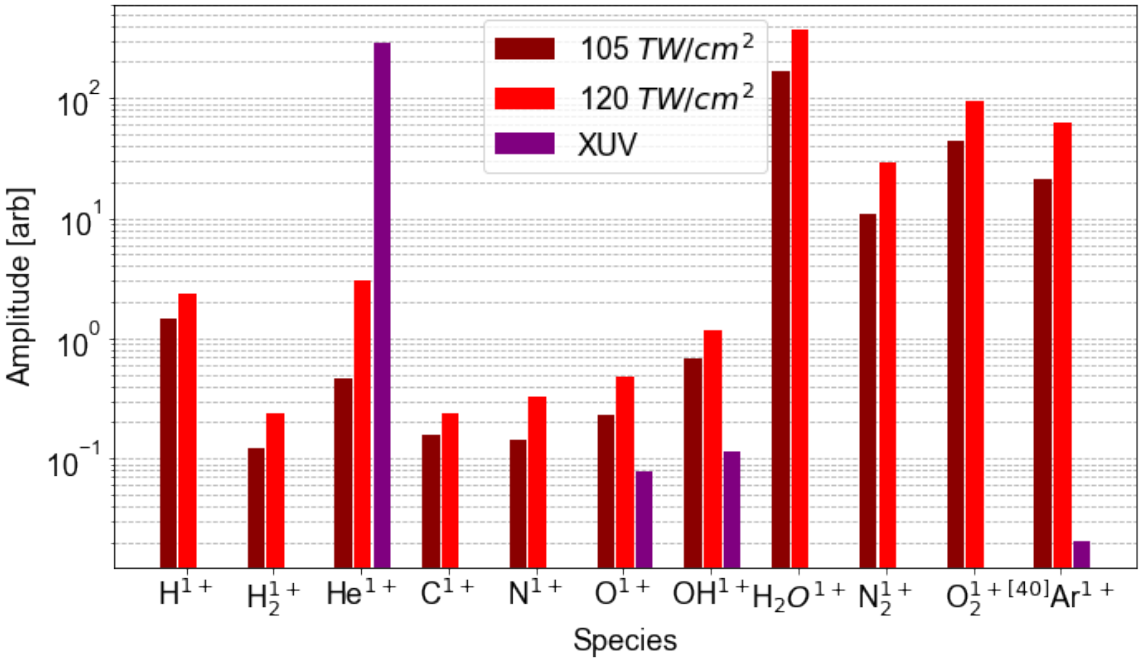

Figure 4.1: Relative abundance of ion species, helium experiments

Relative abundance of the prevalent ion species after ionization for three conditions: the XUV light in isolation or the NIR light alone for two different intensities, 105 and 120 TW/cm^2. The SFS condition is met for helium, where the majority of ionization is due to the XUV pulse. Based on this data, the presence of atmospheric contaminants will be limiting for photelectron studies with NIR intensities greater than 120 TW/cm^2.

As can be seen in Figure 4.1, the ionization of helium due to the XUV is the dominant signal up to 120 TW/cm^2 of NIR intensity at which point H_2O supersedes. The XUV ionizes 100x the amount of helium compared to the maximum NIR intensity, meeting the requirements of the SFS concept. For this reason, in the analysis of Section 4.3 the XUV can be treated as the only ionizing source for helium. Based on the relative ionization rates, the H_2O is at the part per million level of concentration in the gas sample, with other atmospheric contaminants at comparable concentrations. From comparisons of the ionization yield with and without the presence of the gas source, these contaminants are coming from either leaks in the gas delivery lines out of vacuum or are present in the gas cylinder itself. The gas delivery lines were baked repeatedly, a portion is placed in a liquid nitrogen bath, and an inline H_2O trap was installed. All these techniques were used to

remove as much of these contaminant species as possible, achieving the relative abundances shown here.

Having considered the ionization rates of each light source independently, it is worth considering if there are any changes when both fields are combined beyond a simple sum of their ionization rates. Figure 4.2 shows the ionization yield of helium as a function of delay between the XUV and NIR field. Panel (a) of Figure 4.2 has some interesting and unexpected features. Given the overlap of several harmonics with bound state transitions in helium, an asymmetry in the total yield versus delay is anticipated. For large negative delays, the NIR first interacts with the helium atoms, leaving them largely unperturbed, and then the XUV follows driving significant ionization. For large positive delays, the XUV first ionizes a fraction of the helium sample and the lower order harmonics populate excited states of some other fraction. In this situation, the NIR then interacts with a significant number of helium atoms in excited states, effectively helium atoms with significantly lower Ips, allowing for dramatic increases in the tunnel ionization rate. For context, the lowest energy dipole allowed transition from the ground state is to the 1s2p level which lies only 3.62 eV below the Ip of helium, and at this effective binding energy the saturation intensity for a 60 fs pulse is only 3.1 TW/cm^2 [63]. Given the nanosecond scale lifetimes of the helium excited states [102], it can be safely assumed that any atoms excited by the XUV will be ionized by the NIR light with 100% probability for delays up to 10^5 laser cycles. This anticipated behavior is born out by the rising ionization rate with increasing delay approaching 0, at which point the ionization rate should hold constant for effectively all positive delays. At 0 delay this two color ionization mechanism (XUV excitation then NIR tunneling) causes an increase of helium ionization of 1.5x to 2.0x.

In addition to the anticipated gross structure, an intensity dependent resonant like enhancement for positive delays is observed, see Figure 4.2(b). At this time, there is not a clear explanation for this enhancement, nor the logarithmically increasing delay at which it occurs. The delays measured, 10s of femtoseconds, are comparable to two timescales: the pulse duration of the NIR and the inverse of level splittings between some Rydberg levels (0.1 eV $\longrightarrow$ 41 fs). This suggests that this may be the result of wavepacket interference

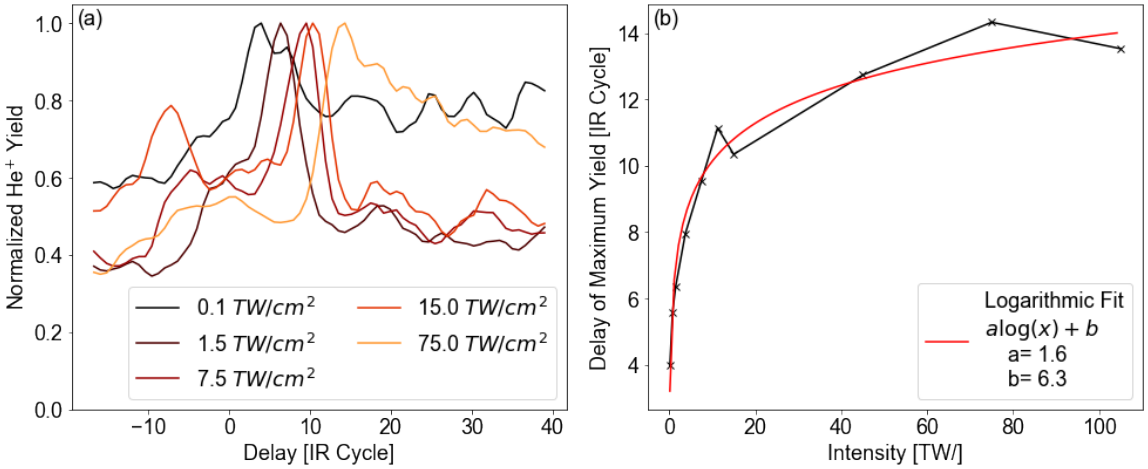

Figure 4.2: He^+ yield versus delay

(a) The ionization yield of helium normalized to the maximum of each lineshape. 0 Delay corresponds to the experimentally determined optimal overlap of the XUV and NIR fields based on the photoelectron data, see Section 2.4.4. The NIR pulse is 10 cycles in duration. Negative delays correspond to NIR leading the XUV field, and vice-versa for positive delays. (b) Increasing delay of the resonant like peak in helium ionization after Delay 0 as a function of NIR intensity.

among the Rydberg levels in helium [33, 42, 100], with the AC Stark shifting of atomic states leading to a delay dependent enhancement of the ionization rate. Further exploration of this type of physics is outside the scope of this dissertation, but could be an interesting avenue for future experiments. In regards to the results of these SFS experiments, it is not clear that this impacts the study of double ionization or the photoelectron spectra. No corresponding enhancement in the photoelectron yield is observed for large positive delays, though the anticipated asymmetry is present from tunneling ionization of excited states.

4.2.2 Double Ion Results

Observation of XUV seeded recollision was the primary goal of these SFS experiments. A delay dependent He^{2+} yield oscillating at a frequency commensurate to the NIR field would be the clearest experimental signature of this process. However, both XUV absorption by helium and the subsequent photoelectron recollision are low cross section events, making this measurement severely count limited. In addition, the possibility of there being other

two-color mechanisms for double ionization needs to be eliminated. In this experimental campaign, the count rate of helium double ions was too low to observe an oscillation of statistical significance or to conduct additional experiments eliminating other ionization mechanisms. What is observed is a significant enhancement in the double ionization of helium in the presence of both fields overlapped in time, see Figure 4.3. In addition, some quantitative arguments can be made to suggest that recollision is the sole mechanism capable of driving double ionization given experimental parameters.

Observing double ionization of helium can be a difficult exercise as the single ion of molecular hydrogen nominally has the same mass-to-charge ratios, 2 amu/e. The difference in mass-to-charge stems from the increased binding energy of helium leading to a splitting of 0.015 amu/e. As discussed in more detail in [59], the ion TOF is capable of resolving differences in mass-to-charge ratios of this order. However, separating these peaks requires greater statistical power, i.e. longer integration times, than a measurement against zero background, which can be limiting when attempting delay scans. In Figure 4.3, five minutes of integration at fixed delay was sufficient to resolve the hydrogen and helium peaks.

In Figure 4.3, two terms are defined that characterize the ability to resolve the He^{2+} and H_2^{1+} peaks. First is the separation which defines the upper bound on the resolving power to be able to distinguish the two species, this is defined as the quotient of the difference in mass-to-charge and the mass-to-charge of He^{2+}. Multiplying the numerator and denominator by a 2e reduces the definition to Equation 4.1.

$$\text{Separation} \equiv \frac{\Delta m}{m} = \frac{2m_{H_2} - m_{He}}{m_{He}} \tag{4.1}$$

The resolution is defined by the ratio between the sum of Half Width at Half Maximum for each species divided by the mass-to-charge ratio of He^{2+}.

$$\text{Resolution} \equiv \frac{\delta m}{m} = \frac{\text{HWHM}(H_2) + \text{HWHM}(He)}{\frac{m}{q}(He^{2+})} \tag{4.2}$$

With a resolution approximately half the magnitude of the separation, the ionization yield of He^{2+} can be accurately determined with little interference from the adjacent H_2^{1+} peak.

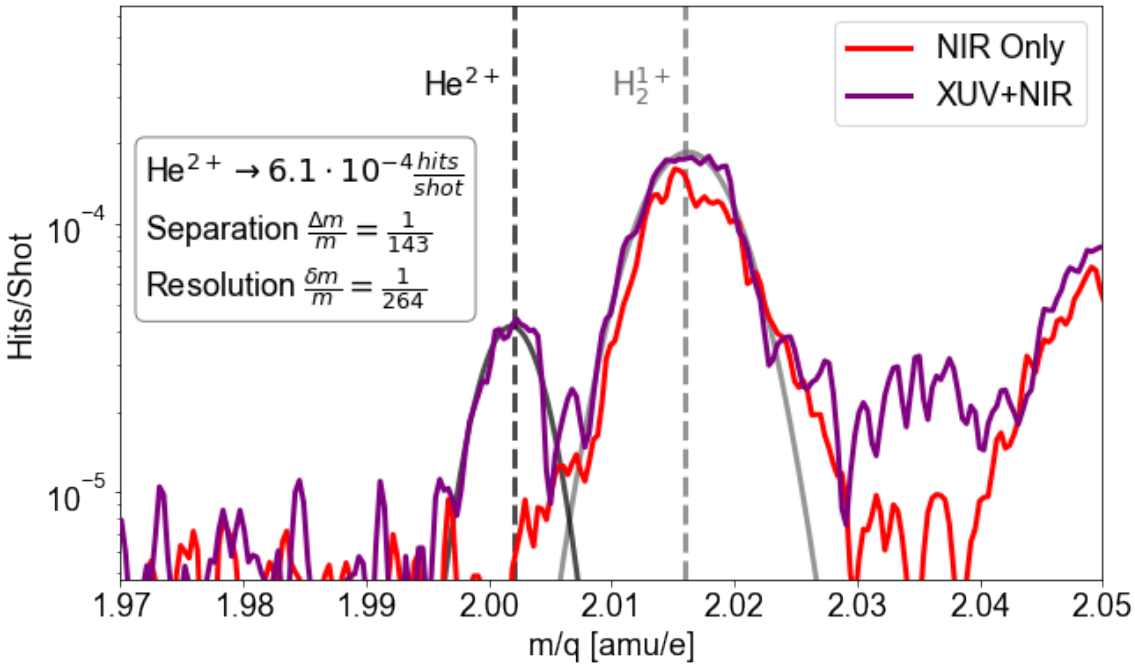

Figure 4.3: First observation of He^{2+} via a two-color XUV+NIR field

Hits per laser shot versus mass-to-charge ratio. The XUV only spectrum is not visible within the bounds of the ordinate. The disparity between the purple and red curves indicates a two-color enhancement of the helium double ionization rate. The separation and resolution are defined in equations 4.1 and 4.2 respectively. The additional peaks at mass-to-charge ratios of 2.035 and 2.05 are the result of ringing in the cabling between the detector and digitizer. The NIR intensity is 120 TW/cm^2 and the delay between it and the XUV field is set to 0.

The fact that double ionization is only observed when both the NIR and XUV fields are present is significant, the question though is if this the result of recollision. At an intensity of 120 TW/cm^2 the highest energy recolliding electron, 3.17 Up = 107.5 eV, is well past the binding potential of the helium ion, Ip = 54.42 eV [63]. So recollision is certainly a likely candidate. The trivial competing effect would be a sequential ionization process where one field ionizes helium and the other drives an additional ionization. This theory can be discarded due to the large increase of Ip between the neutral and singly ionized helium atom, 24.59 eV versus 54.42 eV [63]. The first excited state of singly ionized helium lies 40.81 eV above the ground state or 13.61 eV below the ionization threshold. The NIR is of insufficient intensity and the XUV of insufficient photon energy to drive measurable ionization from the

ions ground state, or even to access the first excited state of the ion. Note that the XUV field alone is of insufficient intensities to independently drive any nonlinear effects such as two-photon absorption. This argument against a sequential process is further strengthened by measurements at large positive/negative delays, greater than the pulse FWHM, where no He^{2+} yield is observed.

The other possibility would require a shake-up (shake-off) process, whereby the rapid ionization of one electron results in the excitation (ionization) of the second due to some overlap between the ground state wave function of the neutral atom and that of an excited (continuum) state in the ion. These were early candidates for the enhancement in double ionization in strong fields before the rescattering model was popularized [35]. However, little evidence has been found to suggest these processes actually occur in tunneling ionization of noble gas atoms [34], and should not occur for single photon ionization with such low energy XUV photons. By process of elimination it appears that XUV seeded recollision is the only candidate which can explain this enhancement. If so, then this is the first evidence that the SFS principle works and also the first demonstration of double ionization via a coherent XUV+NIR process.

4.3 Photoelectron Data

The photoelectron results present a more detailed picture of the interplay between the XUV and NIR fields in these SFS experiments. The added dimension to these data sets, electron kinetic energy, produces 2-dimensional spectrograms as opposed to 1-dimensional lineouts allowing for richer analysis. In addition, the majority of the signal in these spectrograms comes from those electrons that do not undergo recollision but are simply accelerated by the NIR field, or direct electrons. In principle the recollided electrons should still be observable given the dynamic range of the detector. Based on the semiclassical model there are three features which should distinguish the recollided electrons from the direct. First, recollided electrons can achieve much higher kinetic energies, recall the differing cutoff energies of 2Up and 10Up for the direct and recollided electrons. Second, the small cross section for

recollision occuring means there should be a dramatic decrease, or break, in the yield at a particular kinetic energy. Third, the majority of recollided electrons are born in approximately first tenth of an laser cycle following an extrema in the NIR electric field, whereas the maximum acceleration of the direct electrons occurs at extrema of the vector potential ($\pi/4$ out of phase with the electric field). This means that there should be an observable phase shift between the recollided electrons and the maximally accelerated direct electrons.

4.3.1 Experimental Results

Each spectrogram was collected in the following procedure. At the start of each day a particular wedge insertion distance was assigned as delay 0, based on the procedure for finding optimal temporal overlap in Section 2.4.4. This assignment was accurate to within a few laser cycles of the NIR field. Each delay scan consisted of 36 steps centered on delay 0, with step size of 8 microns of wedge insertion corresponding to added delay of approximately a seventh of an laser cycle. As such, each scan consists of 5 laser cycles. 10,000 laser shots were collected for each delay step and each scan required 6 minutes to complete. The average counting rate was at or in excess of a hit per shot for all intensities. At each intensity, an additional spectrum was collected for the NIR alone to calibrate the intensity and characterize the background photoelectron yield in each experiment not driven by XUV ionization. A spectrum for XUV alone was also collected and used to calibrate the eTOF conversion each day. Figures 4.4-4.7 show the results across four orders of magnitude of NIR intensity. Additional spectrograms were collected at 7.5 TW/cm^2 and at intervals of 15 TW/cm^2 from 15 TW/cm^2 to 120 TW/cm^2. These spectrograms are included in the discussions and figures of Sections 4.3.2 and 4.3.4.

Each of these figures contains 5 panels similar in format to Figure 3.12. (a) is the spectrogram with the upper bound on kinetic energy set to where the average yield across all delays is reduced to some fraction of its maximum. This is a 4 order of magnitude reduction for the two lower intensities, Figures 4.4 and 4.5, and 5 orders of magnitude for the two larger intensities, Figures 4.6 and 4.7. The color scale in each spectrogram is normalized to the brightest pixel, so comparisons in yield between Figures 4.4-4.7 is not

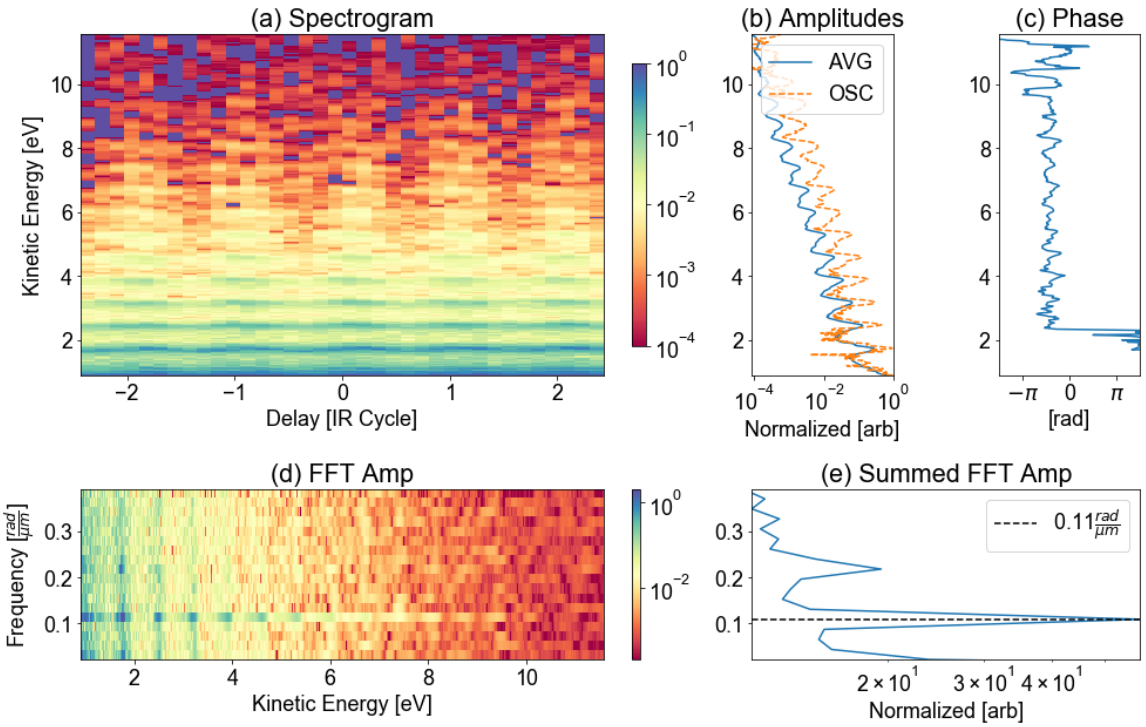

Figure 4.4: Photoelectron spectrogram, helium target, <1 TW/cm^2

possible. (b) displays two lineouts, first the electron kinetic energy versus average yield (AVG) in blue and the amplitude of the brightest Fourier component, OSC, in orange. (c) plots the kinetic energy versus phase of the Fourier component in radians. (d) is a heat map displaying the amplitude of each Fourier component as a function of electron energy. (e) shows the amplitude of each Fourier component, summed over all electron energies, with the brightest identified by a dashed line. Frequencies are provided in radians per micron of delay wedge insertion.

A few features of these spectrograms elicit discucssion. First, at lower intensities the individual harmonics are visible with NIR producing sidebands such as in a RABBITT or PROOF measurement. Increasing intensity leads to the production of additional sidebands given by a perturbative scaling of I^n, where n is the number of NIR photons separating the harmonic and sideband. For intensities greater than 10 TW/cm^2, individual harmonics and sidebands can no longer be distinguished and data in panels (a-d) are smooth along

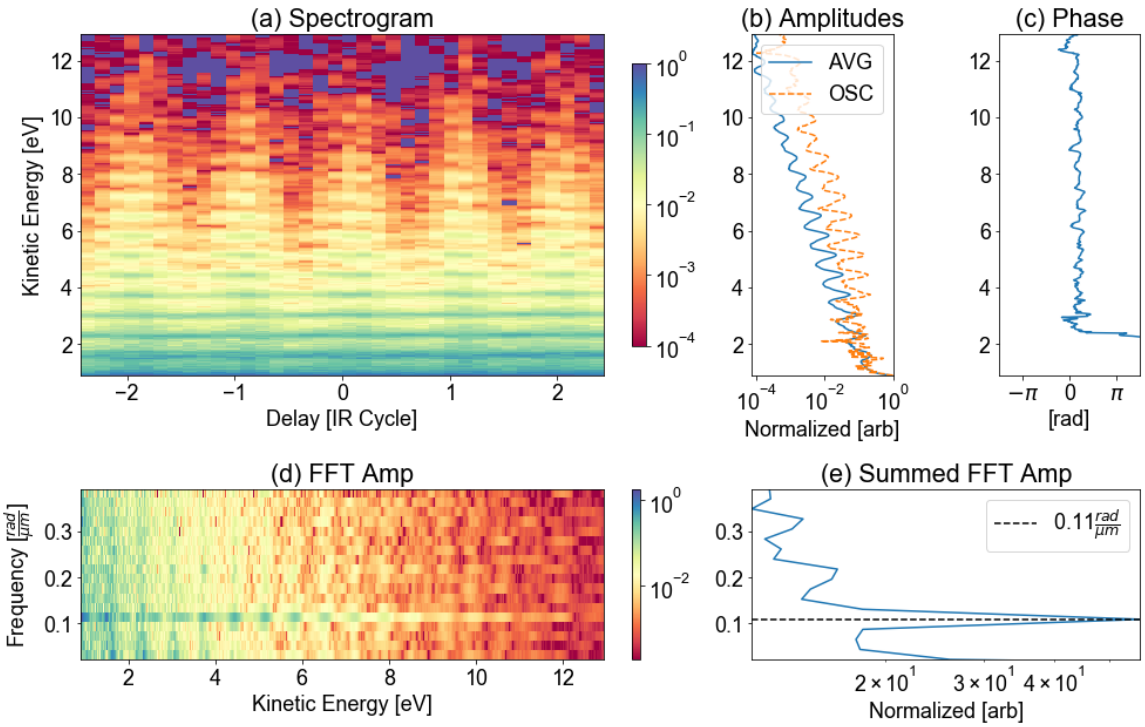

Figure 4.5: Photoelectron spectrogram, helium target, 2 TW/cm^2

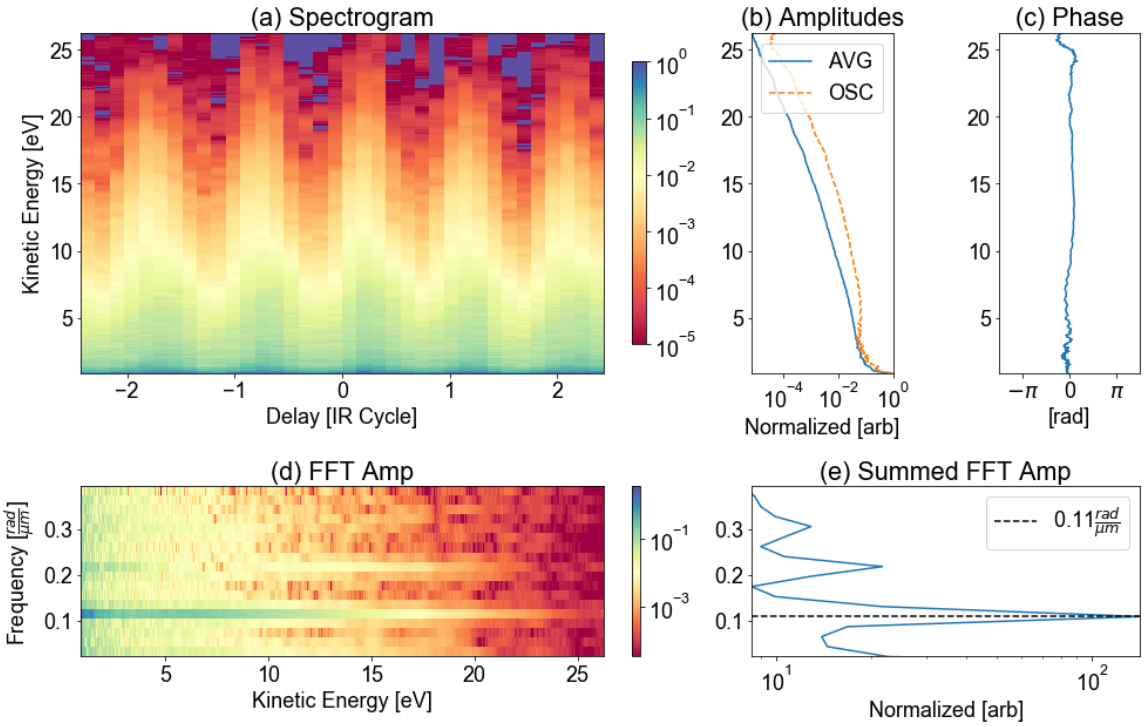

Figure 4.6: Photoelectron spectrogram, helium target, 15 TW/cm^2

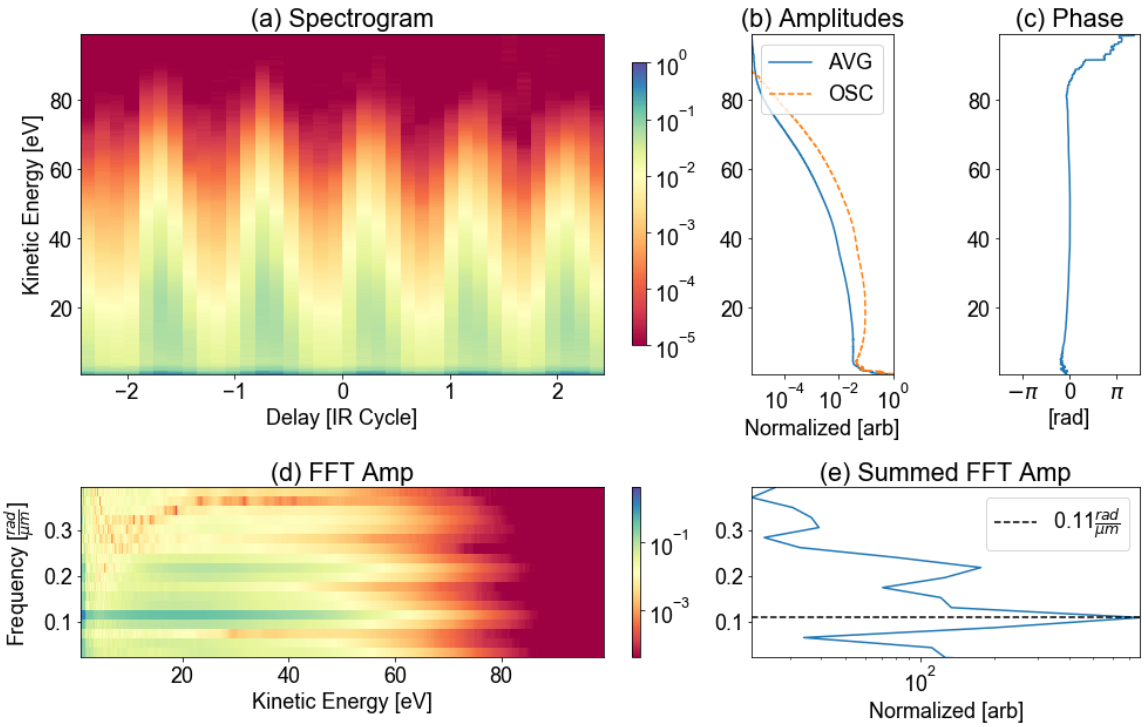

Figure 4.7: Photoelectron spectrogram, helium target, 120 TW/cm^2

the kinetic energy axis. Second, for all intensities the dominant Fourier component lies at 0.11±0.01 $\frac{rad}{\mu m}$ which corresponds to an additional 1.87±0.17 μm of optical path difference per cycle, recall the NIR wavelength of 1.74 μm. This oscillation at once per NIR cycle, here dubbed the 1ω oscillation, is anticipated for an APT with a single pulse per cycle. With increasing intensity, additional peaks corresponding to two and three oscillations per cycle appear and strengthen. Third, the phase of the 1ω oscillation is flat for all kinetic energies regardless of intensity. For lower intensities, Figures 4.4 and 4.5, there is a pi-phase jump around 2 eV which is an artifact of the unwrapping procedure at a point between harmonic orders where the oscillation phase is ill-defined.

This lack of significant chirp across kinetic energies stands in stark contrast to the previous generation of SFS experiments carried out by Dietrich Kieswetter [59]. These experiments at shorter NIR wavelengths and using a broadband XUV pulse (photon energies 15-50 eV) exhibited significant phase excursions in excess of 1 radian. Typical spectrograms

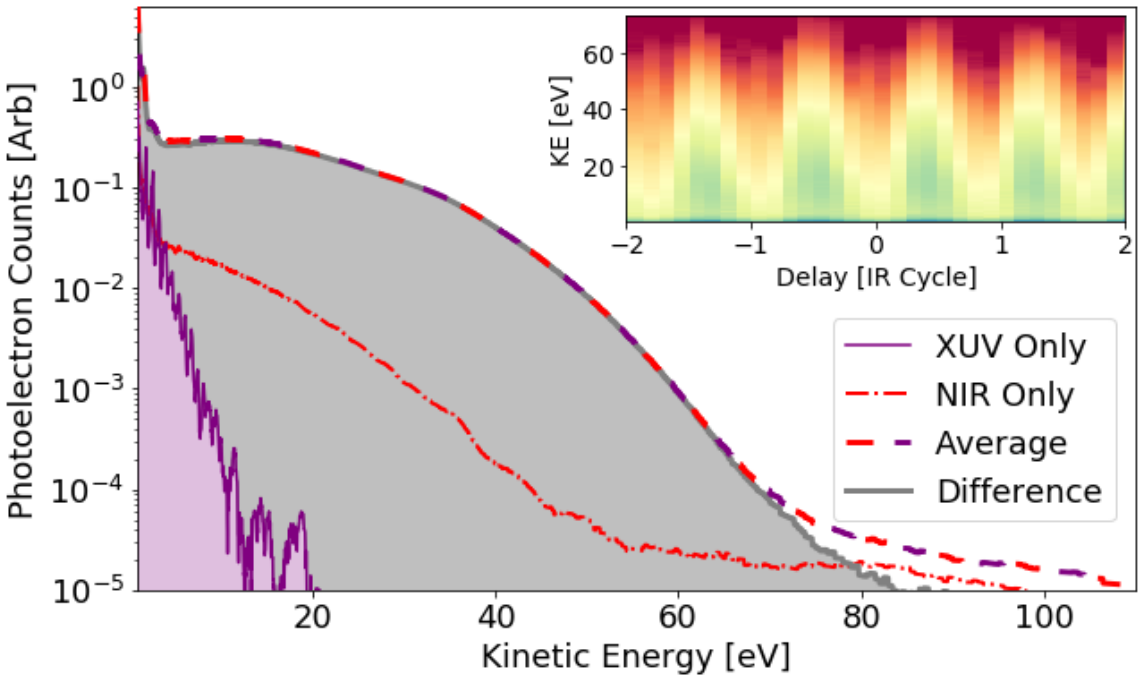

Figure 4.8: Lineouts from spectrogram, helium target, 90 TW/cm^2

Here the average lineout represents the average across delay steps in the spectrogram shown in the inset. The difference is between the average and the NIR only spectrum. Comparing the area of the grey curve, the difference spectrum, and the XUV Only reveals a large enhancement in the photoelectron yield from the two-color XUV+NIR interaction.

could be separated into two regions, one with a strong negative chirp from 0 to ∼15 eV of electron kinetic energy, and the other with weak positive chirp for large kinetic energies. The result was that only the very lowest and very highest kinetic energy electrons oscillated in phase in any spectrogram. TDSE simulations suggested the positive chirp at higher energies was correlated with the chirp of the APT, similar to a streaking type measurement. The low energy region were ascribed to a more complex interaction of the photoelectrons in the NIR field near the ionization threshold. The lack of any phase evolution in these latest experiments suggests the chirp of the XUV pulse is insignificant, and that the role of NIR has fundamentally changed.

Additional information is gained by comparing the spectrograms to the photoelectron yield from the NIR or XUV in isolation. Figure 4.8 shows 4 spectra: the XUV only photoelectron yield, the NIR only, the average for all delays of the spectrogram (inset), and

the difference between this spectrogram average and the NIR only spectrum. Here the difference spectrum is useful as the contributions from the NIR ionization mechanisms are removed. The first thing this difference spectrum reveals is that any signal past 70 eV is from recollision induced by the NIR only in isolation, and not the XUV seeded process we hoped to observe. The difference spectrum also shows a substantial enhancement of the total photoelectron yield, about an order of magnitude larger than an incoherent sum of the XUV Only and NIR Only spectra. The ion yield data showed that the helium ionization rate doubles in the presence of both the NIR and XUV light, however the increase here in the photoelectron signal is factor of 35x. From the previous generation of experiments a similar enhancement was observed, and had been attributed to NIR field focusing the photoelectron distribution along the polarization axis. This focusing combined with the finite collection angle, 10°, of the eTOF creates an intensity dependent enhancement in total photoelectron yield, though the magnitude of the enhancement is substantially larger than in these previous SFS experiments.

4.3.2 Intensity Scaling

Given the linear scaling of many features of strong field ionization with the Ponderomotive Energy (Up) of the NIR field, it is worth analyzing these spectrograms for analogous scalings with Up. Figure 4.9, plots the difference spectra across one and half orders of magnitudes of NIR intensity, corresponding to range of Up from 2.2 to 32.4 eV. Recall that Up scales linearly with intensity.

There are three features of these photoelectron distributions that appear to scale linearly with intensity, or Up. First, the total photoelectron curve as measured by the area under the curve. This can be quantified by a total *enhancement* defined as the area under the difference spectrum divided by that of the XUV alone. The enhancement reflects the degree to which the NIR field is focusing the XUV along the polarization axis, and correspondingly the TOF axis. In addition, this will include the effects of increased helium single ionization

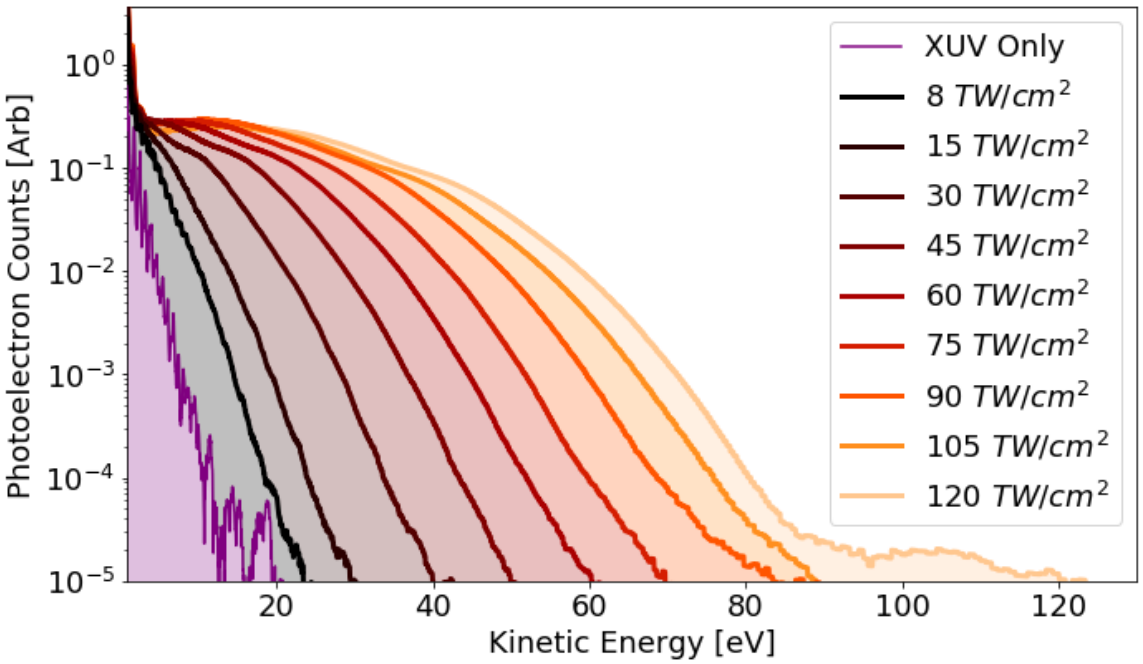

Figure 4.9: 2-Color photoelectron yields for various NIR intensities, helium target

Each curve is the difference between the spectrogram average and the NIR only spectra. These can be directly compared for relative increases in yield.

in the presence of the NIR and XUV fields as discussed in Section 4.2.1.

$$\text{Enhancement} \equiv \frac{\int S(NIR+XUV) - S(NIR)dE}{\int S(XUV)dE} \tag{4.3}$$

Where *S(NIR+HHG)* is the spectrogram average, *S(NIR)* is the NIR only spectrum, and S(HHG) is the XUV only spectrum. Second, there is a distinct *cutoff* at a particular kinetic energy at which the photoelectron yield falls below the detection threshold, here assumed to be 5 orders of magnitude below the maximum value in the spectrogram average. Assuming the SFS concept works, this should correspond to the 2Up cutoff from the "Simpleman's Theory" which is the maximum energy the NIR accelerates an electron without recollision.

$$\text{Cutoff} \equiv KE : \frac{\text{MAX}[S(NIR+XUV)]}{10^5} \tag{4.4}$$

Third, is the *Center of Mass*, CoM, of the photoelectron distribution. In a typical attosecond streaking spectrogram this quantity should be 0 as the photoelectrons are accelerated and

decelerated with equal magnitude as the delay between the XUV and NIR fields changes. However, these spectra clearly have a positive shift to the center of mass that scales with increasing intensity.

$$\text{CoM} \equiv \frac{\int KE \times (S(NIR+XUV) - S(NIR))dE}{\int S(NIR+XUV) - S(NIR)dE} \tag{4.5}$$

Finally given the exponential scaling of the tunneling ionization rate due to the NIR field, at some NIR intensity the signal of interest in these SFS experiments should become unobservable against this competing process. As stated previously, being below this threshold is an essential component of conducting the SFS experiments and the ion data in Figure 4.1 suggested we were in this regime. A final quantity, the *Signal-to-ATI*, quantifies the ratio between the SFS signal we are interested relative to the amount of ATI from the NIR field.

$$\text{Signal-to-ATI} \equiv \frac{\int S(NIR+XUV) - S(NIR)dE}{\int S(NIR)dE} \tag{4.6}$$

Figure 4.10 plots these three features, *enhancement*; *cutoff*; and *CoM* along with the *Signal-to-ATI* which quantifies the quality of the SFS measurement.

The slope of each feature in Figure 4.10(a-c) is given with respect to the Up. For the *enhancement* in (a) there is not a clear reason why it should scale with the Up in units of eV. The linear scaling with ponderomotive energy may be better correlated with an intensity dependence of the focusing of the photoelectron distribution by the NIR field. In (b), the scaling of the cutoff at almost exactly 2Up is in excellent agreement with the "Simpleman's Theory". This is the strongest experimental evidence that the SFS method can accurately reproduce the physics of strong field ionization. Within the "Simpleman's Theory" there is no explicit dependence of the *CoM* with Up, such as the factor of Up/2 seen here, however it is anticipated to increase with Up. Panel (d) shows that the SFS condition is met for all intensities as the majority of photoelectrons produced are coming from the XUV ionization mechanism. At the largest intensities the significant fraction of counts (∼25%) from ATI does create a noisy background to make the measurement against, however the Fourier decomposition allows for effective analysis to still be done as the tunneling electrons by the

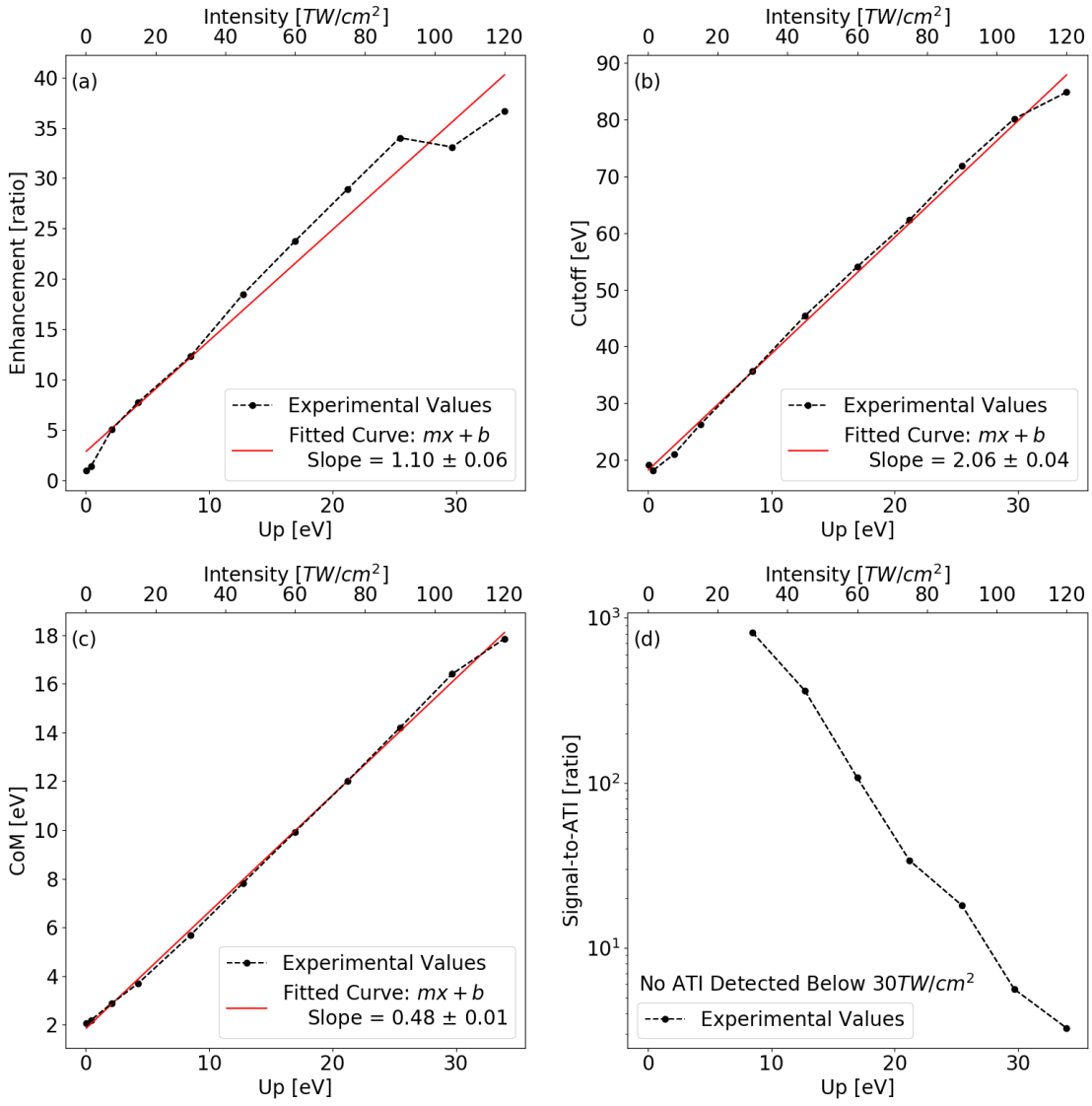

Figure 4.10: SFS feature scaling in helium photoelectrons

See Equations 4.3 - 4.6 for definitions of the ordinate in each subplot.

NIR field are a constant signal for all delays.

4.3.3 SFA Simulations

As discussed in the beginning of Section 4.3, key signatures of electron recollision in a spectrogram would be weak yield at large kinetic energies with some phase offset from the maximum of the *simplman* electrons. Thus far this has not been observed in any of

these spectrograms. Comparisons of the NIR only spectra with the spectrogram averages, such as in Figure 4.8, suggest that past the 2Up cutoff of the spectrogram average the recollided electrons from the action of NIR field in isolation dominate the signal. This is likely due to the increased electron collision cross-section for the larger contaminant species that are ionized by the NIR field relative to helium. However, there may be other signatures of recollision unique to these SFS experiments that would not be seen in a single color experiment.

To explore this possibility, simulations were done within the Strong Field Approximation (SFA) of the NIR interaction with photoelectrons ionized by the XUV field [78]. Using Equation 1.5 and the phase terms defined in Equations 1.7-1.9, the simulations assumed a 10-cycle NIR pulse and an XUV APT with a transform limited 500 as FWHM pulse duration. For further simplicity, the dipole matrix element for XUV absorption by the helium atom was assumed constant across the bandwidth of the XUV harmonics. One weakness of these SFA simulations is the lack of any mechanism for recollision within this formalism, as it ignores the atomic potential after ionization. So the strategy will be to look for discrepancies between the experiments and simulations that are suggestive of recollision. Figures 4.11-4.13 display the results of these simulations.

These simulations reproduce the primary features of the experimental spectrograms. The transition from discrete harmonics to continuous spectra, the linearly increasing cutoff with intensity, and the flat phase structure. The Fourier decomposition reveals many more harmonics of the 1ω oscillation than observed in the experiments. This can be attributed to the higher delay resolution of the simulations, in addition to the lack of interferometric instabilities and integration across the spatial variation of phase across the NIR wave front. The most significant distinction between the simulations and experiments occurs at large intensities in the behavior of low kinetic energies for delays where the electron cutoff is maximized. In Figure 4.13, there is no photoelectron yield below 20 eV for delays with the largest cutoff. Compare this to Figure 4.7 where the yield for all photoelectron energies is maximized at these delays. One simple explanation for this discrepancy is the effect of focal volume averaging. In the simulation the entirety of helium atoms ionized by the XUV field

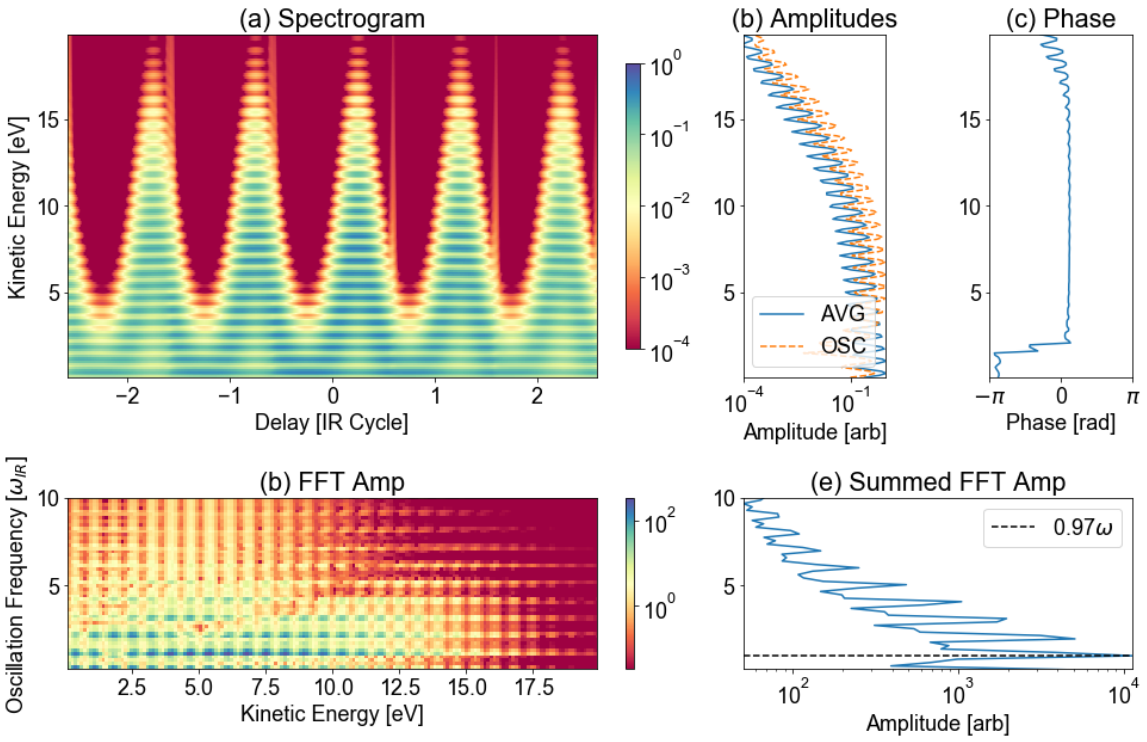

Figure 4.11: SFA photoelectron spectrogram, helium target, 2 TW/cm^2

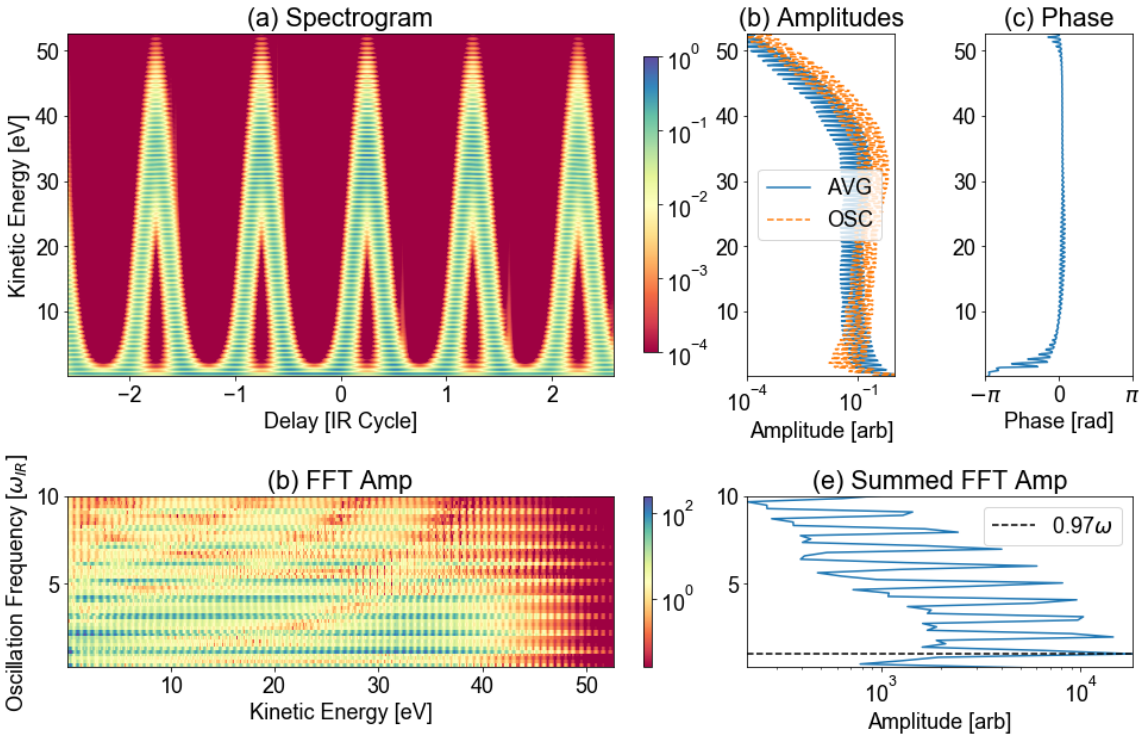

Figure 4.12: SFA photoelectron spectrogram, helium target, 15 TW/cm^2

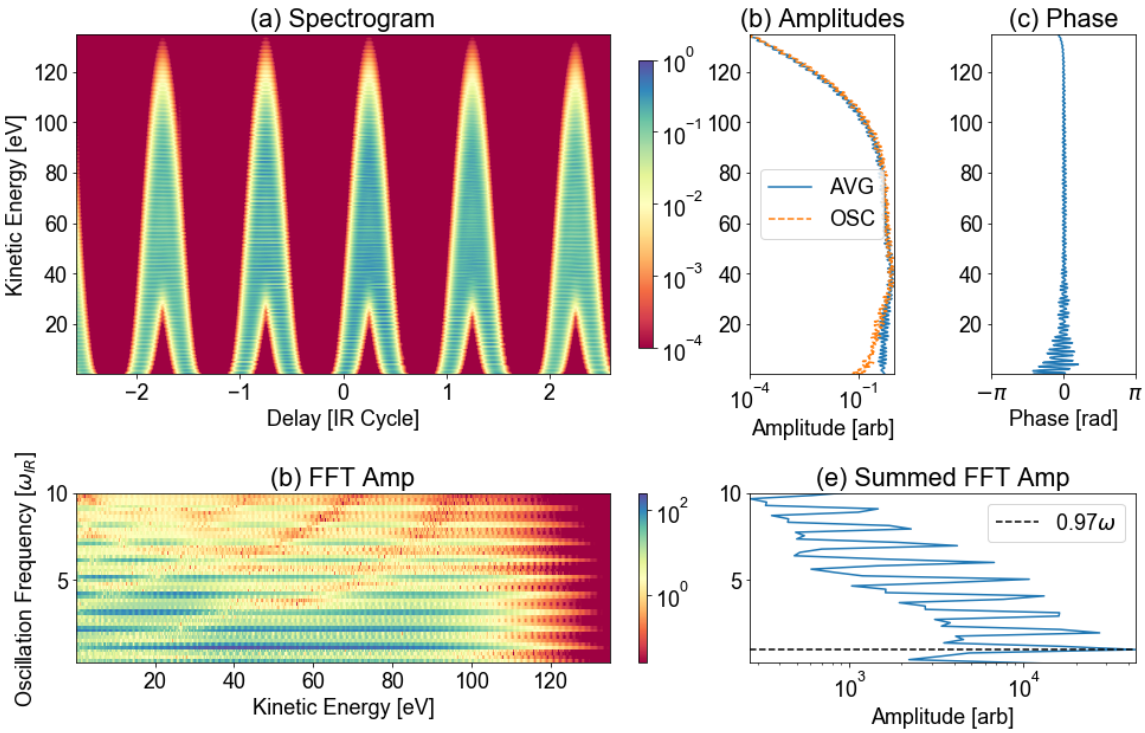

Figure 4.13: SFA photoelectron spectrogram, helium target, 120 TW/cm^2

experience an identical NIR intensity. In the experiment, the XUV waist is some fraction of the NIR waist and so the photoelectrons interact with a distribution of intensities of the NIR field. However, further investigation suggests there is some additional process occurring in the experiments not seen in these simulations.

4.3.4 Low Energy Feature

Figure 4.14 displays panels (a-c) of Figure 4.7 with a logarithmic ordinate so as to emphasize the dynamics of the lowest energy electrons. There is a discernible feature near 1.6 eV of kinetic energy oscillating in phase with the highest energy electrons. Even when accounting for focal volume averaging there is no reason to expect this narrow feature to be the composed of direct electrons. Looking at the lineouts in panel (b), this low energy feature account for a significant fraction of the total photoelectron yield. This feature is not present at the lowest intensities, 15 TW/cm^2 or below. In Figure 4.15(a), the difference spectra

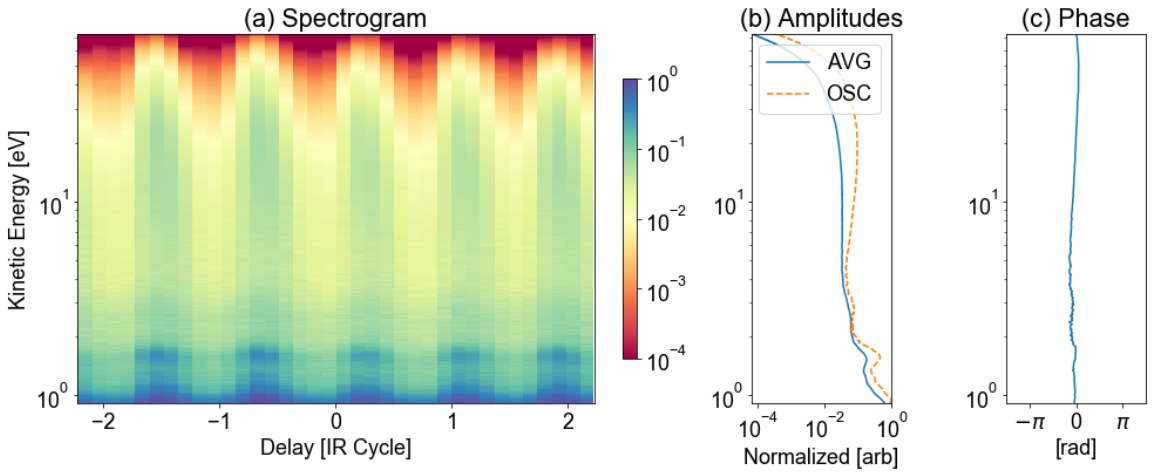

Figure 4.14: Photoelectron spectrogram, helium target, 120 TW/cm^2, semi-log scale

A significant peak in photoelectron yield occurs within a few eV above the ionization threshold in helium.

below 2 eV, spectrogram average minus NIR only, is plotted for increasing NIR intensities. At 30 TW/cm^2 this feature appears as little more than a change in slope at 1.5 eV, however, a narrow peak evolves with increasing intensity slowly shifting toward higher kinetic energy. At 120TW/cm^2 the peak is centered at 1.6 eV. Panel (b) shows the fraction of the total photolectron yield, for all kinetic energies, contained below 2 eV, showing approximately 10 - 20% of the total yield. Considering the factor of three increase in the enhancement from Figure 4.10(a), the real number of photoelectrons contained in the feature also increase with intensity.

This feature observed at low energies is unanticipated but reminiscent of the Low Energy Structure (LES) observed in single color NIR experiments at large intensities [9][110]. A similar feature at low energies is observed in neon, see Appendix C. The LES is attributed to electrons born with little to no kinetic energy that undergo soft recollisions with the atomic core. The LES is characterized by a narrow peak in the photoelectron yield as low kinetic energies, <10 eV, that can contains as much as half of the total photoelectron yield [9]. Zhang et al. provide an analytical expression for the peak position of the LES as a function of pulse duration provided in [110]. For a 10 cycle NIR pulse and 34 eV of Up, corresponding to 120 TW/cm^2 at a wavelength of 1.74 μm, the peak of the LES should be at 1.86 eV. This

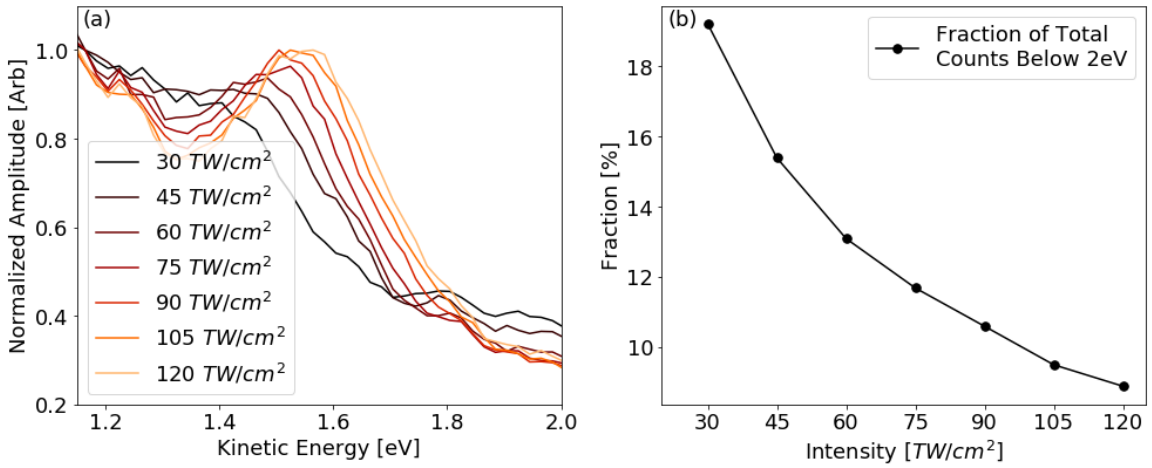

Figure 4.15: Low energy feature scaling in helium

(a) difference spectra normalized to the maximum photoelectron amplitude within each spectra. (b) the fraction of the total photolectron signal in the difference spectra contained below 2 eV.

is within 16% of the experimental value of 1.6 eV, which is within the typical error reported in intensity calibrations using the ATI spectra, 20%. A definitive assignment of this feature as an LES is difficult at this time. One outstanding question regards the lack of phase shift between this feature and the rest of the spectra. The maximum acceleration of the direct electrons occurs at ionization times near the zeros of the electric field, corresponding to the extrema of the vector potential. However, the electrons responsible for the LES are born at the maxima of the electric field or zeros of the vector potential [55]. This suggests that a phase shift of $\pi/2$ should exist between the direct electrons and the LES. This discrepancy requires some explanation before a positive assignment can be made. One possibility is the difference in the ionization process, tunneling versus single photon absorption, as the dipole matrix element for single photon absorption undergoes a significant phase shift of order radians near threshold [60, 66].

4.4 Atomic Resonances

In Section 4.2.1 it was suggested that the increase in the single ionization rate of helium was due to electrons promoted to excited states by the XUV and subsequently tunnel

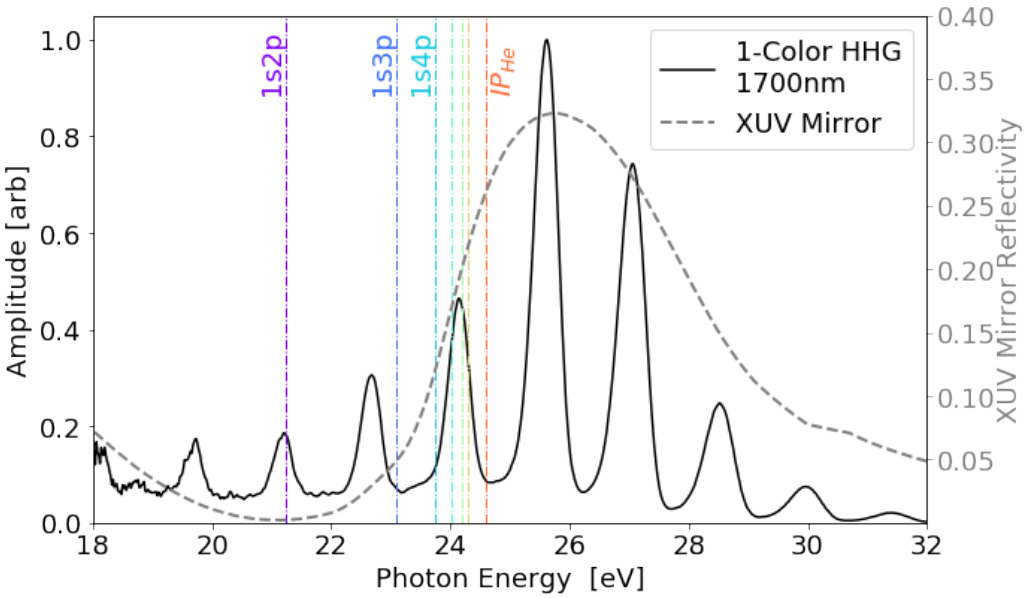

Figure 4.16: One color HHG spectrum driven at 1.7μm

Harmonic 29 at 21.2 eV strongly couples the helium ground state to the 1s2p excited state. Harmonic 33 at 24.1 eV couples the ground state to the 1s5p, 1s6p, and 1s7p excited states.

ionized by the NIR field. The strongest evidence for this mechanism comes from preliminary experiments that were conducted with an XUV APT produced by single color HHG at a laser wavelength of 1.7 μm. The corresponding spectrum is shown in 4.16. At a driving wavelength of 1.7 μm, the first excited state of helium is coupled to the ground state by the 29^{th} harmonic with photon energy 21.2 eV. Given that the oscillator strength of the $1s^2$ to 1s2p transition is 2 orders of magnitude larger than the $1s^2$ to 1s5p or higher lying transitions, it is safe to assume the vast majority of excited electrons occupy the 1s2p state. This same assumption holds true in the case of 2-color HHG at 1.74 μm as shown in Figure 3.10.

Looking at the photoelectron yield over a coarse scan of the XUV and NIR delay, for which delay steps are greater than an laser cycle, a large asymmetry is observed between large positive and negative delays. See Figure 4.17. This asymmetry in photoelectron yield is similar to the coarse features in the single ion yield versus delay previously discussed. When the NIR arrives first, large negative delays, the XUV simply ionizes the helium producing a

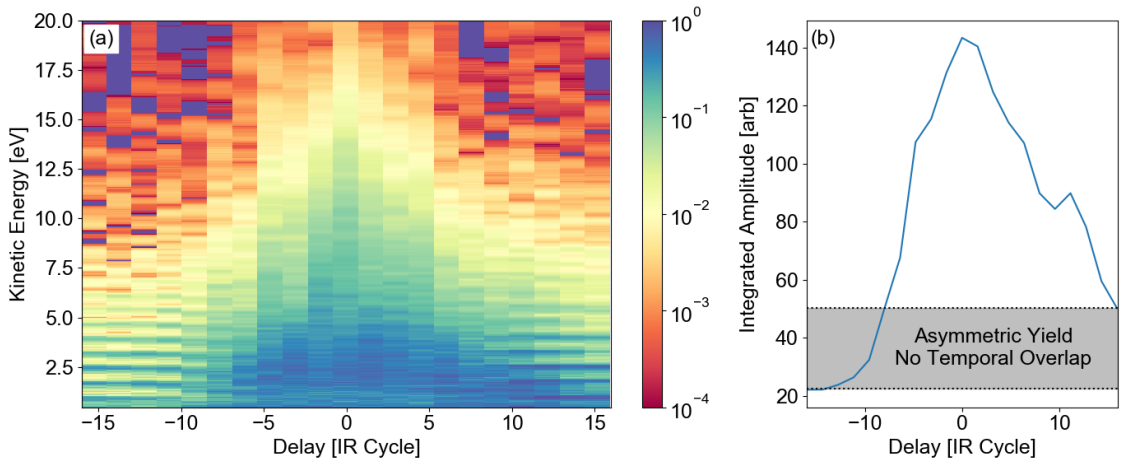

Figure 4.17: Asymmetric photoelectron yield for large delays

(a) coarse delay scan observing photoelectron yield over a range of approximately three NIR pulse widths. (b) shows the total photoelectron yield as a function of delay. The grey box highlights the difference in yield for positive and negative delays large enough that there is little overlap between the XUV and NIR fields.

spectrum indistinguishable from one with no NIR field at all. Near 0 delay the enhancement due to the focusing of the photoelectron distribution results in a dramatic increase in yield across all energies and it becomes difficult to distinguish between harmonic orders. At large positive delays, where the XUV interacts first then the NIR, the photoelectron yield does not return to the amount at negative delays and sidebands are observed between harmonic orders. Figure 4.18 compares the phototelectron yield of the NIR field alone, the XUV yield alone, and the two combined at a delay of +30 laser cycles.

In Figure 4.18 sidebands are observed between the odd ordered harmonic peaks, and the harmonics themselves have an increased yield compared to an incoherent sum of the XUV and NIR only spectra. Knowing that the probability of driving a one photon transition in the continuum is dependent on the instantaneous intensity at the moment of ionization, the presence of these sidebands cannot be the result of continuum-continuum transitions such as in a RABBITT measurement. The simplest explanation for both the presence of "sidebands" and the enhancement of peaks at odd ordered harmonics is the presence of increased ATI due to ionization from excited states, i.e. decreased binding energies.

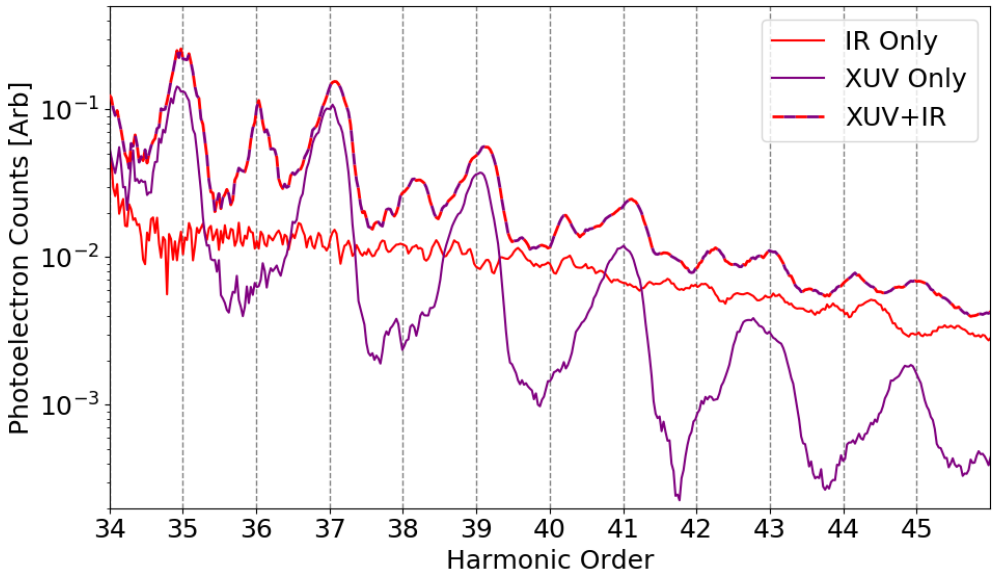

Figure 4.18: Photoelectron enhancement away from temporal overlap

Delay is equal to +30 cycles of the NIR field. The enhanced yield at harmonic orders and the appearance of sidebands is attributed to the increased probability of ATI from the NIR field in the presence of electrons promoted to excited states.

As the XUV harmonics and ATI orders are commensurate in energy, these two ionization mechanisms result in overlapping photoelectron spectra. Previous experiments have actually observed quantum beats between these two ionization mechanisms at similar delay scales as those used in this coarse scan [82], where the frequency of oscillation confirmed the presence of bound states in the interfering pathways.

4.5 Conclusions

The ultimate goal of the experiments presented in this chapter was the observation of recollision events within the SFS scheme. At this time, none of the results can be definitively determined to be the result of recollision. However, the case has been made that the observation of enhanced double ionization of helium is unlikely to result from any other mechanism. In addition, the low energy feature observed in the photoelectron spectrograms is possibly the result of soft recollision event commonly referred to as the LES, when measured in NIR

only experiments. What is encouraging is the reproduction of the essential features of the "Simpleman's Theory", suggesting that these experiments are fully functioning examples of an SFS. Future improvements on these experiments are likely to result in clearer observations of recollision dynamics. Reducing the contaminant species in the gas delivery lines is needed to reveal the electrons undergoing hard recollision, those measured to have between 2 and 10 Up of kinetic energy, in the photoelectron spectrograms. Increases in the XUV yield from HHG or helium gas density in the interaction region are required to attain a sufficient counting rate of double ionization events to conduct sub-cycle delay scans. Additional experiments with new polarization schemes of the XUV and NIR fields, such as using elliptically polarized NIR fields, should be pursued due to the strong dependence of recollision on field ellipticity.

Chapter 5
Argon Experiments

"Now I'm a scientific expert; that means I know nothing about absolutely everything."

— Arthur C. Clarke, 2001: A Space Odyssey

5.1 Overview

A particular challenge of SFS experiments in helium is its small cross-sections for both single photon absorption of XUV light and electron scattering. Switching to larger atomic targets such as argon, allows for dramatic increases in the number of events per laser shot for equivalent experimental conditions. In this chapter, experiments are conducted in argon using the same XUV comb as the previous chapter (with photon energies centered at 26.3 eV). In principle this does not meet the criteria laid out in Section 1.3 for a true SFS experiment, where the XUV energy distribution should be near the ionization threshold. However, a key feature of the photoelectron spectra suggest that given sufficient Up from the NIR field the experiments enter the SFS regime. In addition, an observed oscillation of the Ar^{2+} yield suggests recollision still occurs with larger initial kinetic energies.

5.1.1 Harmonic Spectrum

Figure 5.1 displays the XUV spectrum against the autoionizing states of argon, made up of electronic bound states embedded in the continuum. These states involve promoting the 3s electron to an excited state, as opposed to a 3p electron in the valence shell, and thus lie above the ionization threshold of argon. These bound states have short lifetimes of order 100 fs and result in ionization when the state relaxes, hence autoionizing [97]. This

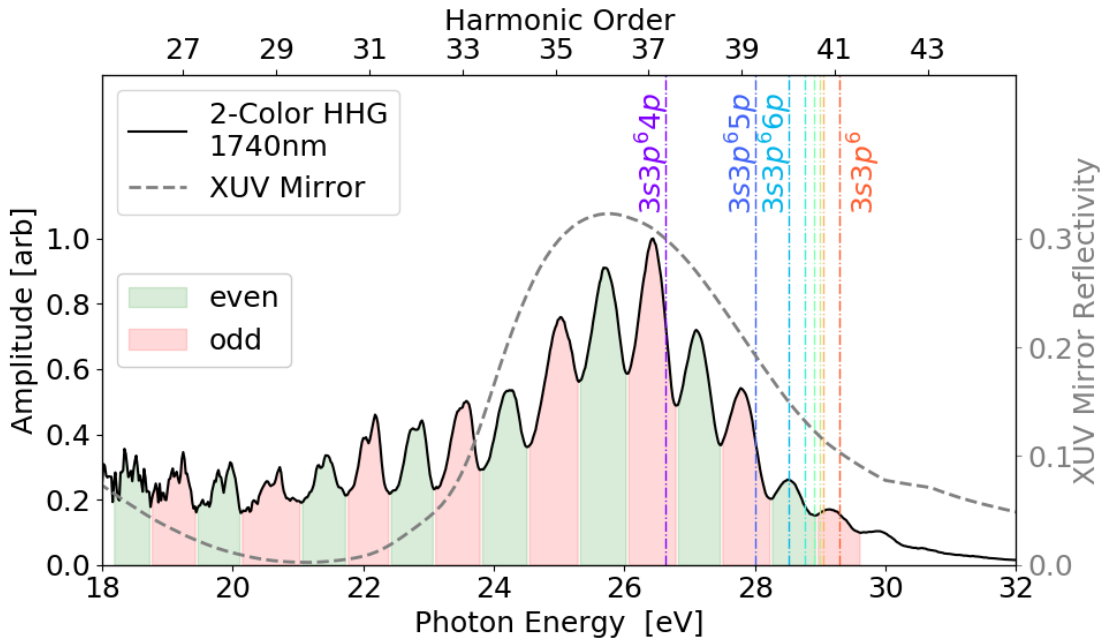

Figure 5.1: XUV spectrum highlighting resonances in the argon continuum Argon energy levels are retrieved from [63].

creates an additional path to ionization beyond trivial single photon ionization, and these pathways interfere to create a Fano resonance [32]. Studying the phase structure of these Fano resonances in argon is a prototypical attosecond experiment [62, 106]. For the role of these Fano resonances in an SFS experiment are unclear. Recent work has shown that the Fano resonance requires a finite amount of time to fully form and can be terminated by the introduction of an ionizing NIR field after XUV excitation [54]. In practice, it may very well be that these autoioninizing states are irrelevant for SFS type experiments with significant NIR intensities. What is certainly significant to these experiments is the large difference between the carrier photon energy of the XUV field and the Ip of argon.

5.1.2 My Contributions

I was responsible for collecting and analyzing all of the data presented in this chapter. I developed the software to run the SFA simulations of the photoelectron data. Qiaoyi Liu

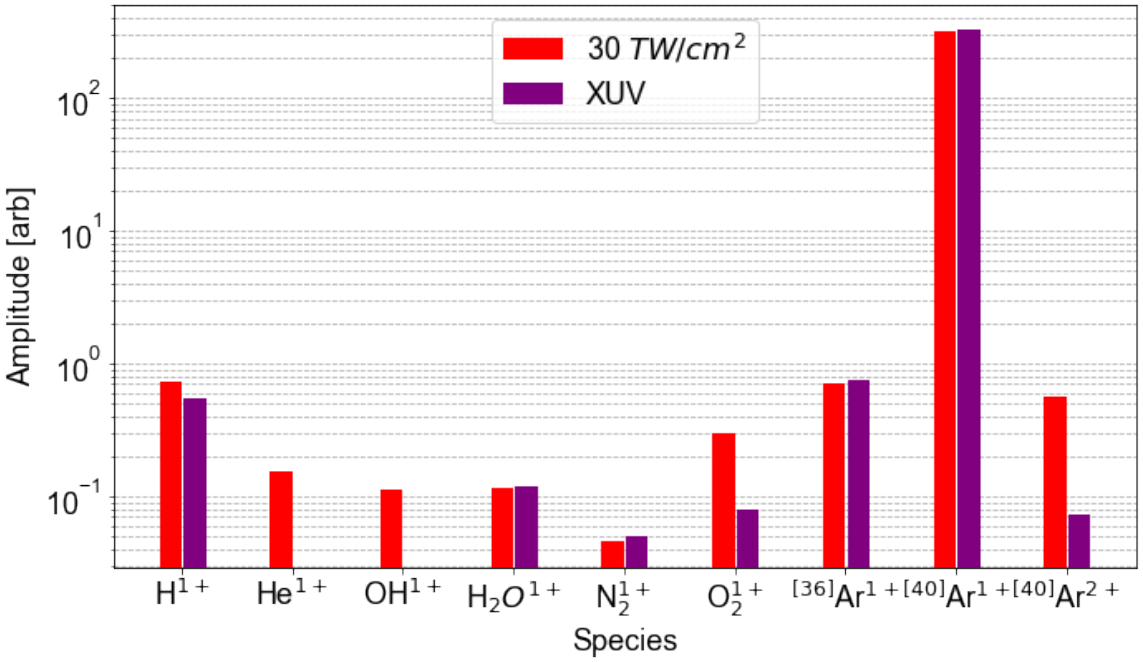

Figure 5.2: Relative abundance of ion species, argon experiments

Relative abundance of the prevalent ion species after ionization for two conditions: the XUV light in isolation or the NIR light alone at an intensity of 30 TW/cm^2. These experiments in argon are limited by the increased tunneling ionization rate due to the lower Ip compared to helium.

assisted me in collecting the data, and running simulations.

5.2 Ion Data

The first check is to ensure that the XUV drives the majority of ionization for the target species, argon. As shown in Figure 5.2, the NIR field drives just as much ionization of argon as the XUV at an intensity of 30 TW/cm^2. This upper threshold for the intensity is much lower than that of the helium experiments, where the H_2O ionization yield superseded helium's at an intensity of 120 TW/cm^2. This large difference is due to the lower Ip of 15.76 eV in argon as compared to 24.59 eV in helium [63]. Fortunately, at an intensity of 31 TW/cm^2 and wavelength of 1.74 μm, the highest electron recollision energy, 3.17 $\times$ Up, is equal to the second ionization energy of argon, 27.63 eV. Though this estimate assumes the photoelectron has no initial kinetic energy, in principle this means the recolliding electron

should still have sufficient energy to release a second electron at this intensity.

As noted in Section 5.1.1, the harmonic comb does not drive significant transitions to excited states in the argon atom below the ionization threshold. As such, the type of two color *enhancement*s in the ionization yield as seen in helium are not observed for argon. Turning to double ionization, a significant increase in the count rate relative to helium allowed for a more robust study as a function of delay. Figure 5.3 shows a clear oscillation of the double ionization at a frequency of 2ω, however the electron spectrograms oscillate primarily at 1ω, same as in the helium experiments. This is to be expected due to the nature of the detection schemes for ions and electrons. The eTOF allows for field-free drift of the photoelectrons, so only electrons driven towards the detector are collected. Another eTOF positioned opposite the first would measure the same spectrogram but half a NIR cycle out of phase. The field plates used in the TOFMS ensures that the ions from all events are captured, regardless of the initial momenta of the ions, and so the frequency of oscillations is effectively doubled. However, this assumes there is only a singular delay within a half-cycle which maximizes the recollision probability. This is indeed the result of the semiclassical model, which predicts that the trajectories which recollide with kinetic energy greater than Up all occur within a seventh of an laser cycle following the peak of the electric field.

Contrary to helium, this argon experiment has additional sequential mechanisms that could contribute to double ionization: (1) shakeup processes and (2) tunnel ionization of the neutral atom. In the first mode the XUV photon would not only singly ionize argon but leave an additional electron in an excited state. Photons with energy greater than 29.3 eV are capable of leaving the second electron in the first excited state of Ar^+, $3s3p^6$. This excited state has an energy 14.2 eV below the second ionization threshold, so it can be easily tunnel ionized by the NIR field given that its effective binding potential is less than that of the charge neutral argon ground state. Though it is not clear why this double ionization mechanism would oscillate with sub-cycle delay steps, as the Ar^+ excited states have lifetimes of order 1 ns or longer. One possibility would be if the instantaneous AC Stark shift of the electronic states impacted the probability of the shake-up process.

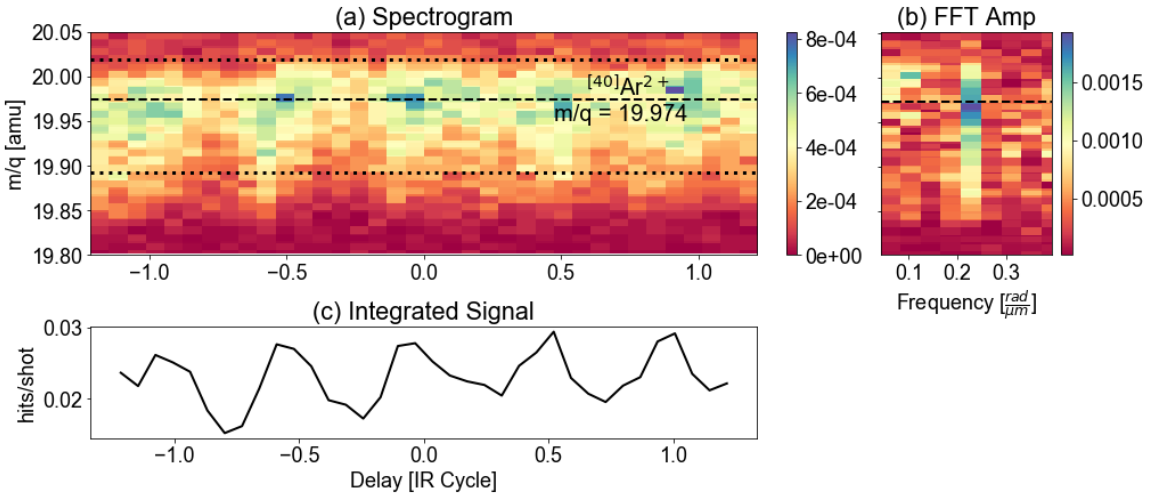

Figure 5.3: Ar^{2+} yield versus delay

The dashed line in (a) and (b) is the nominal m/q of the $^{[40]}Ar^{2+}$ at 19.974 amu/e. The dotted lines in (a) represent the integration window for the total signal plotted in (c). The NIR intensity is 30 TW/cm^2. This was one of only two NIR intensities where an oscillation of statistical significance was observed. The ratio of the mean double ionization rate to single ionization rate is a part in 2000, with a peak to peak oscillation of 15%. This is calculated by comparing the yield of $^{[40]}Ar^{2+}$ to $^{[36]}Ar^{1+}$ and multiplying the relative abundance of $^{[36]}Ar$ and $^{[40]}Ar$, as the signal at $^{[40]}Ar^{+}$ saturated the digitizer.

The second competing mechanism would be tunnel ionization of the neutral atom by the NIR field followed by single photon absorption releasing the second electron. As seen in Figure 5.2, the NIR field is just as likely to ionize argon as the XUV so the mechanism is probable. Though, again, it is not clear why this mechanism would oscillate with delay on sub-cycle time scales unless the NIR field affected the XUV absorption cross-section of Ar^{+}. Additional experiments with XUV photon energies more closely concentrated near the ionization threshold of argon are required to eliminate these two possibilities: (1) shake-up+tunneling or (2) tunneling+photoionization. Regardless, this is the most likely observations of XUV seeded recollision reported in this dissertation thus far.

5.3 Photoelectron Data

Given that the photoelectron wavepacket will have approximately 10 eV of initial kinetic energy in these experiments, as opposed to <2 eV in helium, significant differences in the

photoelectron spectrograms are to be expected. At low intensities, <10 TW/cm^2 in these experiments, a typical attosecond streaking spectrogram should appear. At sufficiently high intensities, the initial kinetic energy should become less significant in comparison to the acceleration by the NIR field and spectrograms resembling those in helium are expected. Unfortunately, the amount of background ionization events is much larger in these experiments as discussed above, so signatures of hard recollision events (2Up < Kinetic Energy < 10Up) will be even more difficult to resolve. In addition, the small fraction of electrons born with close to 0 eV of kinetic energy should minimize, or even eliminate, a low energy feature if indeed it is the result of soft recollisions.

5.3.1 Experimental Data

Figures 5.4 - 5.7 display photoelectron spectrograms spanning two and half orders of magnitude of NIR intensity. These were collected following the same procedure outlined in Section 4.3.1, and the description of the figure elements applies here as well. Many features of these spectrograms are shared with the helium experiments. At lower intensities, individual harmonic orders are still distinct as can be seen in Figures 5.4 and 5.5, but larger intensities results in a smoothing of the photoelectron distribution. The dominant frequency of the Fourier component is still 0.11 $\frac{rad}{\mu m}$ corresponding to a 1ω oscillation. The most significant deviation from the helium experiments is the phase of the 1ω oscillation as a function of kinetic energy. As explained in 1.4.2, the 1ω phase of a typical streaking spectrogram exhibit a π phase shift at the carrier energy of the XUV pulse. Here this π phase shift is observed at lower NIR intensities, but vanishes for intensities greater than 10 TW/cm^2 where the phase structure effectively flattens as seen in the helium experiments. This represents a breakdown of the photoelectron streaking paradigm that has not been reported in the literature, and this phenomenon will be further explored in the following sub-section.

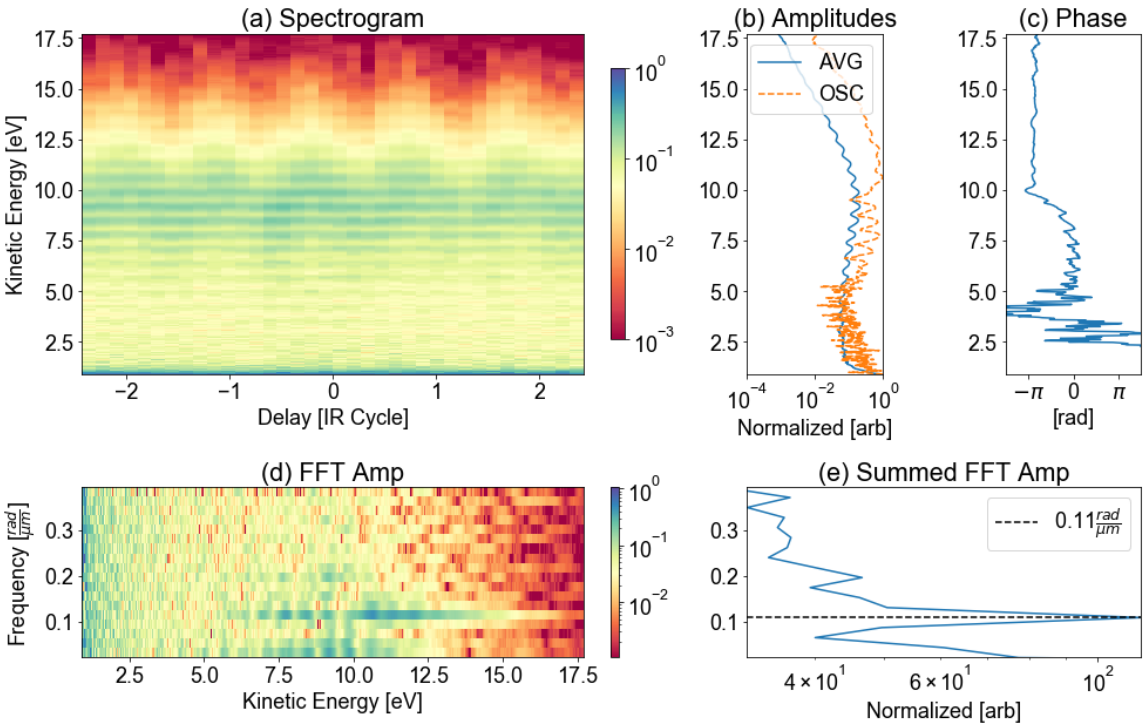

Figure 5.4: Photoelectron spectrogram, argon target, <1 TW/cm^2

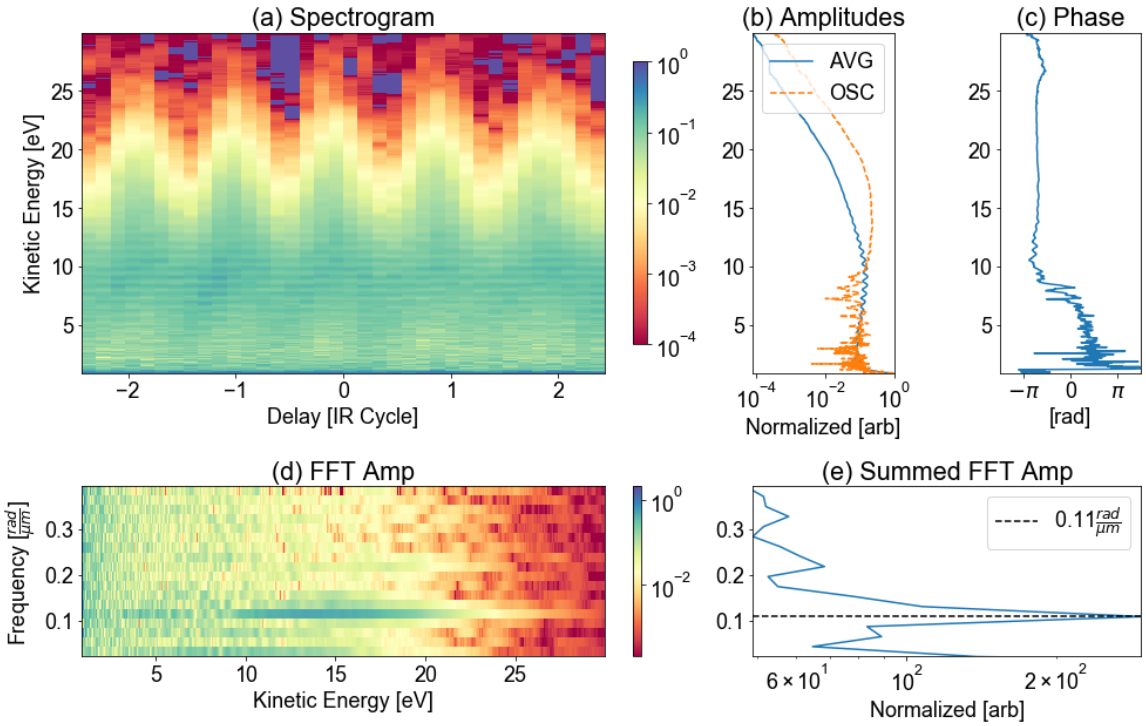

Figure 5.5: Photoelectron spectrogram, argon target, 4 TW/cm^2

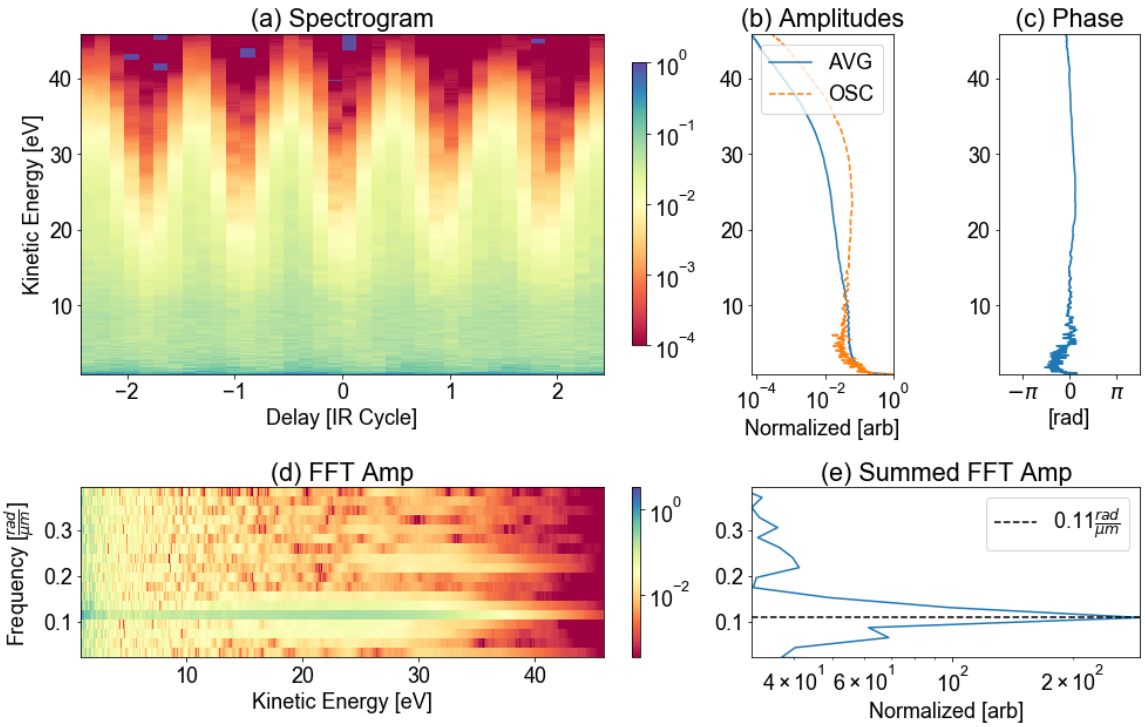

Figure 5.6: Photoelectron spectrogram, argon target, 15 TW/cm^2

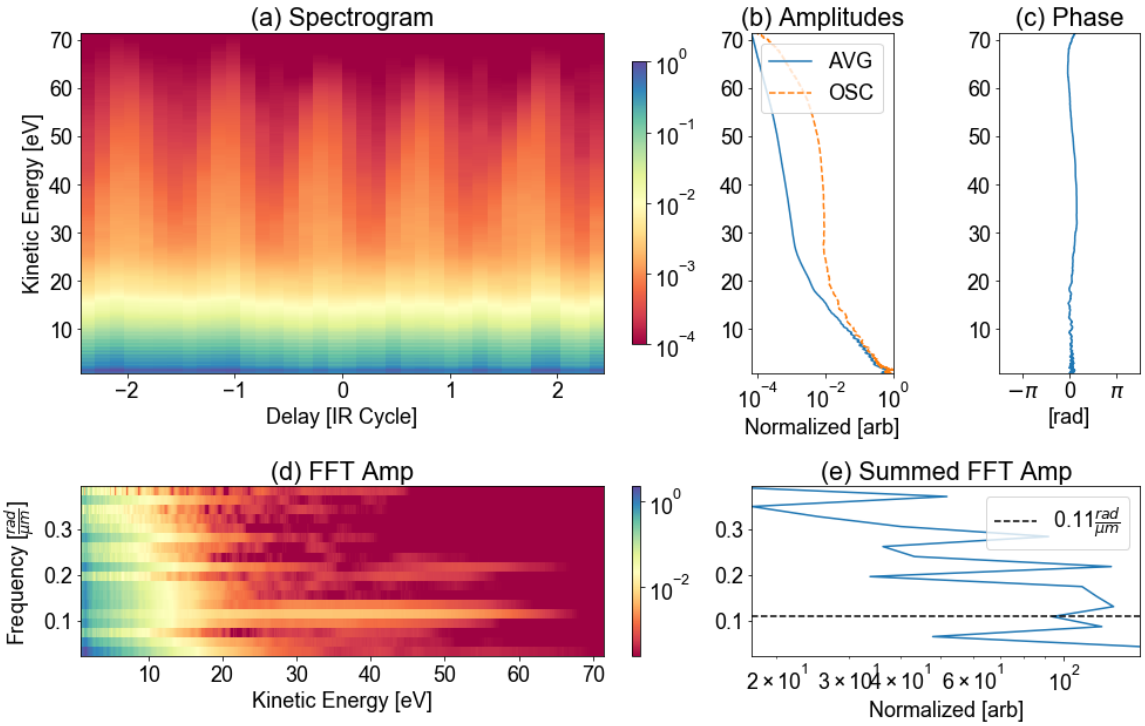

Figure 5.7: Photoelectron spectrogram, argon target, 45 TW/cm^2

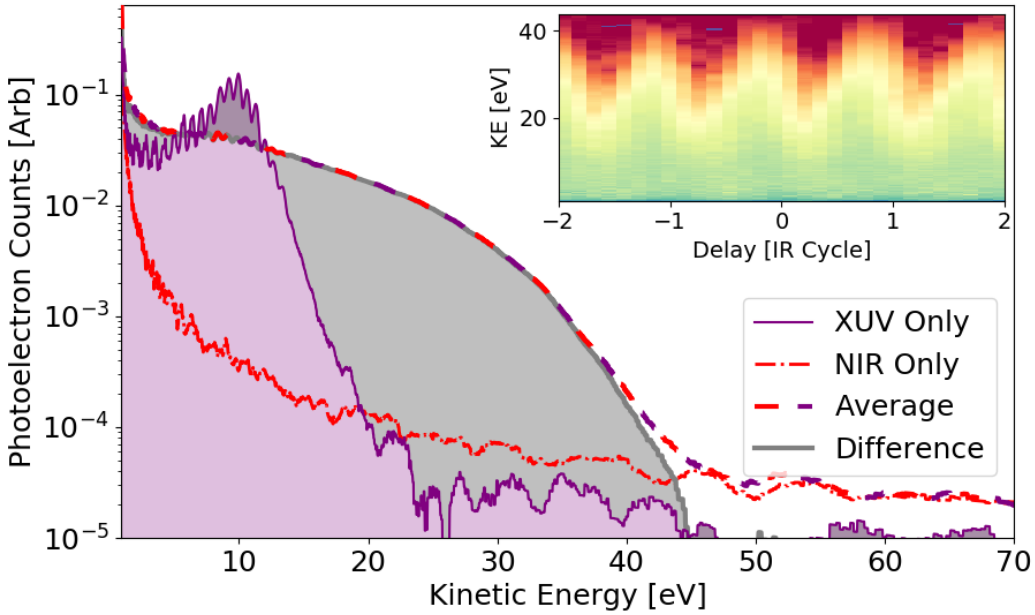

Figure 5.8: Lineouts from spectrogram, argon target, 22 TW/cm^2

Here the average lineout represents the average across delay steps in the spectrogram shown in the inset. The difference is between the average and the NIR only spectrum.

The ionization yield shown in Figure 5.2 suggests that the SFS conditions are not met for intensities greater than 30 TW/cm^2, as the NIR field will drive more ionization events than the XUV. Regardless, Figure 5.7 shows a spectrogram at an intensity 50% larger where the NIR drives the vast majority $> 99\%$ of ionization events. The NIR field drives significantly more ionization than the XUV at this intensity, however delay dependent features are still observed for kinetic energies greater than 20 eV. This results from the acceleration of the XUV ionized electrons such that the final kinetic energy exceeds the 2Up *cutoff* (24 eV for this intensity) of the electrons tunnel ionized by the NIR field. For the oscillation amplitude and phase analysis in panels (b) and (c), the oscillation frequency was fixed at 0.11 $\frac{rad}{\mu m}$ as it is the dominant Fourier component beyond 20 eV.

Figure 5.8 displays the relevant spectrogram lineouts for NIR intensity of 22 TW/cm^2, as presented for helium in Figure 4.8. The difference between the spectrogram average and the NIR only spectrum has no significant signal above the nominal *cutoff* where the high

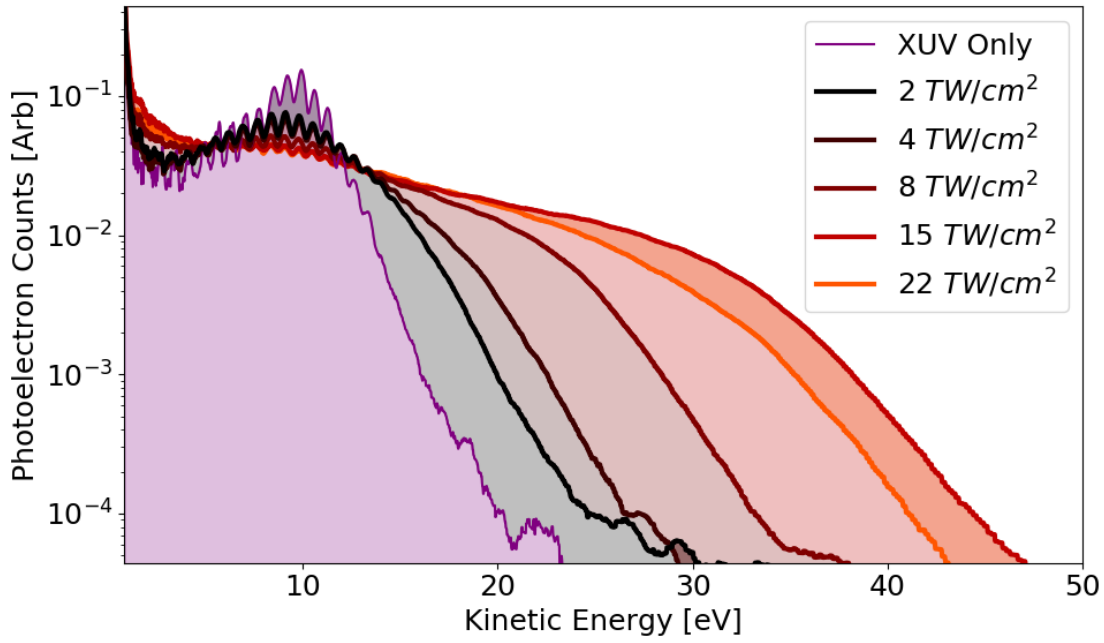

Figure 5.9: 2-Color photoelectron yields for various NIR intensities, argon target

Each curve is the difference between the spectrogram average and the NIR only spectra. These can be directly compared for relative increases in yield.

energy recollision events would occur. The difference spectrogram also lacks the significant peak at low kinetic energies associated with low energy recollision events. None of the spectrograms collected exhibited features that could be attributed to recollision. In addition, the *enhancement* of the total photoelectron yield is minimal with only a 17% increase in signal between the difference and XUV only spectra. The only feature of the difference spectrum that has increased in comparison to the helium results is the *cutoff* or maximum kinetic energy observed. In helium at this intensity, the *cutoff* would lie at 35 eV but this spectrograms *cutoff* is closer to 45 eV. This shift is comparable to the shift in the average kinetic energy of the wavepacket launched by the XUV, Ip_{He} - Ip_{Ar} = 8.7 eV.

5.3.2 Intensity Scaling

Figure 5.9 shows the difference spectra for intensities ranging from 2 to 22 TW/cm^2. Of particular note is the lack of any significant intensity dependent *enhancement* of the total

photoelectron signal as observed in helium. All of these spectra integrate to the same total yield ±20%. However, the *cutoff* and *CoM* clearly still increase with the NIR intensity, similar to the helium experiments. Figure 5.10, shows the feature scaling of the argon spectrograms collected. Note that the definition of the *cutoff* was changed to a reduction in counts of 10^4, as opposed to 10^5 in helium. This is due to the exponential increase in background ATI photoelectrons increasing the effective noise floor for these experiments at higher NIR intensities.

The most dramatic change from the helium experiments is the *enhancement* shown in panel (a) where the linear fit returns a slope of effectively zero. It appears that the on-axis photoelectron focusing does not occur in these experiments, perhaps the initial kinetic energy of these photoelectrons prevents the NIR field from significantly altering the angular distribution. The *cutoff* scales faster than in the helium experiments with a slope of ∼3Up. This is attributed to the nature of the photoelectron streaking which depends on the cross term of the canonical momentum, $\vec{p} \cdot \vec{A}$. So the increased kinetic energies allow for more effective acceleration by the NIR field. This emphasises the importance of having an XUV pulse with photon energies at the ionization threshold to effectively recreate traditional strong field phenomena. Panel (d) demonstrates how quickly the other SFS condition is broken in these experiments, as tunneling ionization by the NIR field becomes the primary ionization mechanism past 30 TW/cm^2. If the data at 45 TW/cm^2, Up = 12.7 eV, is treated as an outlier, the *CoM* shows only a small shift as a function of NIR intensity. This is to be expected as this experiment is closer to a traditional attosecond streaking experiment where the photoelectron distribution is accelerated and decelerated with equal amplitude. However, at sufficiently high intensities this initial kinetic energy should become irrelevant and an approximation to the SFS can be achieved. In principle this same logic should apply to the helium experiment where the initial kinetic energy of a typical photoelectron was 1.7 eV, however the intensity threshold where this initial kick becomes irrelevant is presumably much lower. Determining the intensity at which a given kinetic energy becomes insignificant could provide a useful benchmark, quantifying the boundary separating the SFS regime from traditional attosecond experiments.

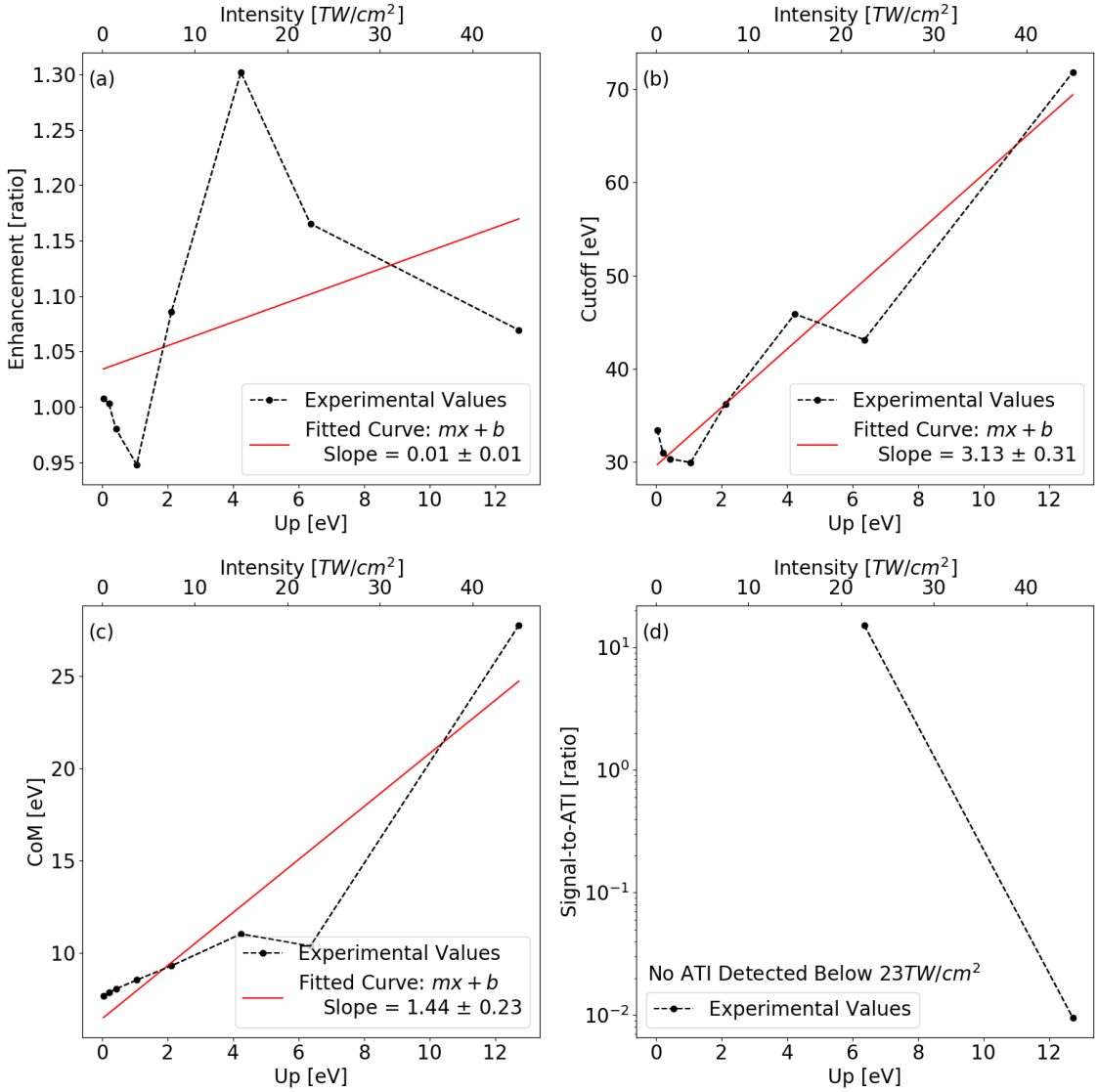

Figure 5.10: SFS feature scaling in argon photoelectrons

See Equations 4.3 - 4.6 for definitions of the ordinate in each subplot. The *cutoff* here is changed to a reduction in signal amplitude of 10^4.

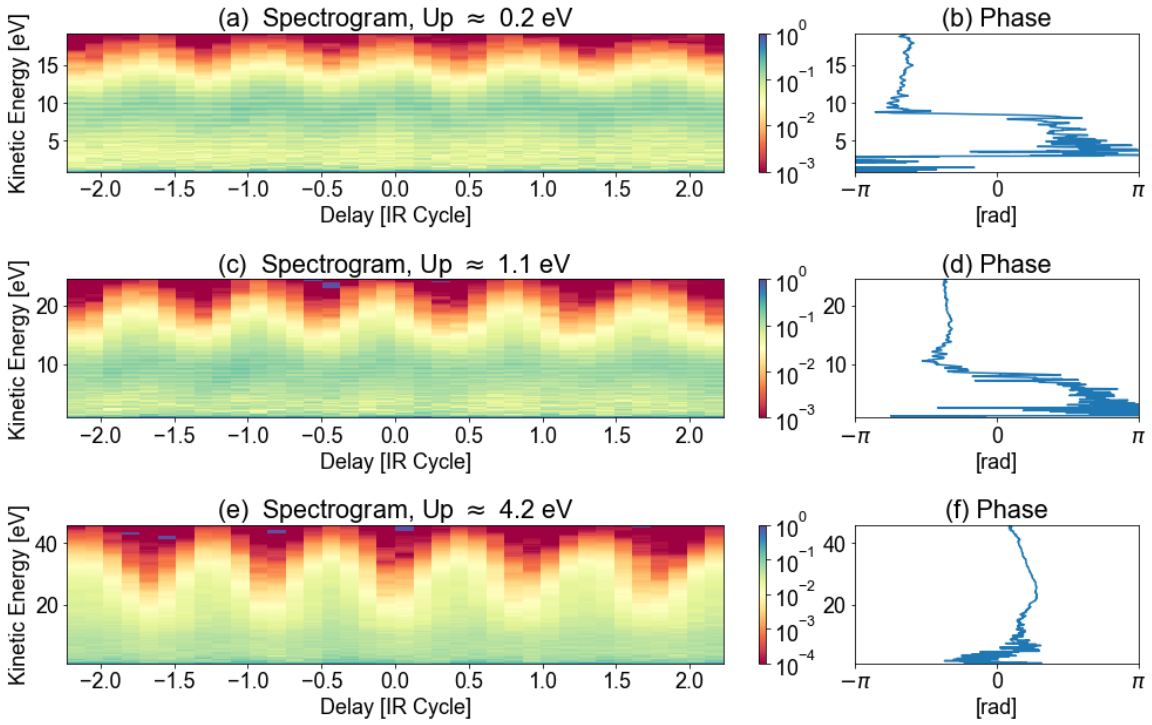

Figure 5.11: Photoelectron spectrograms with 1ω phase extracted, argon target

5.4 The SFS Regime

A significant feature in the argon data that was not present in helium is the π shift in the phase of the 1ω oscillation centered on the carrier XUV photon energy. Again, this is a common feature of typical attosecond streaking experiments. The evolution of this phase shift as a function of intensity is emphasized in Figure 5.11 which displays the spectrograms and 1ω phases for three values of Up. It appears that once the NIR pulse is of sufficient intensity then the π phase shift vanishes and does not return. The lowest intensity where this is observed in the experiment is at 15 TW/cm^2 or Up of 4.2 eV. At higher intensities the phase flattens similar to the results from the helium experiments. Similar observations were made in neon, although the phase flattened at a lower intensity of 1.5 TW/cm^2 or Up of 0.4 eV, see Appendix C. In an attempt to create a quantitative benchmark for satisfying the SFS condition, this vanishing of the π phase shift will be further investigated using SFA simulations.

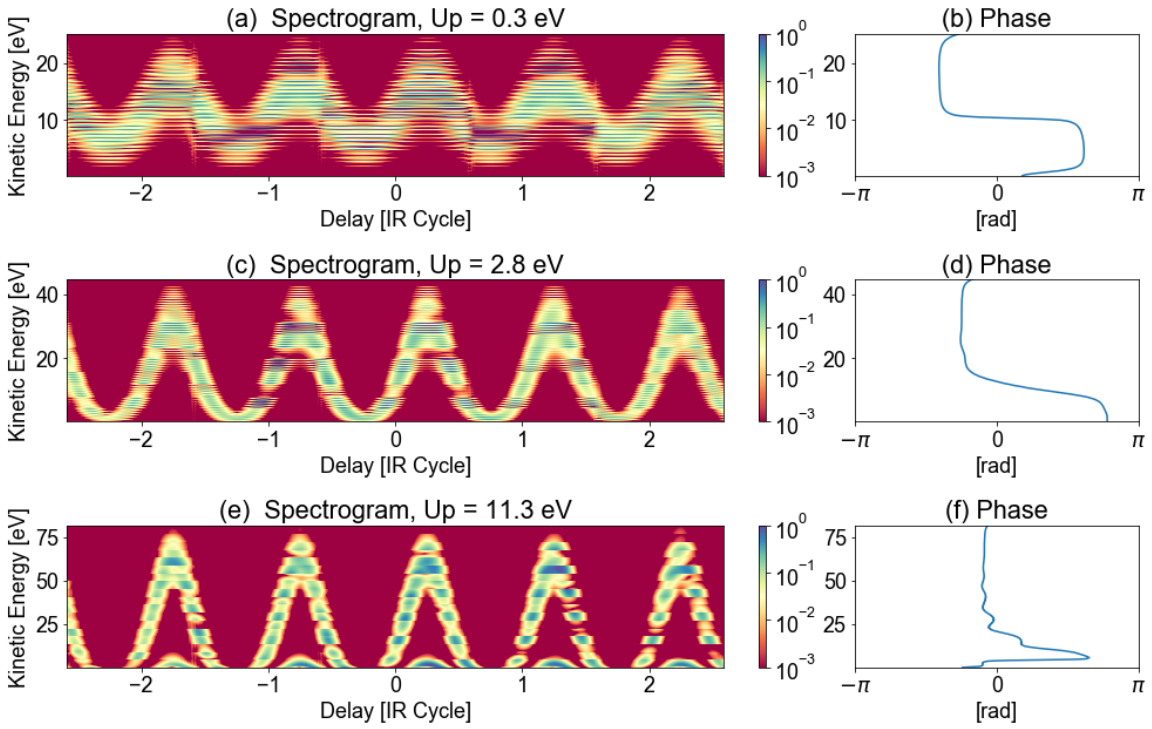

Figure 5.12: SFA photoelectron spectrograms, argon target

5.4.1 SFA Simulations

Using the same procedure as outlined in Section 4.3.3, simulations were done using the SFA to model the photoelectron spectrograms with argon as the atomic target. The results from selected spectrograms are show in Figure 5.12. For the two smallest Up, panels (a-d), the spectrogram looks like a typical attosecond streaking experiment and the evolution of the 1ω phase exhibits the characteristic π phase shift. In panel (f) this phase shift is reduced and correlated with the appearance of a new feature at low kinetic energies in the spectrogram (e). This added feature at low energy oscillates in phase with the maximally accelerated photoelectrons and at first glance is similar in appearance to the low energy feature observed in the helium experiments. However, the SFA simulations for helium never exhibited this low energy feature, and recall that these simulations do not capture the physics of recollision. The Up at which this feature appears is suggestive of another explanation. The mean kinetic energy of the photoelectron wavepacket for these experiments and simulations is 10.6 eV, so

in panel (f) the Up is greater than the initial kinetic energy of many photoelectrons. In this case there should be photoelectrons at particular delays with initial momenta imparted by the XUV ionization pointing away from the TOF detector and drift momentum imparted by the NIR that is both greater in magnitude and opposite in sign. This would explain both the appearance of this feature at low energy, as the momenta largely cancel, and that it oscillates in phase with the features at higher energies. In fact, the appearance of this feature at low energy, for the relative scaling of Up and kinetic energy seen here, was predicted by Itatani et al. in 2002 [52]. The breakdown of the π phase shift provides information about the presence of these additional photoelectrons. The breakdown of the phase shift should be a universal feature always observed when Up is greater than the initial mean kinetic energy of the photoelectron wavepacket. Figure 5.13 demonstrates this effect by analyzing the 1ω phase of SFA simulations using the same conditions as above, but the carrier energy of the XUV pulse is varied to impart different amounts of initial kinetic energy. As expected the π phase shift breaks down whenever the Up matches or exceeds the initial kinetic energy.

At this point, it is worth returning to the question posed in the last section: where is the boundary between a traditional attosecond streaking experiment and an SFS experiment? These SFA simulations suggest a minimum threshold that the Up of the NIR field must be greater than the mean kinetic energy of the photoelectron wavepacket launched by the XUV. Experimentally, this condition can be checked by looking for the NIR intensity where the π phase shift of the 1ω oscillation is no longer observable. In the case of helium this condition was easily met, where the XUV carrier energy was <2 eV above the ionization threshold and Up could be a factor of 10 greater. In argon, the Up is only 8.5 eV when the other SFS condition is broken, that the majority of ionization is driven by the XUV. Therefore, it was impossible to conduct a true SFS experiment here. A small set of experiments were conducted in neon, see Appendix C, with the same XUV pulse, where the carrier energy is only 4.8 eV above the ionization threshold. Here the transition from the streaking to SFS regime is better observed while driving the majority of ionization with the XUV field.

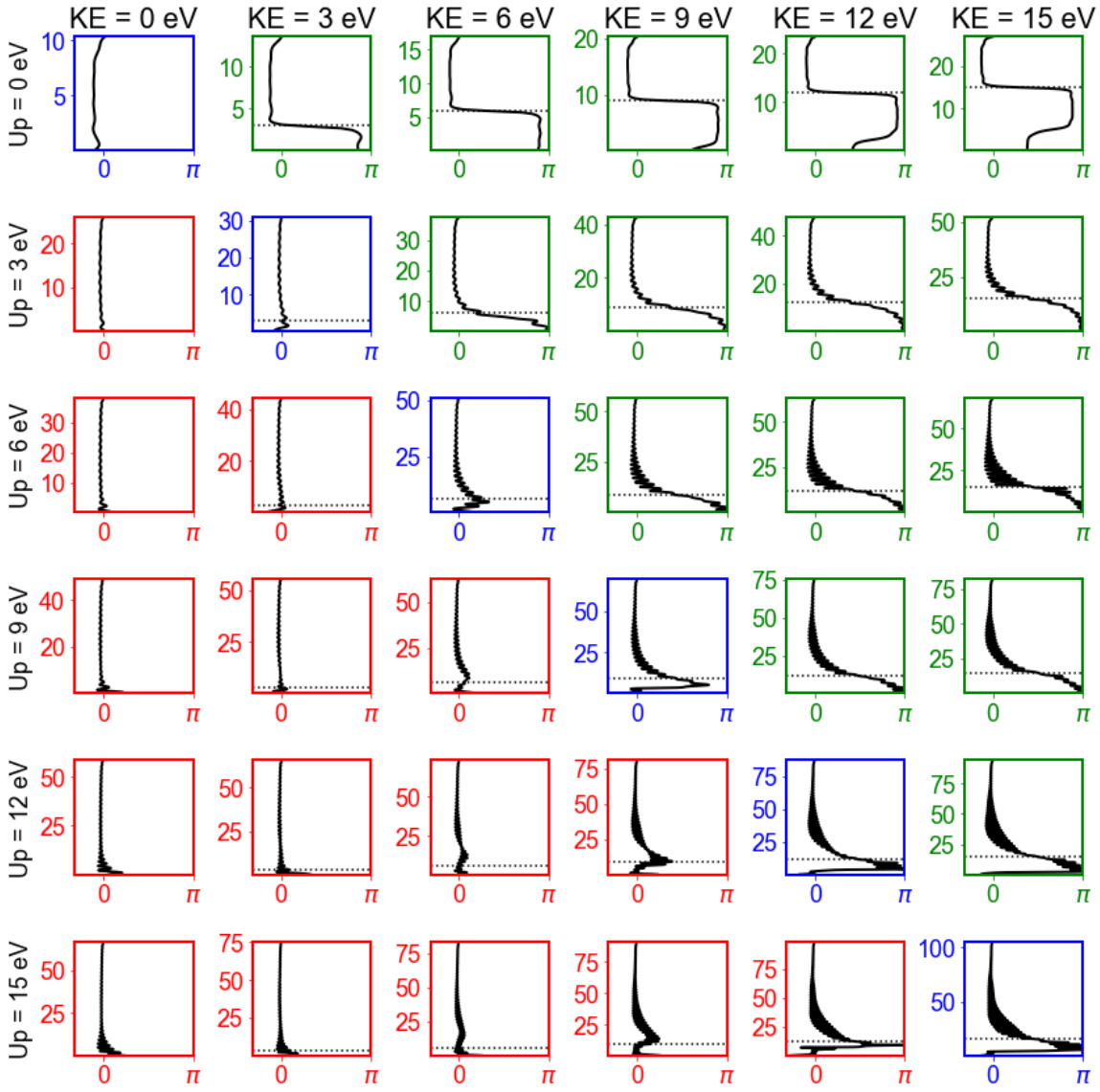

Figure 5.13: 1ω phases for various Up and mean kinetic energy

The abscissa for each plot is the phase of the 1ω oscillation and the ordinate is the final electron kinetic energy. These simulations were done using a transform limted 500 as XUV APT with a single pulse per NIR cycle, and a fixed target Ip. The carrier photon energy and the Up of the NIR field were varied in increments of 3 eV. Columns correspond to constant carrier photon energy and are labeled above by the corresponding mean kinetic energy of the photoelectron wavepacket. Rows are at constant Up with labels on the left. The plots with blue axes along the diagonal are cases where the mean kinetic energy and Up are equal, red axes have greater Up, and green greater mean kinetic energy. In all cases the π phase shift is present in the green region, centered at the mean initial electron kinetic energy marked by a dotted line, but vanishes in the red region.

5.5 Conclusions

Although the spirit of the SFS concept was not met by these experiments in argon, they yielded some interesting results that can guide future experiments. First, the observed oscillation of double ionization events at a frequency commensurate with the NIR field is likely evidence of recollision occurring. Second, studying the phase structure of the photoelectron spectrograms yielded an experimental observable, the π phase shift, that can be used to determine if future experiments meet the SFS criteria. Conducting further experiments in argon, where both the XUV absorption and electron impact cross-sections are larger than helium [64, 76], with an XUV pulse closer in energy to the ionization threshold is a promising direction for future work with the SFS.

Chapter 6
Conclusions

"It is good to have an end to journey toward; but it is the journey that matters, in the end."

— Ursula K. Le Guin, The Left Hand of Darkness

6.1 Review

The goal of the SFS experimental campaign, and this dissertation, was to observe and control recollision using a two-color, XUV and NIR, field. At this time no single piece of evidence can determine if this has been achieved, but I believe the preponderance of evidence suggests that it has. Table 6.1 summarizes the key experimental features observed in the three atomic targets studied in this dissertation: helium, neon, and argon. Only the experiments in helium constitute true SFS experiments and the argon experiments reside outside the required parameter space. Neon presents an interesting middle ground and its results are presented in Appendix C.

The features in the table are as follows:

1. Enhancement Magnitude: increasing photoelectron yield with NIR intensity resulting from focusing of the angular distribution, defined in Equation 4.3.

2. Asymmetric Large Delays: the increased yield resulting from NIR tunneling after XUV excitation to bound states, see Figure 4.17.

3. Low Energy Feature: large peak in the photoelectron spectrograms at low energies, <2 eV, oscillating in phase with the highest photoelectron energies, see Figure 4.15.

Atomic Species		He	Ne	Ar
Electron	Enhancement Magnitude	Large	Medium	Small
	Asymmetric Large Delays	Yes	Weak	No
	Low Energy Feature	Yes	Yes	No
	Pi-Phase Shift Observed	No	Yes	Yes
Ion	Single Ionization Enhanced	Yes	No	No
	Single Ion Oscillation	No	No	No
	Double Ionization Observed	Yes	No Data	Yes
	Double Ion Oscillation	No Data	No Data	Yes

Table 6.1: Survey of results collected for this dissertation
See text for descriptions of the experimental features reported here.

4. Pi-Phase Shift: the deviation in phase of the 1ω oscillation expected for typical attosecond streaking experiments, see Section 5.3.1.

5. Single Ionization Enhanced: increase in the single ion yield when the NIR and XUV fields are combined, attributed to tunneling from bound states, see Figure 4.2.

6. Single Ion Oscillation: double ionization events proportionally reduce the single ionization yield, and the two should oscillate π out of phase, not observed.

7. Double Ionization Observed: significant enhancement of the double ionization yield when the NIR and XUV fields are combined, see Figure 4.3.

8. Double Ionization Oscillation: fluctuations of the double ionization yield as a function of delay with frequency commensurate to the NIR field, see Figure 5.3.

The strongest evidence that I observed and controlled electron recollision is the results of double ionization in helium and argon. As discussed in Sections 4.2.2 and 5.2, there are other possible mechanisms one could imagine that doubly ionize these targets however they require more complex interactions or even previously unobserved physics. Occam's Razor points towards recollision. In addition, the observation of a feature at low kinetic energies

in helium and neon could be the SFS equivalent of the LES which imply that we can access and control the soft recolliding trajectories.

In the rest of this chapter I will discuss both desirable improvements to the experimental apparatus and possibilities for future experiments. The former will allow for measurements with greater statistical power to resolve the recollided electrons past the 2Up cutoff and an oscillation of the helium double ion yield. The latter could both provide definitive evidence that we are controlling recollision and actually advance our understanding of strong field physics and electron correlation.

6.2 Experimental Improvements

Future experiments with the SFS will require measurements with greater statistical power for observing features of recollision. Some gains can be made by increasing the gas density in the interaction region, with the consequence of raising the ambient pressure in the chamber. The MCP detectors become a limiting factor as they can be damaged by operating at gas pressures above 10^{-5} Torr, and these experiments were carried out at chamber pressures of 10^{-4} Torr. Anecdotal experience suggests that with helium as the atomic target it is possible to increase the chamber pressure, and therefore interaction pressure, by another order of magnitude and still use the MCP detectors for some time without damage. For measurements of double ionization of helium, finding some means of further separating the He^{2+} and H_2^+ peaks would also be beneficial. The use of helium-3 would be a simple solution, though the operating costs would be prohibitive. Alternatively, modifications to the electrical feedthrough allowing for larger voltages to be applied to the field plate can increase the difference in TOF of the two species, and therefore the resolution of the TOFMS.

The range of intensities that are viable, where the majority of ionization is driven by the XUV, can also be increased for helium experiments by a new pipeline delivering the gas into the detector chamber. Currently the system uses compression fittings for connecting the tubing, valves, and regulator from the bottle of helium to the gas feedthrough. The

presence of atmospheric contaminants at significant partial pressures, see Figure 4.1, observed only when the helium gas is fed into the system suggests this gas delivery system is insufficiently sealed. Replacing these compression fittings with vacuum rated connections and valves should dramatically reduce the amount of contaminant species. This will reduce the photoelectrons produced by the NIR field, and hopefully allow for observations of high energy recollided electrons past 2Up.

6.2.1 Longer Wavelengths

Recently the Agostini-DiMauro Research Group has developed a NIR 2.4 μm laser source with 6 mJ of pulse energy, 39 fs duration, and 1 kHz repetition rate [67]. As discussed in Section 3.2, moving to longer NIR wavelengths allows for dramatic reductions in the tunneling ionization rate for fixed Up. This could prove essential for future SFS experiments in lower Ip targets such as argon, krypton, and xenon where the tunneling ionization rate will be orders of magnitude higher for comparable intensities in helium. One challenge is the $\lambda^{-5.5}$ scaling of the XUV yield in HHG, where moving from 1.74 μm to 2.4 μm would imply a $\sim$5.9x decrease in the XUV flux. However, the increased XUV absorption cross-sections of these larger atomic targets can compensate for some of these losses. In addition, the increased pulse energy and shorter pulse duration will allow for more effective HHG, recovering some of the losses from using a longer wavelength. One other cost in changing the wavelength would be needing to rebuild the interferometer, as the transmissive optics all have anti-reflective coatings for 1.7 μm. From the work in this dissertation it appears that experiments in argon could be done without this change in light source, but experiments in krypton or xenon would likely require it.

6.2.2 Changing XUV Bandwidth

Another modification that will be needed for future experiments in lower Ip targets is the use of different combinations of thin metallic foils and dielectric mirrors to tune the bandpass of the XUV light, see Figures 3.8 and 3.9. Figure 6.1 plots the XUV bandpass for each various combinations relative to the ionization energies of several atomic targets. A combination of

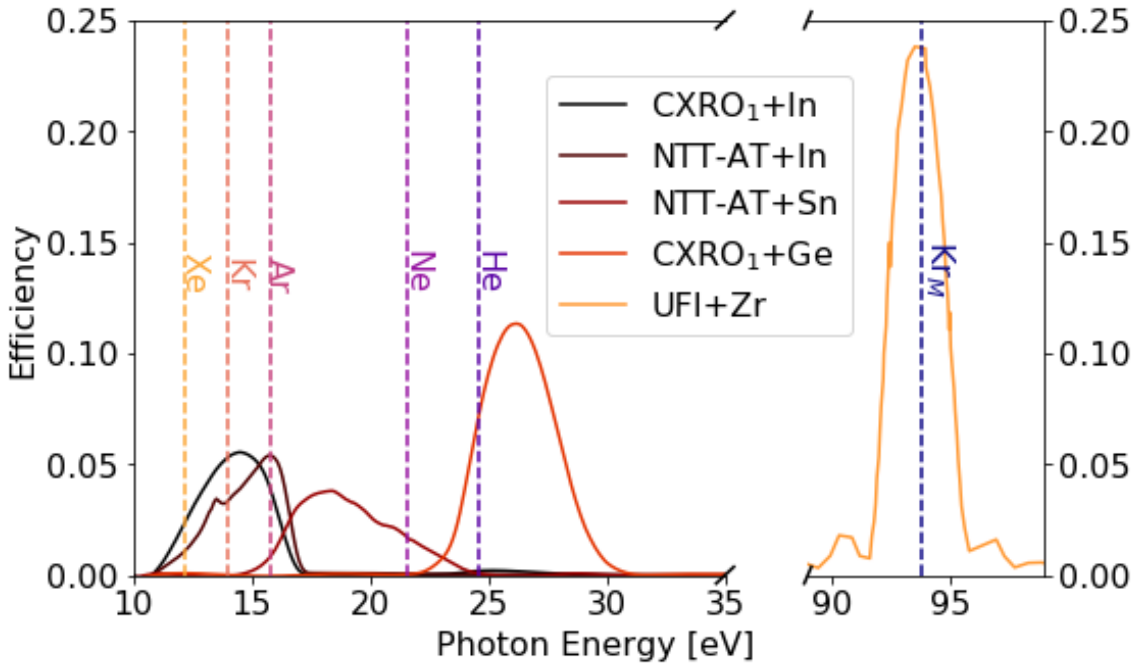

Figure 6.1: Possible XUV bandpasses by combining mirrors and filters

Efficiency is defined as the product of the foil transmission and the mirror reflectivity. The combination of mirror label and foil material is provided in the legend. Here the M edge for krypton is included at 93.8 eV. The UFI mirror is model XUV94BW3 manufactured by Ultrafast Innovations.

the NTT-AT mirror and an indium foil would be optimal for experiments in argon, $CXRO_1$ and indium for experiments in xenon or krypton, and $CXRO_1$ and tin for neon. Ideally a more suitable mirror for neon would be obtained in the future. Using a zirconium filter and the XUV94BW3 dielectric mirror manufactured by Ultrafast Innovations, an XUV pulse could be created with carrier photon energy at the M edge of krypton. This would be a novel SFS experiment where the photoelectron is ionized from a core level, and recollision would occur with a full valence shell of electrons. Fortunately, changing the mirror and filter are minimally invasive procedures compared to the other modification outlined above.

6.3 Future Work

The SFS concept and the experiment apparatus built are ready for a variety of high impact projects to explore recollision physics. Returning to helium after making the modifications

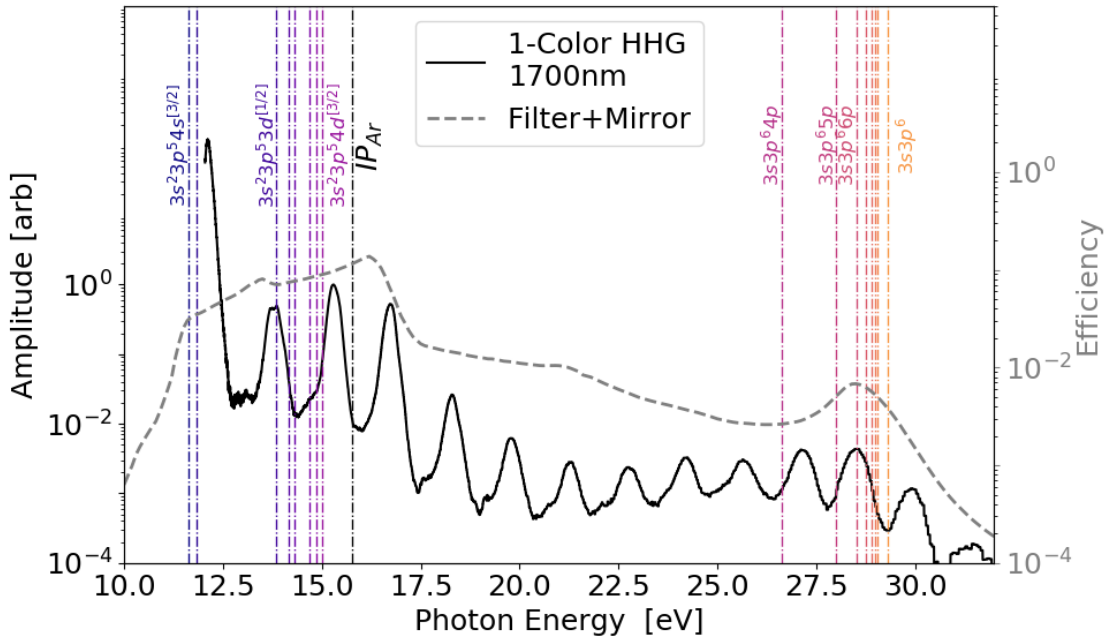

Figure 6.2: HHG spectrum to be used in future argon experiments

Qiaoyi Liu and Yaguo Tang were responsible for installing the NTT-AT mirror, mounting the indium filter, and making this measurement. States with dipole allowed transitions from the ground state of greatest oscillator strength are plotted below the ionization threshold of argon, as well as the autoionizing states below 30 eV in energy.

to the gas delivery system and using increased interaction pressures is essential to studying electron correlation in the most simple two-electron system, a primary motivation for these experiments. Afterwards, the first natural extension is to iterate through the other noble gas targets such as argon, krypton, and xenon. As of writing this dissertation, a fruitful campaign is being conducted with argon using the XUV pulse presented in Figure 6.2. Already many features observed in the helium experiments (Chapter 4), but not in argon (Chapter 5), have been reproduced such as the low energy feature, a resonant like enhancement in single ionization for large delays, and significant electron enhancement attributed to focusing by the NIR field. In addition, a stronger oscillation of the double ionization yield has been measured, with a ∼4x increase in the double to single ionization ratio. A publication reporting the results of these latest experiments in argon is in preparation at the time of writing this dissertation.

6.3.1 Crossed Polarization Scheme

The dependence of NSDI and HHG on the NIR field ellipticity is a key characteristic of recollision, and is attributed to the diminished recollision probability when the electron gains transverse momentum from the field [23, 36]. In an effort to rule out other mechanisms for doubly ionizing argon in the SFS, experiments could be conducted in a crossed polarization scheme where the XUV and NIR fields are perpendicular to each other. In this situation, whatever excess energy there is between the XUV photon energy and Ip of the target will result in transverse momenta, analogous to the experiments with elliptic NIR fields. The magnitude of the transverse momentum could be finely controlled by tuning the wavelength of the NIR field, and correspondingly the XUV harmonic photon energies, without effecting the polarization state of the NIR. It has been suggested that exploring the novel trajectories involving transverse momenta can provide important insights into the nature of electron correlation in NSDI [95]. These proposed SFS experiments would allow for a robust study of such trajectories.

6.3.2 Sub-threshold Excitation

Another avenue for future experiments would be to create an XUV pulse with photon energies exclusively below the ionization threshold of a target. In this situation, the XUV would not drive single photon ionization by excitation to high lying bound states. The NIR field would then tunnel ionize the electron and drive recollision from excited states with small effective Ips. These events are likely to already be occurring in these experiments in helium, see Section 4.4. Isolating the role of this ionization mechanism could provide deeper insights into the results in this dissertation.

6.3.3 Recollision with Core Electrons

As discussed in Section 6.2.2, there is an optimal combination of metallic filter and dielectric mirror to create a narrow comb at the M absorption edge of krypton. This would provide a novel study of recollision with a full valence shell for an atomic target. Attosecond NIR

and XUV experiments have already explored the timescales of Auger processes for M edge excitations in krypton, and the observed dynamics had lifetimes of order 10 fs [50]. Using a 2.4 μm light source, with period 8 fs, a rich set of competing ionization channels would be populated and interferences between Auger and recollision ionization could be observed. The photoelectron spectra would be densely populated between the wavepacket ionized from the valence shell at $\sim$ 80 eV of kinetic energy, the core states with little to no energy, the Auger electrons from 28 to 45 eV [84], and the rescattered electrons. The ion spectra would be equally enriched, as multiple ionizations beyond the second can be driven by both recollision and Auger decay in krypton.

6.3.4 Frustrated Tunneling Ionization

Both the SFS measurements already conducted and these proposals for future experiments could be used to explore the role of Frustrated Tunneling Ionization. This phenomenon suppresses the single ionization rate due to tunneling in a laser pulse as recollision drives electrons to be trapped in Rydberg states [86]. A laser pulse at the saturation intensity for ionization of the target's excited states would probe for the presence of these trapped electrons. With the long (ns scale) lifetimes of these Rydberg states this probe pulse could be delayed by picoseconds so as to leave the SFS experiment unaffected. Differential measurements of the electrons or ions with and without this probe pulse as a function of delay between the NIR and XUV field would experimentally reveal the trajectories resulting in Frustrated Tunneling Ionization.

Appendix A
Vacuum System Operation

A brief explanation of the different menus in the control interface will preface a more thorough discussion of how to utilize the different PLC processes. Figure A.1 shows the null state of the software (no active processes and chambers at atmosphere). Note that the PLC controls for the generation and differential chambers are combined as they are connected by a vacuum aperture, so they should always be operated in the same vacuum state. There is a title bar, three push buttons directing to other menus as labeled, and three indicators for each chamber: armed/unarmed, atmosphere/vacuum, and okay/error. Each menu contains a button marked "HOME" to return to this home screen. The valves menu contains 5 buttons: one for each gate valve in the roughing lines, one for the VAT valve separating the differential pumping and recombination chamber, and one directing to a sub menu with controls for the venting valves of each TMP. The PUMP-VENT menu, as seen in Figure A.2, in the null state simply has two push button controls for each chamber: a start button to begin pulling vacuum and one to arm the chambers once at vacuum. After a start button is pressed, it will indicate the corresponding TMPs have been sent ON signals, a new indicator will display "PUMPING" until the chamber passes its lower set-point, and a new button will allow the user to begin a venting process. The Error menu has 9 indicators which will light when either a TMP throws an error (indicators T1 - T5) or a chambers low set-point has been tripped after pulling vacuum on the chambers. These indicators will remain on until the user presses the button to clear errors.

These instructions will begin assuming the system is in a null state where the chambers are at atmosphere, all valves are closed, and there are no processes activated through the PLC. Before pulling vacuum on the chambers, the user should ensure the following:

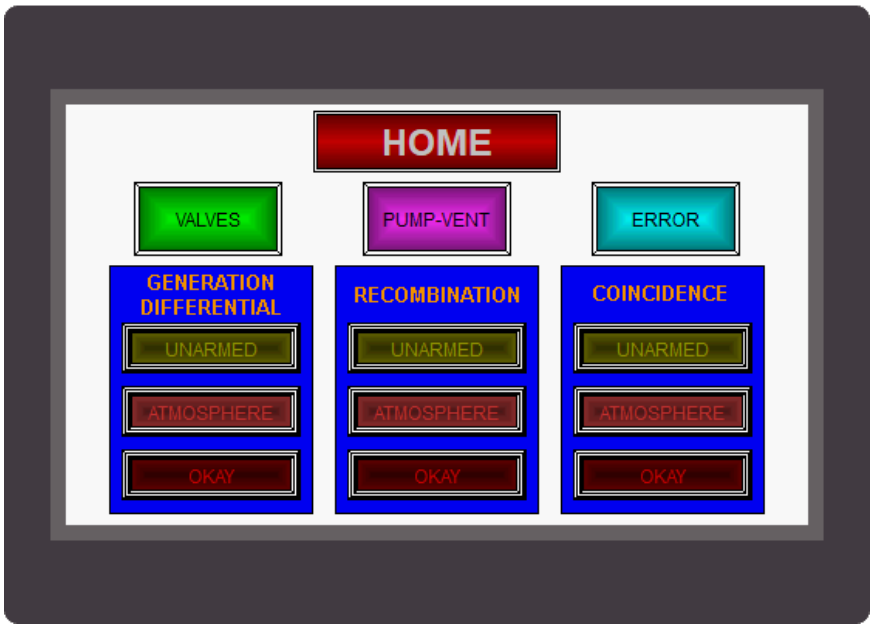

Figure A.1: Home screen display of the vacuum PLC

A touchscreen interface is used to control the vacuum system. This screenshot displays the system in the null state where each chamber is at atmospheric pressure and no error signal are received. Menus for the various valves, system processes, and error signals allow the user to control the vacuum hardware.

- The hand valves for the chilled water and nitrogen are all open.

- The manual gate valves on the roughing lines are closed.

- The roughing pumps are on.

- The power supplies for the magnetically levitated TMPs are on.

At this point the home screen on the touch display should appear as in Figure A.1. The pump down processes can then be started in the PUMP-VENT menu. To begin pulling rough vacuum on the chambers the manual gate valves are slowly opened by the user. The EcoDry pumps will make an audible whining sound as they are exposed to the chambers at atmospheric pressure. It is up to the judgement of the user to open the hand valves slowly enough to not overwhelm the EcoDry pumps. Once the chamber pressure passes the first pressure set point, set point low for each chamber, the corresponding TMP will be turned on. For all chambers, this low vacuum set point is at 200 mTorr. With the TMPs running the chambers will approach high vacuum pressures, on the order of 10^{-6} Torr in the first 30

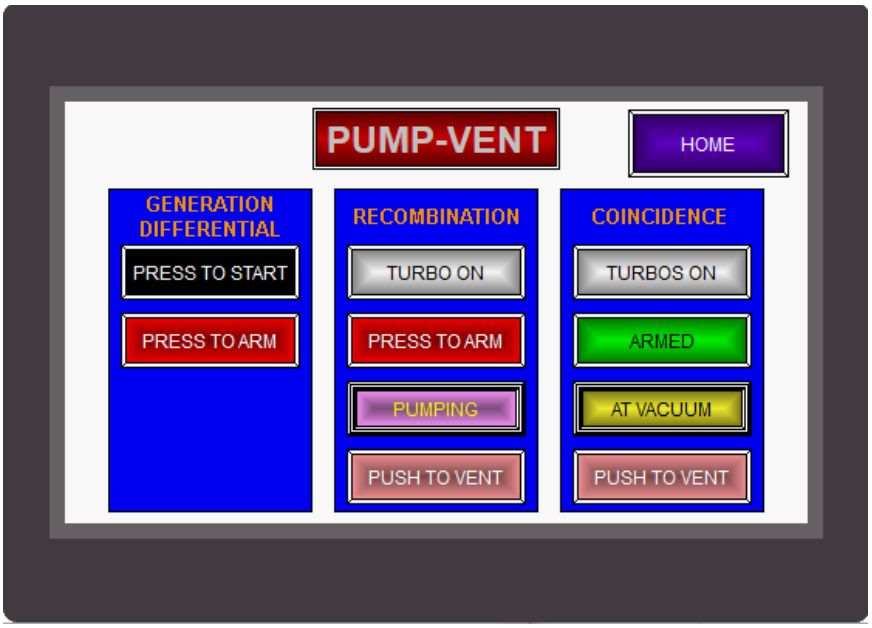

Figure A.2: PUMP-VENT menu for PLC system.

The PLC is in a process of pulling vacuum on recombination and detector chambers. The generation and differential chambers are left at atmospheric pressures. Once a chamber(s) are at vacuum, arming the chamber allows the PLC to respond to system errors with a venting procedure to prevent damage to the apparatus.

to 60 minutes. Once the chamber pressure drops below the high vacuum set point, which is set slightly differently for each chamber, the touchscreen display will update to show that the chamber is at VACUUM. Left overnight the chambers will be at the 10^{-8} Torr level or below. Within a day or two, the differential pumping and recombination chambers will drop below the measurement range of the Penningvac PTR 90 N vacuum gauges. At this point, the L.E.D. indicator on the gauges will turn red, and the controller will read a pressure of $5e^{-5}$ Torr, which is the lower limit of the low vacuum range of the gauge. It is recommended that the hysteresis for each set point, the upper set point limit, is set so that this behavior does not lead to unintended behavior from the PLC.

Venting a chambers is as simple as unarming the PLC, and pressing the PUSH TO VENT button. The venting process for any chamber begins with the VAT valve closing so as to prevent the laser from damaging something downstream if it is in the system. After this the TMP(s) will receive an off signal and begin to spin down, after an additional minute

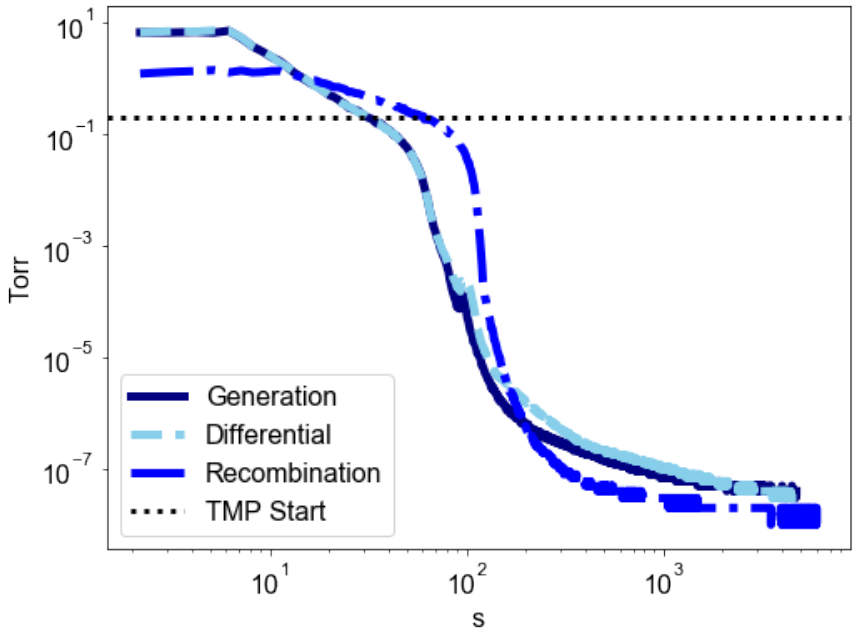

Figure A.3: Pump down curves for new vacuum chambers.

Pressure versus time for the generation, differential, and recombination chambers during a pump down process. The anomalous structure at 10^{-4} Torr and 100 seconds corresponds to where the dual mode vacuum gauge switches from Pirani to cold cathode type pressure measurements. The set point where the TMPs are switched is marked at 200 mTorr.

the vent valve(s) will open to help brake the TMP(s) and begin to bring the chambers up to atmosphere. The system will stay in this state for 30 minutes, after which it is assumed the TMP(s) have stopped spinning. The roughing gate valves and the venting valves will all close. Typically at this point the chamber will be at a pressure of a few Torr. It is recommended to now close the hand valves on the roughing lines for the vented chambers to ensure they are closed prior to the next pumping process. Entering the venting valves sub-menu, the user can reopen the venting the valves to bring the chambers fully up to atmospheric pressures, this typically takes another hour.

CAUTION: The only caveat to the above is if the user desires to vent one chamber in sub-system 2 but not the other, the recombination or detector chambers, it is impossible to do this for sub-system 1. The roughing line pressures will rise too high to safely operate the TMP(s) of the chamber not venting and could throw a magnetically levitated off its

bearings. It is recommended in this situation to either partially or completely close the hand valve to the corresponding venting line of the chamber being pumped down. The goal in this situation is to keep the roughing lines at a pressure below a few hundred mTorr.

For safe operation of the vacuum system while the user is not present, it is best practice to leave the chambers armed whenever their corresponding TMPs are running. Once armed, the system will act to vent the chambers in the event that a TMP throws an error signal or a chamber goes above the low vacuum setpoint (200 mTorr). If armed and one of these events occurs, the PLC will log this error and begin venting every chamber in the system.

Finally, it is worth reviewing the procedure for baking out the Detector chamber. Before attempting to back-out the system, the user should ensure the following:

- The system is sealed, and the turbo pump is on.

- Any samples from the chamber that should not be baked-out are removed.

To start the default bake-out procedure, as is described in 2.3.4, simply turn on the power switch that is connected to the three temperature controllers. They are set to start the ramp/soak cycle as soon as they are powered.

Additional tips, guidelines, and best practices:

- A pumpdown process can be terminated by pressing the corresponding PUSH TO VENT button at any time.

- A venting process can similarly be terminated at any time by pressing the same button again.

- If a venting process is terminated the user must push PRESS TO START to turn the TMPs on again.

- Make sure the water filters for chilled water lines are changed routinely (every 6 months).

- If TMPs are to be off for more than a day, close the water valves.

- The Detector chamber should be at least at rough vacuum or purged with nitrogen when possible to protect the MCPs.

Appendix B
Piezo Valve Testing

B.1 Overview

In order to maximize the interaction pressure of xenon gas for HHG, while simultaneously reducing the total gas throughput, a high repetition rate, piezo actuated gas valve from Amsterdam Piezo Valve was used for these SFS experiments [12, 51]. The model ACPV3 was selected with a 500 μm opening diameter and 5mm nipple length in order to place the laser focus as close as possible to the gas output. This model has a variable pulse duration from 20 to 400 μs, in addition to a continuous mode of operation. In corresponding with the manufacturer it was determined that this experimental campaign was one of the first uses of this valve for the purpose of HHG. For this reason, the performance of the valve was thoroughly tested prior to committing to the design of the vacuum apparatus described in Chapter 2. For all these tests a fixed voltage of 140 V, the maximum the ACPV3's controller could provide at the time, was used to switch the valve open and close. The results of these diagnostic tests are reported below.

B.1.1 My Contributions

I was responsible for collecting and analyzing all of the data presented in this appendix. Bryan Smith assisted me in realigning the spectrometer and collecting the data.

B.2 HHG Test Stand

The valve was tested using a vacucum system connected to an XUV spectrometer, Hettrick Model SXR-II; Ser. No. 02, coupled to an Charge-Coupled Device camera, Andor Model

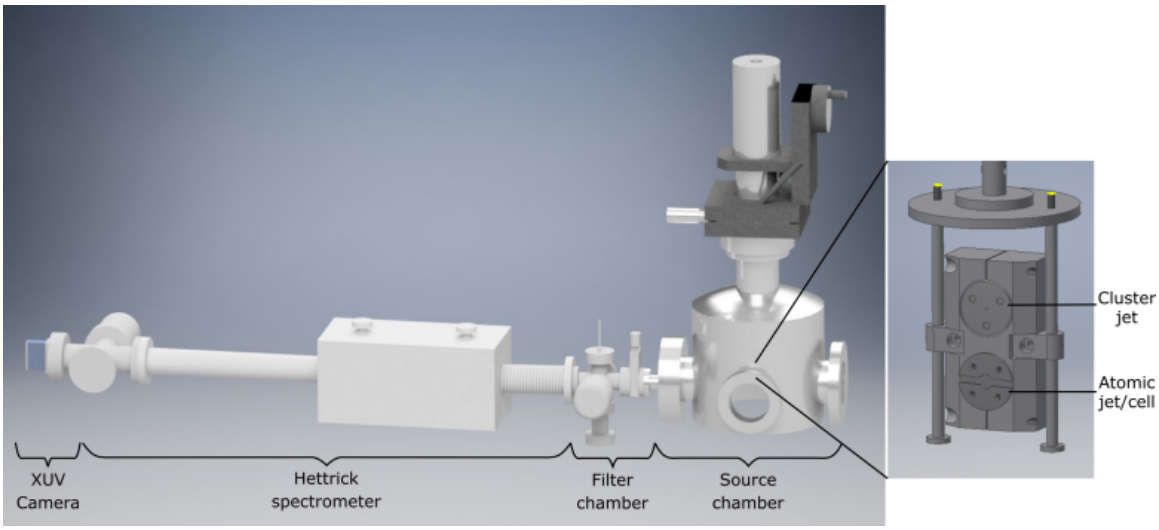

Figure B.1: The test stand used to evaluate the piezo valve

The armature supporting the gas valve was replaced with a custom mount to support the ACPV3 model piezo valve. An aluminum filter removed residual NIR light, after HHG, before transmission through the spectrometer. Adapted from [107].

DO440-BN, shown in Figure B.1. The Hettrick spectrometer has multiple gratings, these measurements utilized Grating D with 22.2 grooves/mm and a blaze wavelength of 40.5 nm, corresponding to a photon energy of 30.6 eV. An 200 nm aluminum foil was used to remove the residual NIR light after HHG. More details on the apparatus can be found in Zhou Wang's dissertation [107]. The pulsed operation of the gas valve was controlled by a TTL signal from a variable delay generator triggered by a photodiode out of vacuum.

The light source was a Ti:Sapphire laser, custom built by members of the DiMauro group, coupled to a HE-TOPAS from Light Conversion [20]. The output pulse had a duration of 60 fs, 1 mJ pulse energy, 1.7 μm carrier wavelength, and was delivered at a 1 kHz repetition rate. More details on this laser system can be found in Tim Gorman's dissertation [43]. The laser pulse was focused by a lens 25 cm outside the vacuum system.

B.3 Gas Throughput

The first tests evaluated the total gas throughput as a function of backing pressure for several different gas samples and valve pulse durations. Argon, xenon, and carbon dioxide

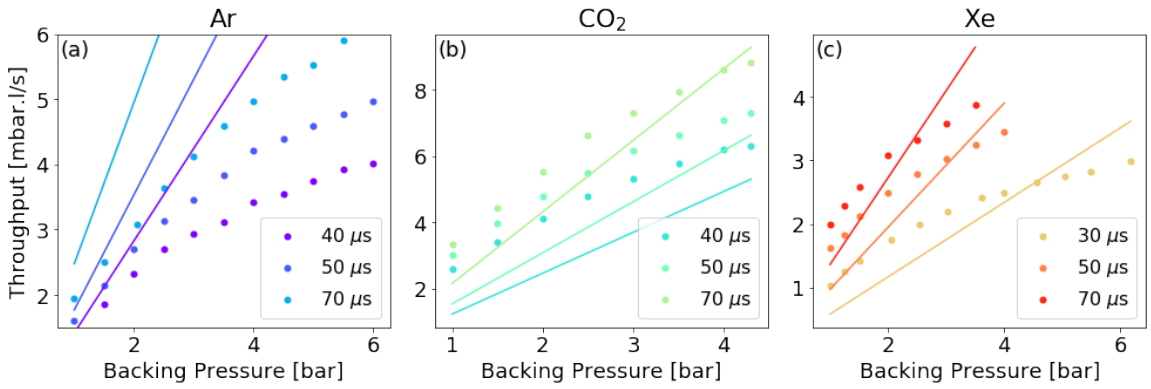

Figure B.2: Gas throughput versus backing pressure

The measured throughput is plotted with individual markers, and the lines are from the model of a continuous flowing jet with an applied duty cycle. (a) Argon. (b) Carbon Dioxide. (c) Xenon.

were used for pulse durations ranging from 30 to 70 mus, at a repetition rate of 1 kHz. The gas throughput was measured by taking the increase in foreline pressure, compared to when the valve was closed, and multiplied by pumping speed of the vacuum pump, a Varian Model SD-700. In addition, a prediction based on the gas throughput from a continuous flowing supersonic nozzle multiplied by the duty cycle was made. These results are presented in Figure B.2.

For xenon and carbon dioxide the throughput was within 30% of the expectation from the continuous flow model, however argon was significantly lower. The nonlinear increase in chamber pressure with valve backing pressure suggests that the ability for the valve to fully open is impaired by the increase in backing pressure. In principle, this could be alleviated by driving the piezo at a higher voltage with an increased risk of damaging the valve mechanism. Since these tests were conducted a software update has raised the maximum voltage to 200 V, for which the gas flow at a fixed backing pressure is increased.

B.4 Pulse Duration

The next tests studied the effective pulse duration of the gas valve by studying the total XUV yield as a function of delay between the laser and gas pulses. Figure B.3 shows the

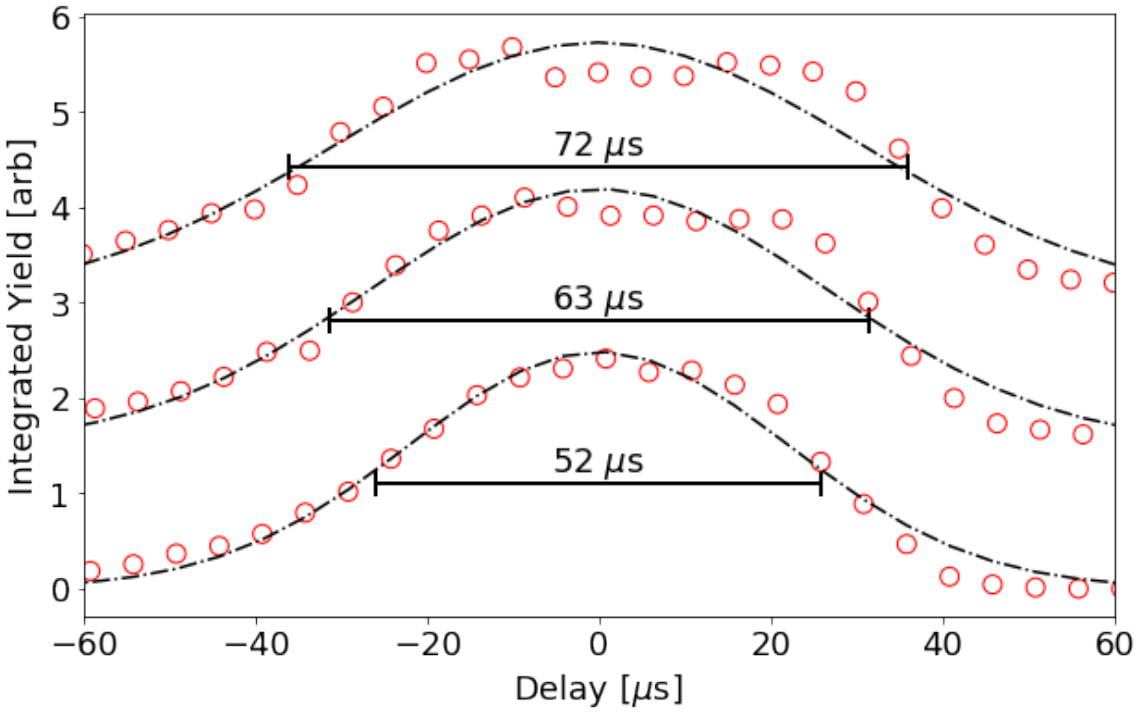

Figure B.3: XUV yield versus delay between the laser and gas pulses

In ascending order the voltage gate duration was 50, 60, and 70 μs. Each curve was shifted from the previous by a false offset of 1.5 units for visual clarity. The red circles are the measured values, and the grey dash dotted curves are the fitted gaussians. The FWHM of the fitted gaussians are reported.

results of these delay scans for three pulse durations for the voltage gate that opens the valve: 50, 60, and 70 μs. The gas target was xenon with a backing pressure of 2.2 bar in absolute units. The results are fitted to a gaussian function and the FWHM was extracted to determine the effective pulse durations. Overall, the valve functions as expected with effective pulse durations only 2-3 μs longer than the applied voltage gate.

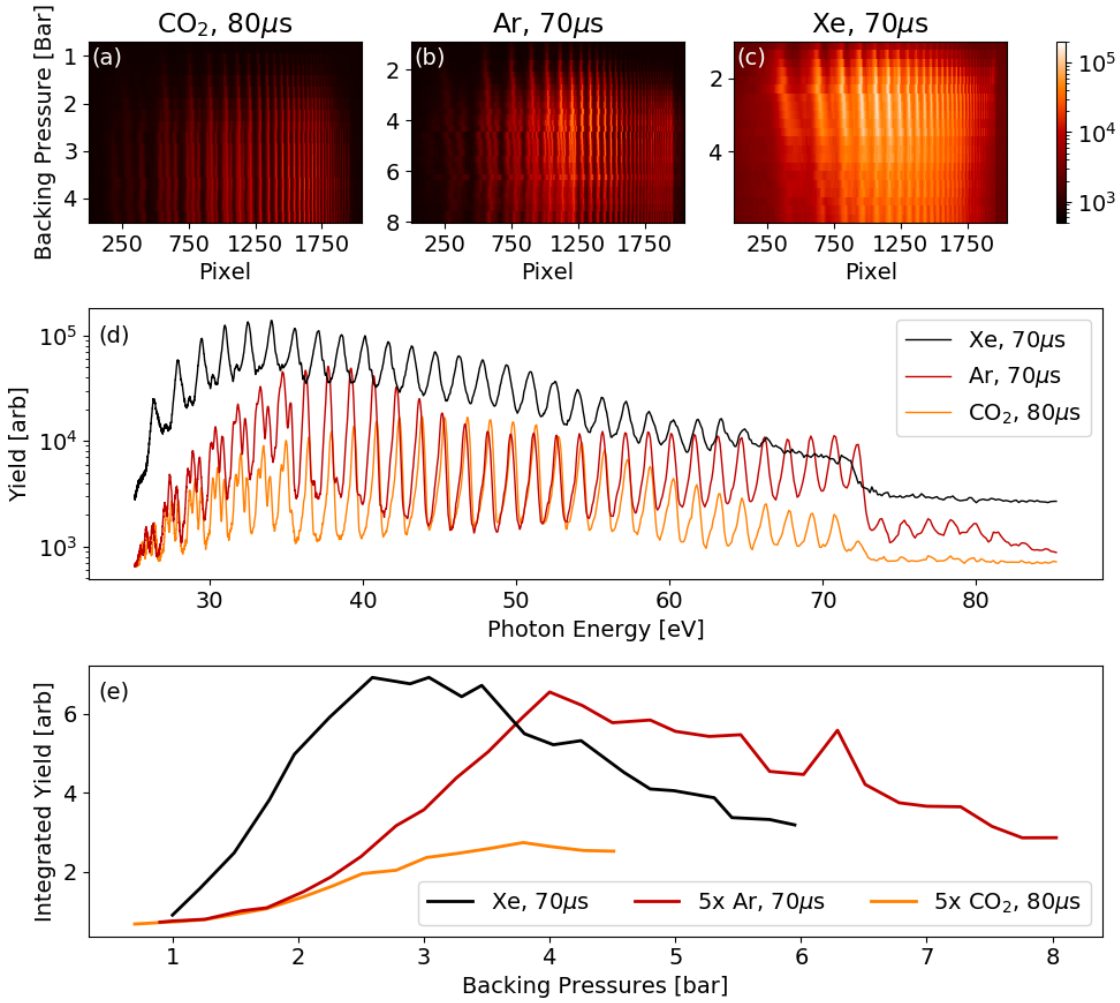

Figure B.4: XUV yield versus backing pressure

Panels (a-c) show the XUV yield versus pixel number for a range of backing pressures for a fixed target species and pulse duration. Panel (d) shows lineouts, with pixel number converted to photon energy, for the backing pressure which maximized total yield for each species. Panel (e) plots the total XUV yield versus backing pressure. The results for Ar and CO_2 were multiplied by 5 for ease of viewing on a linear ordinate.

B.5 Optimal Phase Matching

Finally, Figure B.4 shows the yield of XUV light with increasing backing pressure for fixed pulse duration and target species. Each target was able to optimally phase match for different parts of the spectrum between 25 and 75 eV, see discussion in Section 3.2. Xenon favored the lowest order harmonics observed, carbon dioxide the center of the spectrum at 50 eV, and argon near 40 eV with some revival at 70 eV. However, HHG in xenon produced significantly more XUV light than the other gases tested, as expected based on its lower Ip. Based on these results, xenon was selected as the target gas and the vacuum apparatus was designed to accommodate a gas throughput of several $\frac{mbar \cdot l}{s}$.

Appendix C
Neon Experiments

C.1 Overview

Neon was an additional atomic target used in this campaign of the SFS. The results collected with neon represents an intermediate between the extremes of the helium and argon experiments. With an Ip of 21.56 eV, only 3 eV below that of helium, the SFS condition of launching low kinetic energy electron wavepackets was nearly fulfilled. Analogous features from both the helium and argon experiments could be observed in neon such as the feature at low kinetic energies, significant enhancements in the electron yield, and the disappearance of the π phase shift in the phase of oscillation with increasing field strength. As such, these results are included in this appendix with minimal discussion, highlighting the relevant sections in Chapters 4 and 5 which examine the relevant features observed.

C.1.1 My Contributions

I was responsible for collecting and analyzing all of the data presented in this appendix. I developed the software to run the SFA simulations of the photoelectron data. Qiaoyi Liu assisted me in collecting the data, and running simulations.

C.2 Ion Data

Figure C.1 shows the yield of different ion species. Atmospheric contaminants - namely N_2, O_2, and H_2O - are the dominant species for intensities of 90 TW/cm^2 or greater, setting an upper bound on the viable intensities for studies of the photoelectron spectrograms. The yield for when the XUV and NIR fields are combined shows an insignificant increase in the

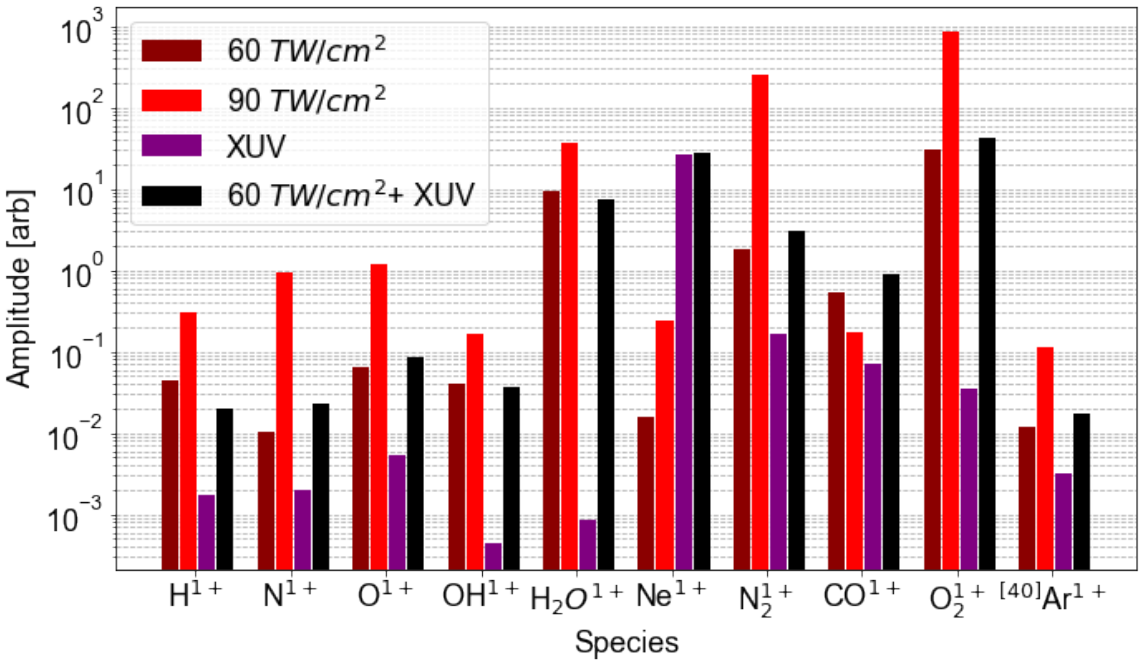

Figure C.1: Relative abundance of ion species, neon experiments

Relative abundance of the prevalent ion species after ionization for four conditions: the XUV light in isolation, the NIR light alone for two different intensities, 60 and 90 TW/cm^2, and the XUV and NIR light combined. The SFS condition is met for neon, where the majority of ionization is due to the XUV pulse. Based on this data, the presence of atmospheric contaminants will be limiting for photoelectron studies with NIR intensities greater than 60 TW/cm^2.

yield of neon single ions. As such, it is assumed that there is no two color mechanism for single ionization as seen in helium, where the harmonics with energies below the Ip could excite electrons which were subsequently ionized by the NIR field. Brief experiments were conducted to observe an enhancement in the rate of double ionization as observed in helium and argon but was unsuccessful. More rigorous experiments with longer integration times than used here are likely required to make this observation of XUV seeded NSDI.

C.3 Photoelectron Data

Figures C.2-C.5 show spectrograms collected across 4 orders of magnitude of NIR intensity. Similar to argon, at the lowest intensities a π phase shift is observed in the phase of the 1ω

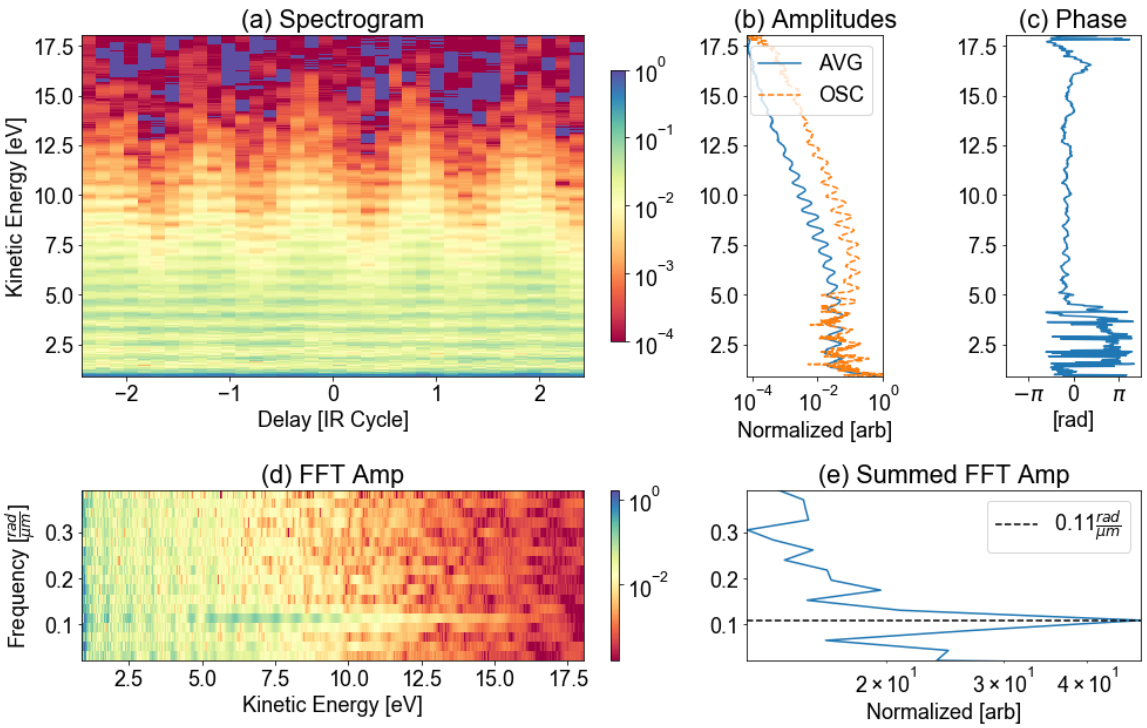

Figure C.2: Photoelectron spectrogram, neon target, $< 1TW/cm^2$

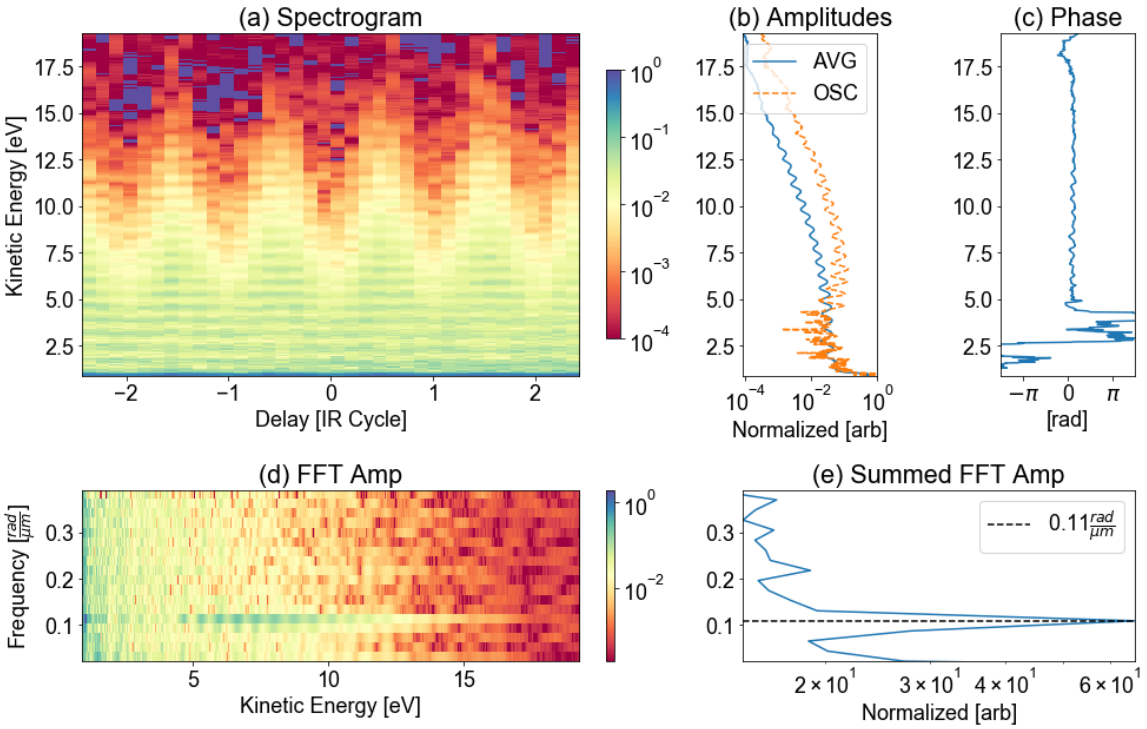

Figure C.3: Photoelectron spectrogram, neon target, $2TW/cm^2$

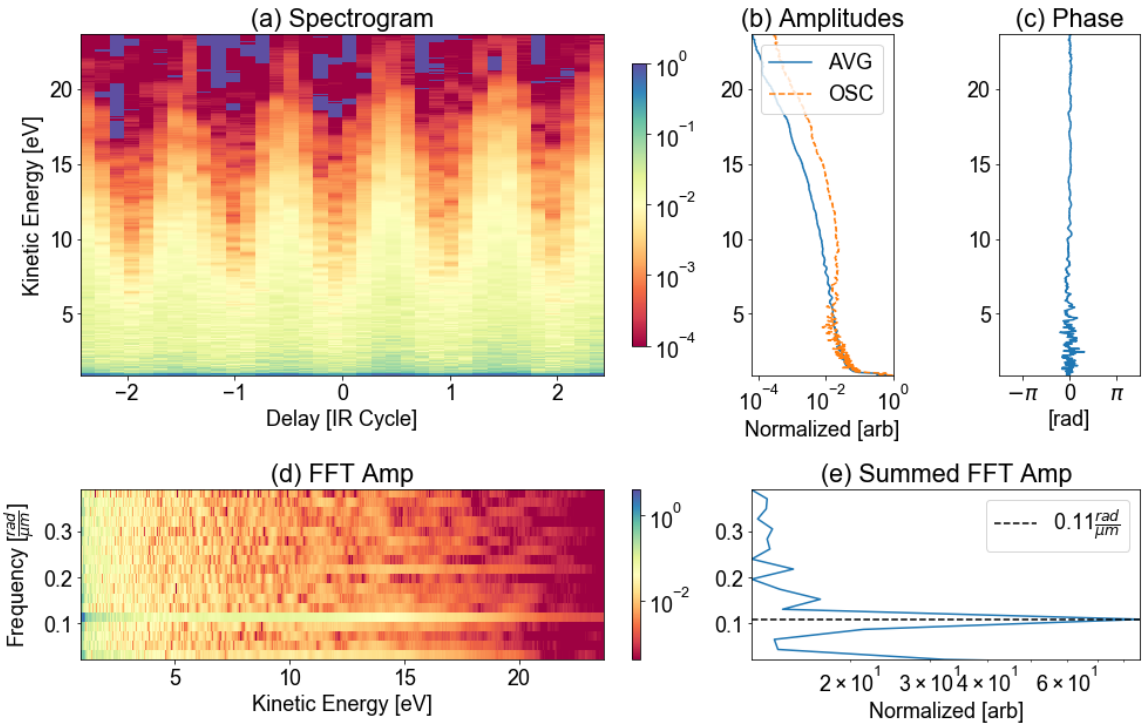

Figure C.4: Photoelectron spectrogram, neon target, $8TW/cm^2$

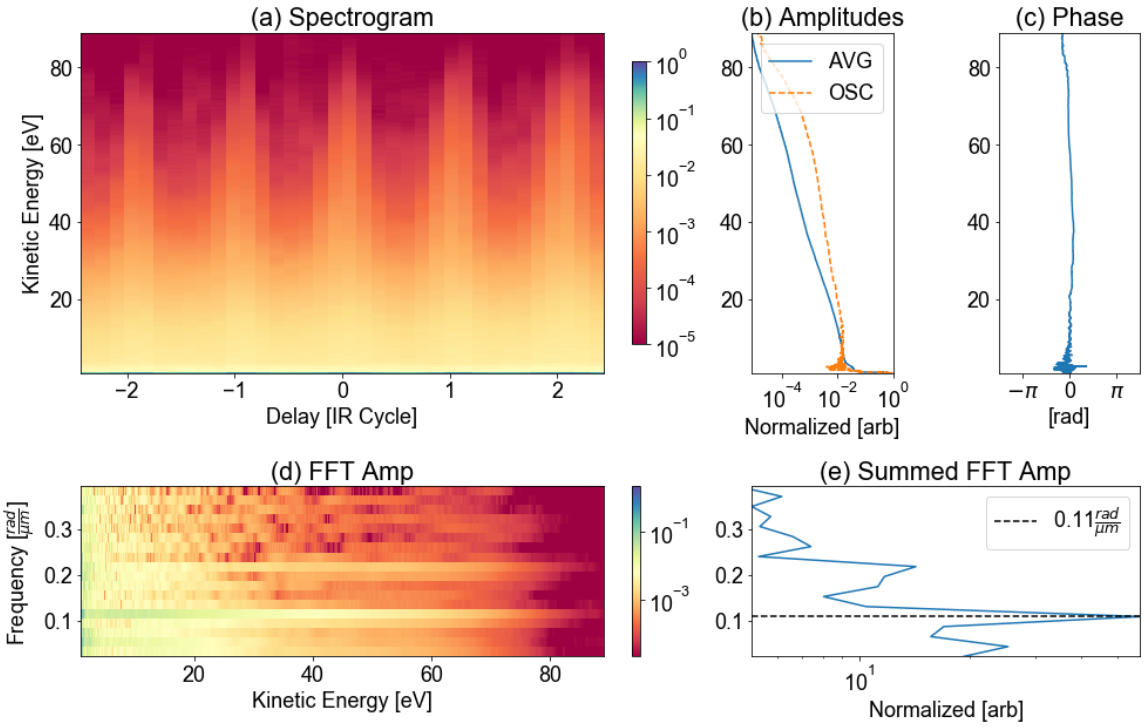

Figure C.5: Photoelectron spectrogram, neon target, $90TW/cm^2$

oscillation associated with a typical streaking experiment. As expected from the analysis in Section 5.4, this phase shift vanishes at a lower intensity in neon than argon, compare the results at 8 TW/cm^2 for neon in Figure C.4 to 15 TW/cm^2 for argon in panels (e-f) of Figure 5.11, corresponding to the lower mean kinetic energy of the electron wavepacket.

Figure C.6 shows the extracted lineouts from a spectrogram taken with NIR intensity of 75 TW/cm^2 which can be compared to Figures 4.8 and 5.8. Similar to helium, though lesser in magnitude, a significant enhancement in the total photoelectron yield is observed and attributed to the focusing effect of the NIR field, see the discussion at the end of Section 4.3.1. Again, no recollision events at large kinetic energies could be observed due to the significant yield of ATI from contaminant species. A set of difference lineouts are shown in Figure C.7 showing the effects of increasing NIR intensities on the photoelectron distribution. Figure C.8 shows the scalings of various features with Up and NIR intensity. Comparing to the results in helium, see Figure 4.10, the *enhancement* has a slope and total magnitude $\sim$ 4x smaller in neon. The slope of the *CoM* is nearly identical to within the fitting errors. The slope of the *cutoff* is between the values observed in helium and argon, 2.06 and 3.13 respectively. It seems likely that this slope is sensitive to the mean electron kinetic energy at ionization, and should approach the results of the "Simpleman's Theory" as it approaches 0 (when the mean photon energy equals the atomic Ip). The ratio of *Signal-to-ATI* shows some disagreement with the results of the ion yield data in Figure C.1, and that at an intensity of 90 TW/cm^2 the results are dominated by the NIR ionization of contaminant species. This can be attributed to the role of the focusing effect increasing the detection efficiency of electrons ionized by the XUV.

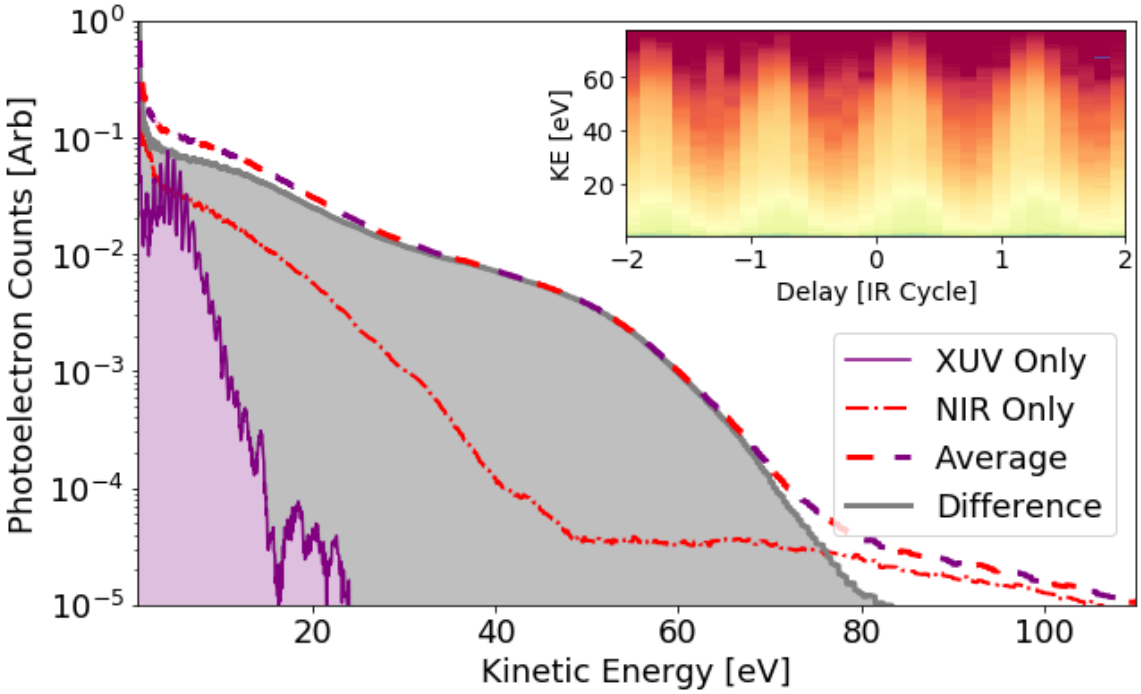

Figure C.6: Lineouts from spectrogram, neon target, $75 TW/cm^2$

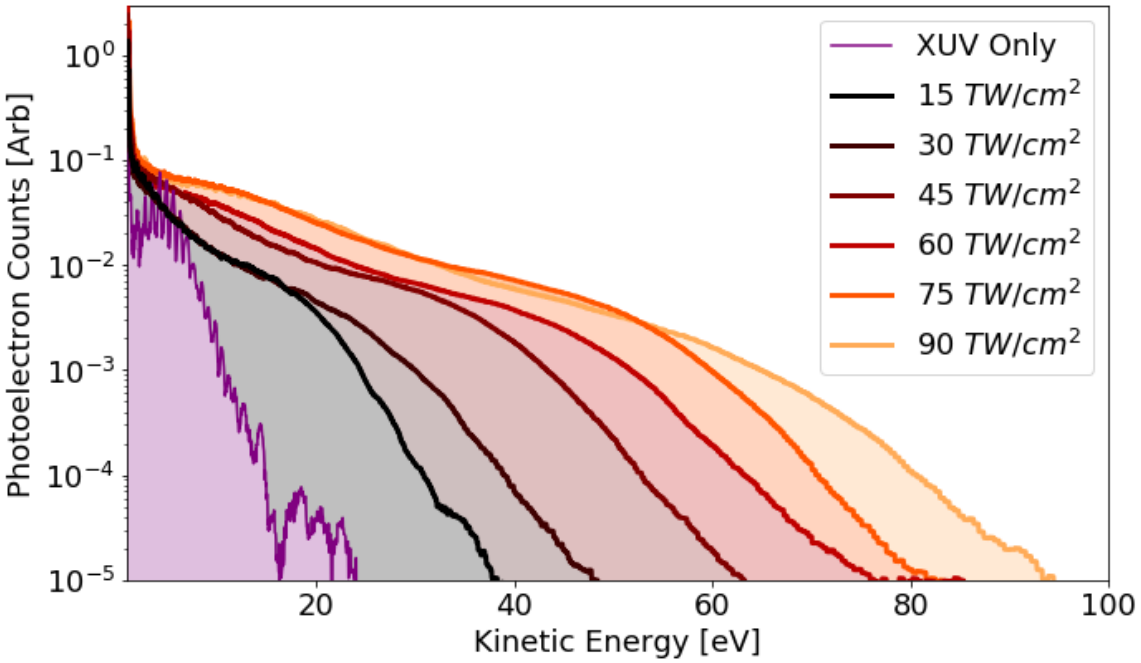

Figure C.7: 2-Color photoelectron yields for various NIR intensities, neon target

Each curve is the difference between the spectrogram average and the NIR only spectra. These can be directly compared for relative increases in yield.

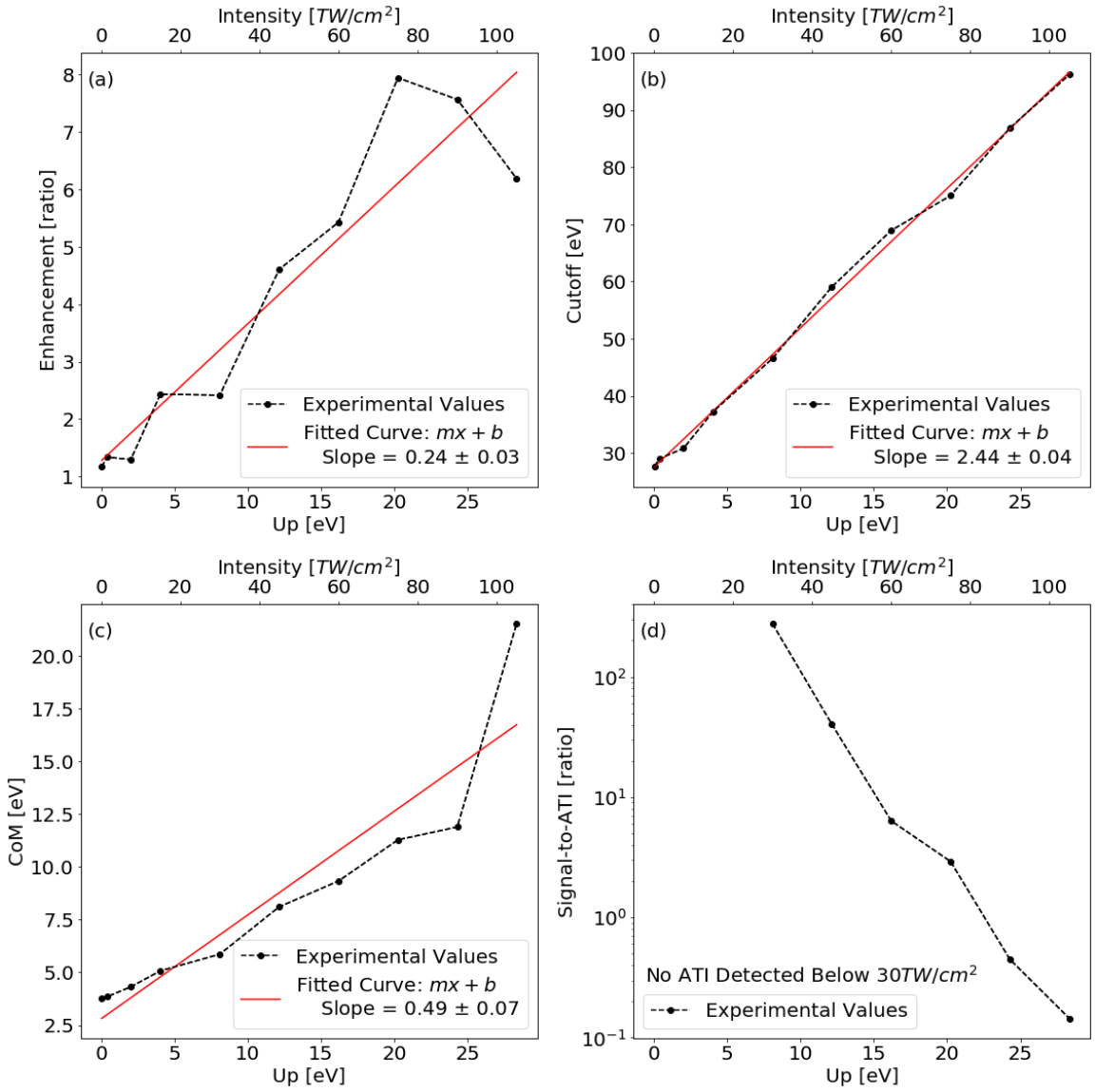

Figure C.8: SFS feature scaling in neon photoelectrons

See Equations 4.3 - 4.6 for definitions of the ordinate in each subplot.

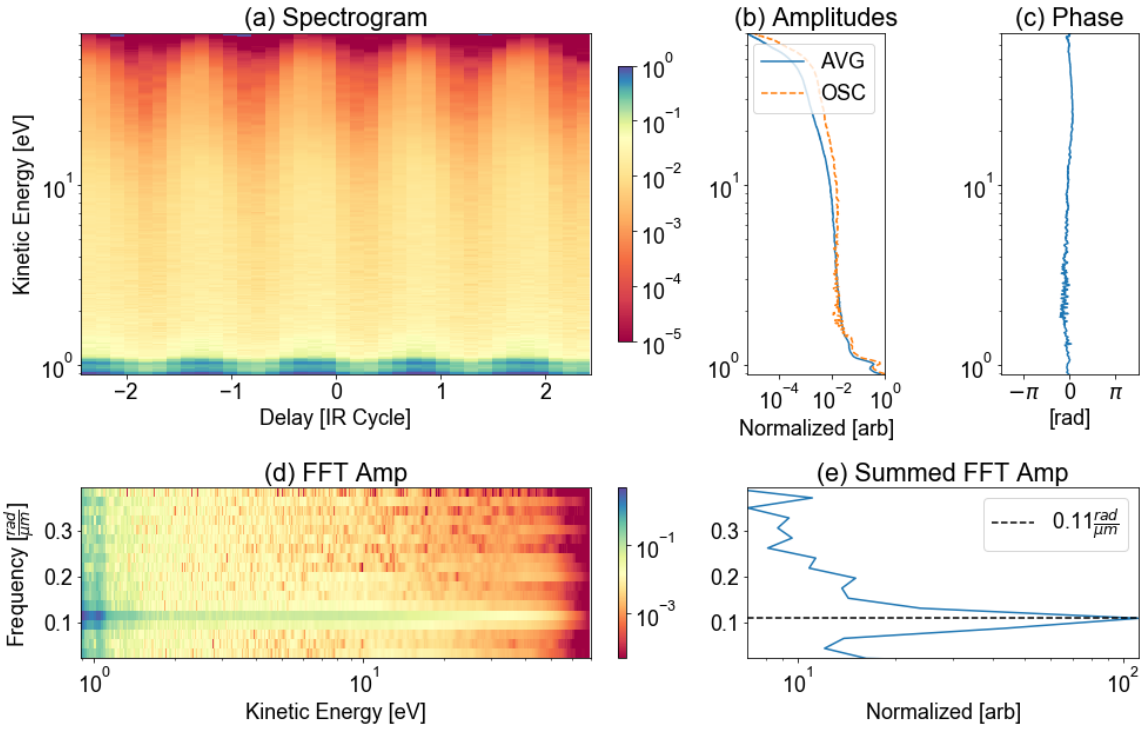

Figure C.9: Photoelectron spectrogram, neon target, $60 TW/cm^2$, semi-log scale

A feature at low electron energies is observed in neon similar to helium, see Section 4.3.4. Figure C.9 shows a spectrogram using a logarithmic kinetic energy axis, highlighting the maxima in yield near 1 eV that oscillates in phase with the higher energy electrons. Figure C.10 shows the scaling of this low energy feature with increasing intensity. The difference in energy at which the feature appears, 1 eV in neon versus 1.6 eV in helium, is significant. The results of Zhang et al. suggest that the peak energy of the LES is independent of atomic species, and instead is a function of solely Up and the NIR pulse duration [110]. This change in energy from helium to neon casts some doubt on this assignment as a recollision driven LES. However, in these SFS experiments, the role of the changing mean kinetic energy of the electron wavepacket with decreasing atomic Ip may influence the position of this peak, explaining this discrepancy.

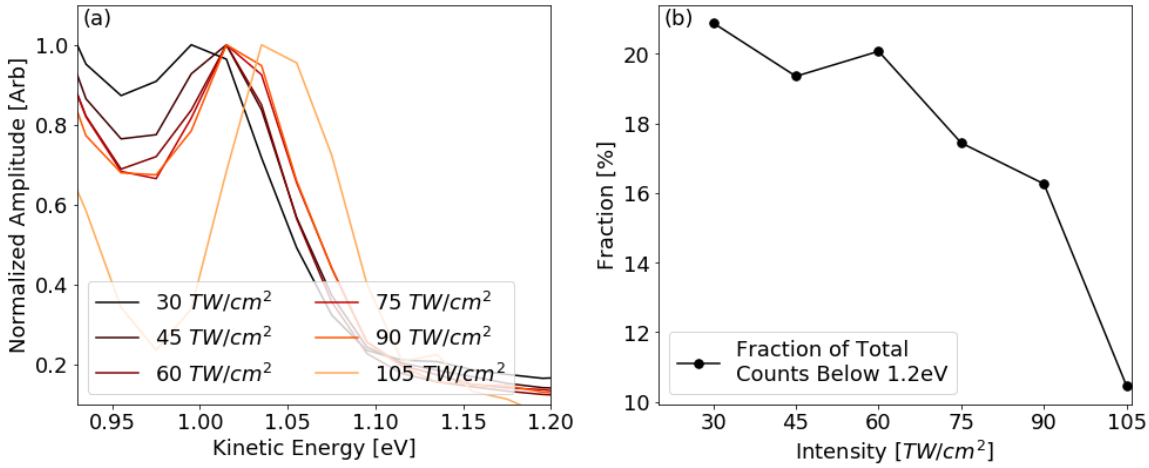

Figure C.10: Low energy feature scaling in neon

(a) difference spectra normalized to the maximum photoelectron amplitude within each spectra. (b) the fraction of the total photolectron signal in the difference spectra contained below 1.2 eV.

Bibliography

[1] V. V. AG. Uhv gate valve, series 108, dn 63 (id $2\frac{1}{2}$") technical data. Online, 1 2016. See VAT45data.pdf.

[2] P. Agostini, F. Fabre, G. Mainfray, G. Petite, and N. K. Rahman. Free-free transitions following six-photon ionization of xenon atoms. *Phys. Rev. Lett.*, 42:1127–1130, Apr 1979.

[3] C. Altucci, R. Velotta, E. Heesel, E. Springate, J. P. Marangos, C. Vozzi, E. Benedetti, F. Calegari, G. Sansone, S. Stagira, M. Nisoli, and V. Tosa. High-order harmonic generation in alkanes. *Phys. Rev. A*, 73:043411, Apr 2006.

[4] K. Amini, J. Biegert, F. Calegari, A. Chacón, M. F. Ciappina, A. Dauphin, D. K. Efimov, C. F. de Morisson Faria, K. Giergiel, P. Gniewek, A. S. Landsman, M. Lesiuk, M. Mandrysz, A. S. Maxwell, R. Moszyński, L. Ortmann, J. A. Pérez-Hernández, A. Picón, E. Pisanty, J. Prauzner-Bechcicki, K. Sacha, N. Suárez, A. Zaïr, J. Zakrzewski, and M. Lewenstein. Symphony on strong field approximation. *Reports on Progress in Physics*, 82(11):116001, oct 2019.

[5] M. V. Ammosov, N. B. Delone, and V. P. Krainov. Tunnel Ionization Of Complex Atoms And Atomic Ions In Electromagnetic Field. In J. A. Alcock, editor, *High Intensity Laser Processes*, volume 0664, pages 138 – 141. International Society for Optics and Photonics, SPIE, 1986.

[6] V. Antonov, L. Bekenov, and A. Yaresko. Electronic structure of strongly correlated systems. *Advances in Condensed Matter Physics*, 2011, Dec 2011.

[7] P. Balcou, A. S. Dederichs, M. B. Gaarde, and A. L'Huillier. Quantum-path analysis and phase matching of high-order harmonic generation and high-order frequency mixing processes in strong laser fields. *Journal of Physics B: Atomic, Molecular and Optical Physics*, 32(12):2973–2989, jan 1999.

[8] J. Biegert, A. Heinrich, C. P. Hauri, W. Kornelis, P. Schlup, M. P. Anscombe, M. B. Gaarde, K. J. Schafer, and U. Keller. Control of high-order harmonic emission using attosecond pulse trains. *Journal of Modern Optics*, 53(1-2):87–96, 2006.

[9] C. Blaga, F. Catoire, P. Colosimo, G. Paulus, H. Muller, P. Agostini, and D. L.F. Strong-field photoionization revisited. *Nature Physics*, 5:335–338, Mar 2009.

[10] R. W. Boyd. Chapter 2 - wave-equation description of nonlinear optical interactions. In R. W. Boyd, editor, *Nonlinear Optics (Third Edition)*, pages 69–133. Academic Press, Burlington, third edition edition, 2008.

[11] I. Buluta and F. Nori. Quantum simulators. *Science*, 326(5949):108–111, 2009.

[12] M. BV. Amsterdam cantilever piezo valve user manual. Online, 7 2018. See APV-Manual.pdf.

[13] Z. Chang. Controlling attosecond pulse generation with a double optical gating. *Phys. Rev. A*, 76:051403, Nov 2007.

[14] Z. Chang. *Fundamentals of attosecond optics*. CRC Press, Boca Raton, Fla., first edition, 2011.

[15] C. Chen, C. Hernández-García, Z. Tao, W. You, Y. Zhang, D. Zusin, C. Gentry, P. Tengdin, A. Becker, A. Jaron-Becker, H. Kapteyn, and M. Murnane. Influence of microscopic and macroscopic effects on attosecond pulse generation using two-color laser fields. *Opt. Express*, 25(23):28684–28696, Nov 2017.

[16] S. L. Chin, F. Yergeau, and P. Lavigne. Tunnel ionisation of xe in an ultra-intense CO2laser field (1014w cm-2) with multiple charge creation. *Journal of Physics B: Atomic and Molecular Physics*, 18(8):L213–L215, apr 1985.

[17] M. Chini, S. Gilbertson, S. D. Khan, and Z. Chang. Characterizing ultrabroadband attosecond lasers. *Opt. Express*, 18(12):13006–13016, Jun 2010.

[18] M. Chini, H. Mashiko, H. Wang, S. Chen, C. Yun, S. Scott, S. Gilbertson, and Z. Chang. Delay control in attosecond pump-probe experiments. *Opt. Express*, 17(24):21459–21464, Nov 2009.

[19] K. J. L. Company. Kjl615tc k/h technical data. Online, 3 2020. Date of Retrieval, See kjl615tckTechnicalData.pdf.

[20] L. Conversion. Topas. Online, 1 2005. See MaiTaiSPDatasheet.pdf.

[21] P. B. Corkum. Plasma perspective on strong field multiphoton ionization. *Phys. Rev. Lett.*, 71:1994–1997, Sep 1993.

[22] E. K. Damon and R. G. Tomlinson. Observation of ionization of gases by a ruby laser. *Appl. Opt.*, 2(5):546–547, May 1963.

[23] P. Dietrich, N. H. Burnett, M. Ivanov, and P. B. Corkum. High-harmonic generation and correlated two-electron multiphoton ionization with elliptically polarized light. *Phys. Rev. A*, 50:R3585–R3588, Nov 1994.

[24] A. Direct. C-more micro 4-inch ea3 touch panel technical data. Online, 3 2018. Date of Retrieval, See cmoreTechnicalData.pdf.

[25] A. Direct. Solo temperature controllers $\frac{1}{16}$ din technical data. Online, 3 2018. Date of Retrieval, See SOLOTechnicalData.pdf.

[26] A. Direct. Ethernet basic plc manual. Online, 3 2020. Date of Retrieval, See click-PLCTechnicalData.pdf.

[27] M. Drescher, M. Hentschel, R. Kienberger, G. Tempea, C. Spielmann, G. A. Reider, P. B. Corkum, and F. Krausz. X-ray pulses approaching the attosecond frontier. *Science*, 291(5510):1923–1927, 2001.

[28] Edwards. Pv25pka technical data. Online, 3 2020. Date of Retrieval, See edwards25TechnicalData.pdf.

[29] Edwards. Pv40pka technical data. Online, 3 2020. Date of Retrieval, See edwards40TechnicalData.pdf.

[30] A. Einstein. Über einen die erzeugung und verwandlung des lichtes betreffenden heuristischen gesichtspunkt. *Annalen der Physik*, 17(6):132–148, 1905.

[31] F. H. M. Faisal. Multiple absorption of laser photons by atoms. *Journal of Physics B: Atomic and Molecular Physics*, 6(4):L89–L92, apr 1973.

[32] U. Fano. Effects of configuration interaction on intensities and phase shifts. *Phys. Rev.*, 124:1866–1878, Dec 1961.

[33] R. Feynman, J. Hollingsworth, M. Vennettilli, T. Budner, R. Zmiewski, D. P. Fahey, T. J. Carroll, and M. W. Noel. Quantum interference in the field ionization of rydberg atoms. *Phys. Rev. A*, 92:043412, Oct 2015.

[34] C. Figueira de Morisson Faria and X. Liu. Electron–electron correlation in strong laser fields. *Journal of Modern Optics*, 58(13):1076–1131, 2011.

[35] D. N. Fittinghoff, P. R. Bolton, B. Chang, and K. C. Kulander. Observation of nonsequential double ionization of helium with optical tunneling. *Phys. Rev. Lett.*, 69:2642–2645, Nov 1992.

[36] D. N. Fittinghoff, P. R. Bolton, B. Chang, and K. C. Kulander. Polarization dependence of tunneling ionization of helium and neon by 120-fs pulses at 614 nm. *Phys. Rev. A*, 49:2174–2177, Mar 1994.

[37] P. A. Franken, A. E. Hill, C. W. Peters, and G. Weinreich. Generation of optical harmonics. *Phys. Rev. Lett.*, 7:118–119, Aug 1961.

[38] M. B. Gaarde, K. J. Schafer, A. Heinrich, J. Biegert, and U. Keller. Large enhance-

ment of macroscopic yield in attosecond pulse train–assisted harmonic generation. *Phys. Rev. A*, 72:013411, Jul 2005.

[39] G. Gademann, F. Kelkensberg, W. K. Siu, P. Johnsson, M. B. Gaarde, K. J. Schafer, and M. J. J. Vrakking. Attosecond control of electron–ion recollision in high harmonic generation. *New Journal of Physics*, 13(3):033002, mar 2011.

[40] T. F. Gallagher. Above-threshold ionization in low-frequency limit. *Phys. Rev. Lett.*, 61:2304–2307, Nov 1988.

[41] T. Gaumnitz, A. Jain, Y. Pertot, M. Huppert, I. Jordan, F. Ardana-Lamas, and H. J. Wörner. Streaking of 43-attosecond soft-x-ray pulses generated by a passively cep-stable mid-infrared driver. *Opt. Express*, 25(22):27506–27518, Oct 2017.

[42] K. Gawlas and S. D. Hogan. Rydberg-state ionization dynamics and tunnel ionization rates in strong electric fields. *Phys. Rev. A*, 99:013421, Jan 2019.

[43] T. Gorman. *Attosecond probing of electron dynamics in atoms and molecules using tunable mid-infrared drivers.* PhD thesis, Ohio State University, 1224 Kinnear Road Columbus, OH 43212, 11 2019.

[44] J. Grant-Jacob, B. Mills, T. J. Butcher, R. T. Chapman, W. S. z Brocklesby, and J. G. Frey. Gas jet structure influence on high harmonic generation. *Opt. Express*, 19(10):9801–9806, May 2011.

[45] Granville-Phillips. Series 307 vacuum gauge controller. Print, 7 1990.

[46] S. M. Hankin, D. M. Villeneuve, P. B. Corkum, and D. M. Rayner. Intense-field laser ionization rates in atoms and molecules. *Phys. Rev. A*, 64:013405, Jun 2001.

[47] B. Henke, E. Gullikson, and J. Davis. X-ray interactions: Photoabsorption, scattering, transmission, and reflection at e = 50-30,000 ev, z = 1-92. *Atomic Data and Nuclear Data Tables*, 54(2):181–342, 1993.

[48] H. Hertz. Über einen einfluss des ultravioletten lichtes auf die electrische entladung. *Annalen der Physik*, 267(8):983–1000, Jun 1887.

[49] M. Huppert, I. Jordan, and H. J. Wörner. Attosecond beamline with actively stabilized and spatially separated beam paths. *Review of Scientific Instruments*, 86(12):123106, 2015.

[50] K. Hütten, M. Mittermair, S. Stock, R. Beerwerth, V. Shirvanyan, J. Riemensberger, A. Duensing, R. Heider, M. Wagner, A. Guggenmos, S. Fritzsche, N. Kabachnik, R. Kienberger, and B. Bernhardt. Ultrafast quantum control of ionization dynamics in krypton. *Nat. Commun.*, 9:719, Feb 2018.

[51] D. Irimia, D. Dobrikov, R. Kortekaas, H. Voet, D. A. van den Ende, W. A. Groen, and M. H. M. Janssen. A short pulse (7μs fwhm) and high repetition rate (dc-5khz) cantilever piezovalve for pulsed atomic and molecular beams. *Review of Scientific Instruments*, 80(11):113303, 2009.

[52] J. Itatani, F. Quéré, G. L. Yudin, M. Y. Ivanov, F. Krausz, and P. B. Corkum. Attosecond streak camera. *Phys. Rev. Lett.*, 88:173903, Apr 2002.

[53] W. Kaiser and C. G. B. Garrett. Two-photon excitation in caf$_2$: eu^{2+}. *Phys. Rev. Lett.*, 7:229–231, Sep 1961.

[54] A. Kaldun, A. Blättermann, V. Stooß, S. Donsa, H. Wei, R. Pazourek, S. Nagele, C. Ott, C. D. Lin, J. Burgdörfer, and T. Pfeifer. Observing the ultrafast buildup of a fano resonance in the time domain. *Science*, 354(6313):738–741, 2016.

[55] A. Kästner, U. Saalmann, and J. M. Rost. Electron-energy bunching in laser-driven soft recollisions. *Phys. Rev. Lett.*, 108:033201, Jan 2012.

[56] S. Kazamias, S. Daboussi, O. Guilbaud, K. Cassou, D. Ros, B. Cros, and G. Maynard. Pressure-induced phase matching in high-order harmonic generation. *Phys. Rev. A*, 83:063405, Jun 2011.

[57] S. Kazamias, F. Weihe, D. Douillet, C. Valentin, T. Planchon, S. Sebban, G. Grillon, F. Augé, D. Hulin, and P. Balcou. Gas jet structure influence on high harmonic generation. *Eur. Phys. J. D*, 21:353–359, December 2002.

[58] L. Keldysh. Ionization in the field of a strong electromagnetic wave. *Zh. Eksp. Teor. Fiz.*, 47:1945 – 1957, Nov 1964.

[59] D. Kiesewetter. *Dynamics of near-threshold, attosecond electron wavepackets in strong laser fields*. PhD thesis, Ohio State University, 1224 Kinnear Road Columbus, OH 43212, 11 2019.

[60] D. Kiesewetter, R. Jones, A. Camper, S. Schoun, P. Agostini, and L. DiMauro. Probing electronic binding potentials with attosecond photoelectron wavepackets. *Nature Phys*, 14:68–73, October 2018.

[61] K. Kimura, S. Katsuma, Y. Achiba, T. Yamazaki, and S. Iwata. *Handbook of HeI photoelectron spectra of fundamental organic molecules*. Japan Scientific Societies Press, 1 edition, 1981.

[62] M. Kotur, D. Guénot, A. Jiménex-Galán, D. Kroon, E. Larsen, M. Louisy, S. Bengtsson, M. Miranda, J. Mauritsson, C. Arnold, S. Canton, M. Gisselbrecht, T. Carette, J. Dahlström, E. Lindroth, A. Maquet, L. Argenti, F. Martín, and A. L'Huillier. Spectral phase measurement of a fano resonance using tunable attosecond pulses. *Nat. Commun.*, 7:10566, Feb 2016.

[63] A. Kramida, Yu. Ralchenko, J. Reader, and and NIST ASD Team. NIST Atomic Spectra Database (ver. 5.9), [Online]. Available: `https://physics.nist.gov/asd` [2022, March 2]. National Institute of Standards and Technology, Gaithersburg, MD., 2021.

[64] D. Krebs, S. Pabst, and R. Santra. Introducing many-body physics using atomic spectroscopy. *American Journal of Physics*, 82(2):113–122, 2014.

[65] P. Kruit, J. Kimman, H. G. Muller, and M. J. van der Wiel. Electron spectra from multiphoton ionization of xenon at 1064, 532, and 355 nm. *Phys. Rev. A*, 28:248–255, Jul 1983.

[66] A.-T. Le, R. R. Lucchese, S. Tonzani, T. Morishita, and C. D. Lin. Quantitative rescattering theory for high-order harmonic generation from molecules. *Phys. Rev. A*, 80:013401, Jul 2009.

[67] V. E. Leshchenko, B. K. Talbert, Y. H. Lai, S. Li, Y. Tang, S. J. Hageman, G. Smith, P. Agostini, L. F. DiMauro, and C. I. Blaga. High-power few-cycle cr:znse mid-infrared source for attosecond soft x-ray physics. *Optica*, 7(8):981–988, Aug 2020.

[68] M. Lewenstein, P. Balcou, M. Y. Ivanov, A. L'Huillier, and P. B. Corkum. Theory of high-harmonic generation by low-frequency laser fields. *Phys. Rev. A*, 49:2117–2132, Mar 1994.

[69] Leybold. Display one/display two, three. Online, 1 2005. Date of Retrieval, See LeyboldDisplayTechnicalData.pdf.

[70] Leybold. Ecodry 40 technical data. Online, 3 2020. Date of Retrieval, See EcoDry40TechnicalData.pdf.

[71] Leybold. Ecodry 65 technical data. Online, 3 2020. Date of Retrieval, See EcoDry65TechnicalData.pdf.

[72] Leybold. Penningvac ptr 90 n technical data. Online, 3 2020. Date of Retrieval, See PenningVacPTR90NTechnicalData.pdf.

[73] Leybold. Turbovac 450 i technical data. Online, 3 2020. Date of Retrieval, See TBVac450iTechnicalData.pdf.

[74] Leybold. Turbovac mag w 1300 ip technical data. Online, 3 2020. Date of Retrieval, See MAG1300TechnicalData.pdf.

[75] A. l'Huillier, L. A. Lompre, G. Mainfray, and C. Manus. Multiply charged ions induced by multiphoton absorption in rare gases at 0.53 μm. *Phys. Rev. A*, 27:2503–2512, May 1983.

[76] W. Lotz. Electron-impact ionization cross-sections and ionization rate coefficients for atoms and ions from hydrogen to calcium. *Z. Physik*, 216:241–247, 1968.

[77] T. Maiman. Stimulated optical radiation in ruby. *Nature*, 187:493–494, 1960.

[78] Y. Mairesse and F. Quéré. Frequency-resolved optical gating for complete reconstruction of attosecond bursts. *Phys. Rev. A*, 71:011401, Jan 2005.

[79] I. H. Malitson. Interspecimen comparison of the refractive index of fused silica∗,†. *J. Opt. Soc. Am.*, 55(10):1205–1209, Oct 1965.

[80] J. Mauritsson, P. Johnsson, E. Gustafsson, A. L'Huillier, K. J. Schafer, and M. B. Gaarde. Attosecond pulse trains generated using two color laser fields. *Phys. Rev. Lett.*, 97:013001, Jul 2006.

[81] J. Mauritsson, P. Johnsson, E. Mansten, M. Swoboda, T. Ruchon, A. L'Huillier, and K. J. Schafer. Coherent electron scattering captured by an attosecond quantum stroboscope. *Phys. Rev. Lett.*, 100:073003, Feb 2008.

[82] J. Mauritsson, T. Remetter, M. Swoboda, K. Klünder, A. L'Huillier, K. J. Schafer, O. Ghafur, F. Kelkensberg, W. Siu, P. Johnsson, M. J. J. Vrakking, I. Znakovskaya, T. Uphues, S. Zherebtsov, M. F. Kling, F. Lépine, E. Benedetti, F. Ferrari, G. Sansone, and M. Nisoli. Attosecond electron spectroscopy using a novel interferometric pump-probe technique. *Phys. Rev. Lett.*, 105:053001, Jul 2010.

[83] A. McPherson, G. Gibson, H. Jara, U. Johann, T. S. Luk, I. A. McIntyre, K. Boyer, and C. K. Rhodes. Studies of multiphoton production of vacuum-ultraviolet radiation in the rare gases. *J. Opt. Soc. Am. B*, 4(4):595–601, Apr 1987.

[84] J. Metje, F. Lever, D. Mayer, R. J. Squibb, M. S. Robinson, M. Niebuhr, R. Feifel,

S. Düsterer, and M. Gühr. Ursa-pq: A mobile and flexible pump-probe instrument for gas phase samples at the flash free electron laser. *Applied Sciences*, 10(21), 2020.

[85] D. R. Miller. Free Jet Sources (Chap 2). In G. Scoles, editor, *Atomic and Molecular Beam Methods*, volume 1, pages 14–82. Oxford University Press, 1988.

[86] T. Nubbemeyer, K. Gorling, A. Saenz, U. Eichmann, and W. Sandner. Strong-field tunneling without ionization. *Phys. Rev. Lett.*, 101:233001, Dec 2008.

[87] P. M. Paul, E. S. Toma, P. Breger, G. Mullot, F. Augé, P. Balcou, H. G. Muller, and P. Agostini. Observation of a train of attosecond pulses from high harmonic generation. *Science*, 292(5522):1689–1692, 2001.

[88] G. G. Paulus, W. Nicklich, H. Xu, P. Lambropoulos, and H. Walther. Plateau in above threshold ionization spectra. *Phys. Rev. Lett.*, 72:2851–2854, May 1994.

[89] T. Popmintchev, M.-C. Chen, A. Bahabad, M. Gerrity, P. Sidorenko, O. Cohen, I. P. Christov, M. M. Murnane, and H. C. Kapteyn. Phase matching of high harmonic generation in the soft and hard x-ray regions of the spectrum. *Proceedings of the National Academy of Sciences*, 106(26):10516–10521, 2009.

[90] H. R. Reiss. Effect of an intense electromagnetic field on a weakly bound system. *Phys. Rev. A*, 22:1786–1813, Nov 1980.

[91] P. Salières, A. L'Huillier, and M. Lewenstein. Coherence control of high-order harmonics. *Phys. Rev. Lett.*, 74:3776–3779, May 1995.

[92] K. J. Schafer, M. B. Gaarde, A. Heinrich, J. Biegert, and U. Keller. Strong field quantum path control using attosecond pulse trains. *Phys. Rev. Lett.*, 92:023003, Jan 2004.

[93] K. J. Schafer, B. Yang, L. F. DiMauro, and K. C. Kulander. Above threshold ionization beyond the high harmonic cutoff. *Phys. Rev. Lett.*, 70:1599–1602, Mar 1993.

[94] E. S. Shuman, R. R. Jones, and T. F. Gallagher. Multiphoton assisted recombination. *Phys. Rev. Lett.*, 101:263001, Dec 2008.

[95] N. I. Shvetsov-Shilovski, S. P. Goreslavski, S. V. Popruzhenko, and W. Becker. Ellipticity effects and the contributions of long orbits in nonsequential double ionization of atoms. *Phys. Rev. A*, 77:063405, Jun 2008.

[96] G. J. Smith. *Application of attosecond techniques to condensed matter systems.* PhD thesis, Ohio State University, 1224 Kinnear Road Columbus, OH 43212, 12 2020.

[97] S. L. Sorensen, T. Åberg, J. Tulkki, E. Rachlew-Källne, G. Sundström, and M. Kirm. Argon 3s autoionization resonances. *Phys. Rev. A*, 50:1218–1230, Aug 1994.

[98] Spectra-Physics. Maitai sp. Online, 4 2020. Date of Retrieval, See MaiTaiSP-Datasheet.pdf.

[99] Spectra-Physics. Spitfire ace pa. Online, 4 2020. Date of Retrieval, See SpitfireAcePADatasheet.pdf.

[100] M. Stecker, R. Nold, L.-M. Steinert, J. Grimmel, D. Petrosyan, J. Fortágh, and A. Günther. Controlling the dipole blockade and ionization rate of rydberg atoms in strong electric fields. *Phys. Rev. Lett.*, 125:103602, Aug 2020.

[101] D. Tew, W. Klopper, and T. Helgaker. Electron correlation: the many-body problem at the heart of chemistry. *J. Comput. Chem.*, 8:1307–1320, Jun 2007.

[102] C. E. Theodosiou. Lifetimes of singly excited states in he i. *Phys. Rev. A*, 30:2910–2921, Dec 1984.

[103] I. Vacuum. Ideal vacuum cube. Online, 3 2020. Date of Retrieval, See IdealVacCube-Brochure.pdf.

[104] H. van Linden van den Heuvell and H. Muller. In P. Knight and S. Smith, editors, *Multiphoton Processes.* Cambridge University Press, Cambridge, 1987.

[105] B. Walker, B. Sheehy, L. F. DiMauro, P. Agostini, K. J. Schafer, and K. C. Kulander. Precision measurement of strong field double ionization of helium. *Phys. Rev. Lett.*, 73:1227–1230, Aug 1994.

[106] H. Wang, M. Chini, S. Chen, C.-H. Zhang, F. He, Y. Cheng, Y. Wu, U. Thumm, and Z. Chang. Attosecond time-resolved autoionization of argon. *Phys. Rev. Lett.*, 105:143002, Oct 2010.

[107] Z. Wang. *Mid-infrared strong-field laser interactions with nanoclusters and semiconductors*. PhD thesis, Ohio State University, 1224 Kinnear Road Columbus, OH 43212, 12 2018.

[108] S. J. Weber, B. Manschwetus, M. Billon, M. Böttcher, M. Bougeard, P. Breger, M. Géléoc, V. Gruson, A. Huetz, N. Lin, Y. J. Picard, T. Ruchon, P. Salières, and B. Carré. Flexible attosecond beamline for high harmonic spectroscopy and xuv/near-ir pump probe experiments requiring long acquisition times. *Review of Scientific Instruments*, 86(3):033108, 2015.

[109] A. Zaïr, T. Siegel, S. Sukiasyan, F. Risoud, L. Brugnera, C. Hutchison, Z. Diveki, T. Auguste, J. W. Tisch, P. Salières, M. Y. Ivanov, and J. P. Marangos. Molecular internal dynamics studied by quantum path interferences in high order harmonic generation. *Chemical Physics*, 414:184–191, 2013. Attosecond spectroscopy.

[110] K. Zhang, Y. H. Lai, E. Diesen, B. E. Schmidt, C. I. Blaga, J. Xu, T. T. Gorman, F. m. c. Légaré, U. Saalmann, P. Agostini, J. M. Rost, and L. F. DiMauro. Universal pulse dependence of the low-energy structure in strong-field ionization. *Phys. Rev. A*, 93:021403, Feb 2016.